NATIONAL TECHNICAL UNIVERSITY OF ATHENS
SCHOOL OF MECHANICAL ENGINEERING
FLUIDS SECTION

BIOFLUID MECHANICS AND BIOMEDICAL ENGINEERING LABORATORY

"Ascending aortic aneurysm parametric modeling and computational study of the aortic wall stress state"

DIPLOMA THESIS

SEFERLIS KONSTANTINOS

Supervisor: Dr. Christos Manopoulos
Senior Researcher, N.T.U.A.

Athens, October 2020

ΕΘΝΙΚΟ ΜΕΤΣΟΒΙΟ ΠΟΛΥΤΕΧΝΕΙΟ
ΣΧΟΛΗ ΜΗΧΑΝΟΛΟΓΩΝ ΜΗΧΑΝΙΚΩΝ
ΤΟΜΕΑΣ ΡΕΥΣΤΩΝ

ΕΡΓΑΣΤΗΡΙΟ ΒΙΟΡΕΥΣΤΟΜΗΧΑΝΙΚΗΣ ΚΑΙ ΒΙΟΪΑΤΡΙΚΗΣ ΤΕΧΝΟΛΟΓΙΑΣ

« Παραμετρική μοντελοποίηση ανευρύσματος ανιούσης αορτής και υπολογιστική μελέτη της εντατικής κατάστασης του τοιχώματος »

ΔΙΠΛΩΜΑΤΙΚΗ ΕΡΓΑΣΙΑ

ΣΕΦΕΡΛΗΣ ΚΩΝΣΤΑΝΤΙΝΟΣ

Επίβλεψη : Χρήστος Μανόπουλος
Δρ., Ε.ΔΙ.Π., Ε.Μ.Π.

Αθήνα, Οκτώβριος 2020

Ευχαριστίες

Θα ήθελα να ευχαριστήσω θερμά τον επιβλέποντα κ. Χρήστο Μανόπουλο, Διδάκτορα Ε.ΔΙ.Π. του Εργαστηρίου Βιορευστομηχανικής & Βιοϊατρικής Τεχνολογίας Ε.Μ.Π., για την εμπιστοσύνη του στην ανάθεση της συγκεκριμένης διπλωματικής εργασίας, την καθοριστική συμβολή του και την συνεχή ενασχόληση για την επίτευξη του καλύτερου δυνατού αποτελέσματος. Επιπλέον, θερμές ευχαριστίες θα ήθελα να απευθύνω στον Μεταδιδάκτορα Αναστάσιο Ράπτη για την εκτεταμένη στήριξη του και τις πολύτιμες θεωρητικές και τεχνικές γνώσεις που μου παρείχε καθ' όλη τη διάρκεια εκπόνησης της διπλωματικής μου. Ιδιαίτερες ευχαριστίες οφείλω, επίσης, στον καρδιοχειρουργό, κ. Ηλία Κουερίνη, Επιμελητή Α' στο Καρδιοχειρουργικό Τμήμα του Γενικού Νοσοκομείου Αθηνών «Ιπποκράτειο», για τα δεδομένα αξονικών τομογραφιών που παρείχε, καθώς και την κριτική εξέταση των αποτελεσμάτων από ιατρική σκοπιά. Τέλος, θα ήθελα να ευχαριστήσω την οικογένειά μου και τους φίλους μου οι οποίοι με στήριξαν σε όλη τη διάρκεια των σπουδών μου αλλά και όλους εκείνους που βοήθησαν με τον τρόπο τους να πραγματοποιήσω τις σπουδές μου.

Acknowledgements

I would like to warmly thank my supervisor Dr. Christos Manopoulos, Senior Researcher in the Biofluid Mechanics and Biomedical Engineering Laboratory N.T.U.A., for trusting me with the assignment of this thesis, his significant contribution and his continuous commitment in order to achieve the best result possible. In addition, I would like to thank the Postdoctoral Fellow Anastasios Raptis for his extensive support and the valuable theoretical and technical knowledge he provided me throughout my diploma thesis. Special thanks, also, to the Attending Physician Dr. Elias Kouerinis, cardiac surgeon at the Cardiac Surgery Department of "Ippokrateio" General Hospital of Athens, for the CT scan data he provided, as well as the critical examination of the results from a medical point of view. Last but not least, I would like to thank my family and friends who supported me throughout my student course, as well as everyone that, in their way, helped me complete my studies.

Περίληψη

Η παρούσα εργασία έχει ως στόχο την μελέτη της φόρτισης του τοιχώματος ανευρύσματος ανιούσης αορτής σε φυσιολογική και υπερτασική εντατική κατάσταση κατά την καρδιακή συστολή.

Σε πρωταρχικό στάδιο έγινε συλλογή δεδομένων και γεωμετρικών χαρακτηριστικών από τη διεθνή βιβλιογραφία και έπειτα από επεξεργασία και προσαρμογή αυτών στις ανάγκες του εξεταζόμενου θέματος, προχωρήσαμε στο σχεδιασμό των αορτικών μοντέλων. Οι γεωμετρίες που σχεδιάστηκαν αποτελούν εξιδανικευμένα μοντέλα της ανθρώπινης αορτής.

Έπειτα από βιβλιογραφική διερεύνηση, βρέθηκε ότι το μέγεθος των αγγείων συνδέεται αναλογικά με τη σωματική διάπλαση του ανθρώπου, και πως είναι σύνηθες να ορίζεται το Εμβαδόν Επιφάνειας Σώματος (Body Surface Area) (m^2), ως δείκτης για την ποσοτικοποίηση του μεγέθους του ανθρώπινου σώματος. Για τον λόγο αυτό, επιλέχθηκαν τέσσερις χαρακτηριστικές τιμές εμβαδού επιφάνειας σώματος με τέτοιο τρόπο ώστε να καλύπτεται όλο το φάσμα των ανθρώπινων σωματικών διαπλάσεων και εν συνεχεία κατασκευάστηκαν τέσσερα μοντέλα φυσιολογικής αορτής, καθένα από τα οποία αντιστοιχούσε σε μια από αυτές τις τιμές.

Το επόμενο βήμα ήταν να σχεδιαστούν οι παθολογικές γεωμετρίες, δηλαδή τα ανευρυσματικά μοντέλα. Βασικό χαρακτηριστικό προσδιορισμού ενός ανευρύσματος είναι η μέγιστη διάμετρος του. Συμπερασματικά, σημαντική προϋπόθεση για την διεκπεραίωση μιας ολοκληρωμένης μελέτης είναι η σύγκριση ανευρυσμάτων διαφορετικού μεγέθους. Για αυτό τον λόγο, οι αρχικές, φυσιολογικές γεωμετρίες τροποποιήθηκαν και για καθεμία από αυτές σχεδιάστηκαν περίπου έξι διαφορετικά ανευρυσματικά μοντέλα. Τα παθολογικά, αορτικά μοντέλα, επομένως, παραμετροποιήθηκαν σύμφωνα με την διάμετρο ανευρύσματος.

Παράλληλα, αποκτήθηκαν δεδομένα αξονικών τομογραφιών από ασθενή που έπασχε από ανεύρυσμα ανιούσης αορτής. Η επεξεργασία και η σύνθεση των δεδομένων αυτών πραγματοποιήθηκε στο εμπορικό πακέτο MIMICS όπου επιτεύχθηκε ανακατασκευή του πραγματικού ανευρυσματικού αγγείου. Έτσι λοιπόν, έγινε δυνατή η μελέτη των εξιδανικευμένων μοντέλων σε σύγκριση με μια πραγματική παθολογική γεωμετρία. Η μελέτη αυτή έγινε μέσω της μεθόδου των πεπερασμένων στοιχείων με τη χρήση του δημοφιλούς λογισμικού ANSYS R19.0. Αρχικά, εισαγάγαμε τις γεωμετρίες στο πρόγραμμα και αφού θέσαμε τις απαραίτητες συνοριακές συνθήκες προχωρήσαμε στη φόρτιση του αορτικού αυλού με φυσιολογική (120mmHg) και υπερτασική (240 mmHg) συστολική πίεση. Η προσομοίωση για το μοντέλο ασθενούς έγινε στο πακέτο FEBio υπό τις ίδιες ακριβώς συνθήκες. Ομοίως, η επιλογή των ελαστικών ιδιοτήτων ήταν η ίδια και στις δύο περιπτώσεις θεωρώντας το υλικό ως ελαστικό και ισότροπο.

Με την ολοκλήρωση των προσομοιώσεων, εξήχθησαν αποτελέσματα τάσης *(σ)* – τροπής *(ε)* και η απεικόνιση τους έγινε μέσω στιγμιότυπων και διαγραμμάτων συναρτήσει της διαμέτρου του ανευρυσματικού ιστού. Αξίζει επίσης να σημειωθεί ότι στο Κεφάλαιο Results φαίνονται τα αποτελέσματα για ένα μόνο εξιδανικευμένο μοντέλο το οποίο προσεγγίζει καλύτερα την ανακατασκευασμένη γεωμετρία ενός ασθενούς, προκειμένου η σύγκριση μεταξύ τους να είναι ορθή και να μπορούμε να εξάγουμε ένα ασφαλές συμπέρασμα.

Εν τέλει, ως παράρτημα, παρατίθενται οι φωτογραφίες των αποτελεσμάτων όλων των μοντέλων καθώς και κάποια συμπληρωματικά διαγράμματα παραμόρφωσης και μέσης τάσης σε συνάρτηση με τη διάμετρο ανευρύσματος.

Abstract

The present thesis aims at studying the normal and hypertensive stress state of the ascending thoracic aortic aneurysm (aTAA) during cardiac systole.

Primarily, data and geometric features were collected from the international literature and after processing and adapting them to the needs of this thesis, we proceeded to design the aortic models. The designed geometries are idealized models of the human aorta.

After a literature study, it was found that the size of the vessels is proportionally related to the dimensions of the person, and that it is common to define Body Surface Area (m^2) (BSA) as an indicator for quantifying the size of the human body.

For this reason, four characteristic BSA values were selected in such a way as to cover the full range of human body sizes, and then four models of the physiological aorta were constructed, each corresponding to one of these values.

The next step was to design the pathological geometries, i.e. the aneurysmal models. A key feature in characterizing an aneurysm is its maximum diameter. Conclusively, an important condition for conducting a comprehensive study is the comparison of aneurysms of different sizes. For this reason, the original, physiological geometries were modified and for each of them, approximately six different aneurysmal (aTAA) models were designed. The pathological, aortic models, therefore, were parameterized according to the aneurysm diameter.

At the same time, computed tomography data were obtained from a patient suffering from an ascending aortic aneurysm. The processing and synthesis of this data was performed in the commercial package MIMICS where the reconstruction of the real aneurysmal vessel was achieved. Thus, it became possible to study the idealized models in comparison with a real pathological geometry.

This study was performed using the Finite Element Method (FEM) in ANSYS R19.0 software. Initially, we imported the geometries in the program and after setting the necessary boundary conditions we proceeded to load the aortic lumen with normal (120mmHg) and hypertensive (240 mmHg) systolic pressure. The simulation for the patient model was performed in the FEBio package under the exact same conditions. Similarly, the choice of elastic properties was the same in both, assuming an elastic and isotropic material.

Upon completion of the simulations, stress *(σ)* – strain *(ε)* results were extracted and visualized using snapshots and diagrams as a function of the diameter of the aneurysmal tissue. It is also worth noting that Results shows the results for a single idealized model that better approximates the reconstructed geometry, so that we are able to compare them and draw a safe conclusion.

Finally, photos of the results for all models are presented in the Appendix along with some additional diagrams of deformation and average stress with respect to aTAA diameter.

Index

Ευχαριστίες ***3***

Acknowledgements ***4***

Περίληψη ***5***

Abstract ***6***

Index ***7***

List of Figures ***9***

List of Tables ***12***

Nomenclature ***13***

Introduction ***15***

1. Theoretical Background ***16***

1.1 The Cardiovascular System **16**

1.2 Cardiovascular Diseases **17**

1.2.1 Aortic disease 17

1.2.2 Cerebrovascular disease 18

1.2.3 Coronary heart disease 18

1.2.4 Peripheral arterial disease 18

1.3 The normal aorta **18**

1.3.1 Function 18

1.3.2 Anatomical considerations 20

1.3.3 Aging of the aorta 22

1.4 Diseases of the aorta **22**

1.4.1 Aortic Aneurysms 22

1.4.2 Abdominal Aortic Aneurysms 23

1.4.3 Thoracic Aortic Aneurysms 24

1.4.4 Etiology and pathogenesis 26

1.4.5 Natural history 27

1.4.6 Surgical treatment 28

2. Defining the problem ***32***

2.1 Introduction **32**

2.2 Data collection and processing **35**

2.2.1 Age determination 35

2.2.2 Calculation of aortic diameter at diaphragm level 35

2.2.3 Calculation of total aortic length 39

2.2.4 Age transform coefficient 41

2.2.5 Cross section tapering 42

2.2.6 Thickness and tapering of the aortic wall 44

2.3 Design of the 3D models **46**
2.3.1 Idealized model 46
2.3.2 Patient-specific model 59
2.4 Materials and Methods **65**
2.4.1 Idealized geometry case preparation 65
2.4.2 Patient-specific case preparation 72
3. Results ***77***
3.1 Pathological cases **77**
3.2 Normal cases **82**
4. Conclusions and suggestions for future research ***92***
4.1 Conclusions **92**
4.2 Future research **92**
References ***93***
5. Appendix ***96***

List of Figures

Figure 1.1. The Circulatory system. [9] *16*
Figure 1.2. The structure of an artery wall. [11] *19*
Figure 1.3. Illustration of normal thoracic aortic anatomy. The brachiocephalic vessels arise from the transverse aortic arch and are used as anatomic landmarks to define the aortic regions. The ascending aorta is proximal to the innominate artery, whereas the descending aorta is distal to the left subclavian artery.[12] *21*
Figure 1.4. Diagram of the aorta and its named parts and branches.[13] *21*
Figure 1.5. A. Normal Aorta, B. Saccular aneurysm, C. Fusiform aneurysm. [14] *23*
Figure 1.6. Abdominal aneurysms.[15] *24*
Figure 1.7. Descending Aortic Aneurysm *25*
Figure 1.8. Thoracic Aortic Aneurysms.[16] *25*
Figure 1.9. Thoracoabdominal aneurysms (Crawford Classification).[17] *26*
Figure 1.10.Technique for the composite graft replacement of an aneurysm of the ascending aorta.[1] *29*
Figure 2.1. Ascending Thoracic Aortic Aneurysm (aTAA) *34*
Figure 2.2. Sagittal Image of the Aorta from the Aortic Root to the Level of the Bifurcation.[2] L1 through L5 indicate the level of cine phase contrast magnetic resonance imaging image acquisition, and R1 through R4 indicate the region of pulse wave velocity measurement. *36*
Figure 2.3. Association between Age and Systolic Diameter. *37*
Figure 2.4. Association between Age and Aortic Length.[2] *38*
Figure 2.5. Association of aorta length and body surface area (BSA). [25] *40*
Figure 2.6. Layout of electrical model of the human systemic arterial tree. (Rectangles with arrows represent regional peripheral resistances). *44*
Figure 2.7. Solidworks 2018 user interface. *47*
Figure 2.8. Inserting variables and dimensions into the program. *47*
Figure 2.9. (a). Centerline of the aortic model; brachiocephalic artery, left common carotid and left subclavian are not included in the design of the model. (b). Animation of thoracic aorta anatomy. PA : Pulmonary Artery [28] *48*
Figure 2.10. Planes positioned perpendicularly along the centerline. *49*
Figure 2.11. Sketched circles *49*
Figure 2.12. Close up view of the sketched circles and the applied dimensions. *50*
Figure 2.13. Creating the small (a) and large (b) solid by using the "Loft" command. *51*
Figure 2.14. (a); both solid bodies created from the "Loft" command are merged into each other (b); the smaller body had been subtracted from the larger one creating this way the wanted cavity. *52*
Figure 2.15. Section view of model; BSA=2.0 m^2, aneurysmal diameter= 77.5 mm, showing the 2D sketch of the spherical aneurysm. *53*
Figure 2.16. Preview of the revolution of the sketch. *54*
Figure 2.17. The created solid sphere as a result of the "Revolve" command. *54*
Figure 2.18. Section view of the model that shows the spherical solid intersecting with the normal geometry. *55*
Figure 2.19. Scatterplot of wall thickness (μm) against aortic diameter (mm) [29] *56*
Figure 2.20. (a) The intersecting parts of the hollow sphere with the normal aortic model. (b) Preview of the "Intersect" command; after selecting the intersecting sections (highlighted areas), the command enables the removal of those parts and the merge of the remaining ones into one solid body. *57*
Figure 2.21. Creating fillets on sharp edges in order to achieve a more realistic result; the primary stage (before fillet) is depicted on the left set of pictures. The pictures in the bottom show a section view of the pictures in the top of the figure. *58*
Figure 2.22. Final form of the idealized pathological aortic model. *58*
Figure 2.23.Toshiba's Activion 16 Multislice CT system. *59*
Figure 2.24. 3D view of the CT scan *60*
Figure 2.25. Mimics user interface. *61*

Figure 2.26. The aTAA model in different views after isolating the aortic lumen. *62*
Figure 2.27. 3D aTAA model before (a) and after (b) smoothing. *63*
Figure 2.28. (a) Superposition of the aTAA and left ventricle surfaces and (b) resulting aTAA model after intersection featuring the aortic valve opening. *63*
Figure 2.29. Final result of the meshed aneurysmatic aortic model. *64*
Figure 2.30. ANSYS Workbench R19.0 User Interface. *65*
Figure 2.31. (a) and (b) represent a Poisson coefficient of v=0.45 while (c) and (d) were computed for v=0.49. The models on the left are loaded with 120 mmHg and the ones on the right with 240 mmHg. All models refer to a BSA of 2.0 m^2 and an aneurysmal diameter equal to 65 mm. *66*
Figure 2.32. Relationship between E_{inc} and aortic diameter in ascending aortic aneurysms.[40] *67*
Figure 2.33. Principles of calculating the physiologic range, hypertensive range, and Maximum Elastic Modulus (MEM).[41] *67*
Figure 2.34. Relationship between the diameter of the ascending thoracic aortic aneurysm ATAA D (cm) and the elastic modulus E (MPa) for the pressures of 120 mmHg (red curve) and 240 mmHg (black curve) *68*
Figure 2.35. Setting a uniform and normal to the internal surface pressure. (120 mmHg = 15999 Pa) *68*
Figure 2.36. Inserting boundary conditions in ANSYS. *69*
Figure 2.37. The window that appears during the solution process in ANSYS and shows the convergence progress by presenting graphically the calculated value of the selected result (here: maximum stress) for every solution. The table below the chart presents the error (change (%)) as well as the density of the mesh in every iteration. It is clear that the criterion of 0.5% has been fulfilled in this simulation. *71*
Figure 2.38. FEBio Studio user interface. *72*
Figure 2.39. Mesh of the model. *73*
Figure 2.40. Selection of the internal surface in order to apply a uniform pressure. *73*
Figure 2.41. Fixing both ends of the aorta model. *74*
Figure 2.42. CT slice showing the maximal diameter of the aneurysm extending up to 7 cm. *75*
Figure 2.43. Flowchart illustrating the consecutive stages of the analysis. *76*
Figure 3.1. BSA=2.0 m^2 aneurysmal diameter D=55mm (α). Equivalent Elastic Strain at 120 mmHg (b). Von-Mises Stress at 120 mmHg (c). Equivalent Elastic Strain at 240 mmHg (d). Von-Mises Stress at 240 mmHg *77*
Figure 3.2. BSA=2.0 m^2 aneurysmal diameter D=77.5mm (α). Equivalent Elastic Strain at 120 mmHg (b). Von-Mises Stress at 120 mmHg (c). Equivalent Elastic Strain at 240 mmHg (d). Von-Mises Stress at 240 mmHg *78*
Figure 3.3. Patient case (α). Equivalent Elastic Strain at 120 mmHg (b). Von-Mises Stress at 120 mmHg (c). Equivalent Elastic Strain at 240 mmHg (d). Von-Mises Stress at 240 mmHg *79*
Figure 3.4. BSA=1.65 m^2; (a) Maximum Equivalent Elastic Strain (m/m) – Aneurysmal Diameter (mm). (b) Maximum Stress (MPa) – Aneurysmal diameter (mm). *80*
Figure 3.5. BSA=1.85 m^2; (a) Maximum Equivalent Elastic Strain (m/m) – Aneurysmal Diameter (mm). (b) Maximum Stress (MPa) – Aneurysmal diameter (mm). *80*
Figure 3.6. BSA=2.00 m^2; (a) Maximum Equivalent Elastic Strain (m/m) – Aneurysmal Diameter (mm). (b) Maximum Stress (MPa) – Aneurysmal diameter (mm). *80*
Figure 3.7. BSA=2.20 m^2; (a) Maximum Equivalent Elastic Strain (m/m) – Aneurysmal Diameter (mm). (b) Maximum Stress (MPa) – Aneurysmal diameter (mm). *81*
Figure 3.8. BSA=1.65 m^2, 120 mmHg; (a) Equivalent Elastic Strain (m/m) with a section view in (c). (b) Equivalent Stress with a section view in (d). *82*
Figure 3.9. BSA=1.65 m^2, 240 mmHg; (a) Equivalent Elastic Strain (m/m) with a section view in (c). (b) Equivalent Stress with a section view in (d). *83*
Figure 3.10. BSA=1.85 m^2, 120 mmHg; (a) Equivalent Elastic Strain (m/m) with a section view in (c). (b) Equivalent Stress with a section view in (d). *84*
Figure 3.11. BSA=1.85 m^2, 240 mmHg; (a) Equivalent Elastic Strain (m/m) with a section view in (c). (b) Equivalent Stress with a section view in (d). *85*

Figure 3.12. BSA=2.0 m^2, 120 mmHg; (a) Equivalent Elastic Strain (m/m) with a section view in (c). (b) Equivalent Stress with a section view in (d). *86*
Figure 3.13. BSA=2.0 m^2, 240 mmHg; (a) Equivalent Elastic Strain (m/m) with a section view in (c). (b) Equivalent Stress with a section view in (d). *87*
Figure 3.14. BSA=2.2 m^2, 120 mmHg; (a) Equivalent Elastic Strain (m/m) with a section view in (c). (b) Equivalent Stress with a section view in (d). *88*
Figure 3.15. BSA=2.2 m^2, 240 mmHg; (a) Equivalent Elastic Strain (m/m) with a section view in (c). (b) Equivalent Stress with a section view in (d). *89*
Figure 3.16. (a) Maximum Equivalent Elastic Strain (m/m) – BSA (m^2). (b) Maximum Stress (MPa) – BSA (m^2). *89*
Figure 3.17. (a) Maximum Total Deformation (mm) – BSA (m^2). (b) Average Stress (MPa) – BSA (m^2). *90*
Figure 3.18. (a) BSA (m^2)-aneurysmal diameter (mm)-maximum strain (m/m); 120 mmHg. (b) BSA (m^2)-aneurysmal diameter (mm)-maximum stress (MPa); 120 mmHg. (c) BSA (m^2)-aneurysmal diameter (mm)-maximum strain (m/m); 240 mmHg. (d) BSA (m^2)-aneurysmal diameter (mm)-maximum stress (MPa); 240 mmHg. *91*
Figure 5.1. BSA=1.65 m^2, aneurysmal diameter = 52.5 mm *96*
Figure 5.2. BSA=1.65 m^2, aneurysmal diameter=55 mm *97*
Figure 5.3. BSA=1.65 m^2, aneurysmal diameter=60 mm *97*
Figure 5.4. BSA=1.65 m^2, aneurysmal diameter=65 mm *98*
Figure 5.5. BSA=1.65 m^2, aneurysmal diameter=67.5 mm *98*
Figure 5.6. BSA=1.65 m^2, aneurysmal diameter=70 mm *99*
Figure 5.7. BSA=1.85 m^2, aneurysmal diameter=52.5 mm *99*
Figure 5.8. BSA=1.85 m^2, aneurysmal diameter=55 mm *100*
Figure 5.9. BSA=1.85 m^2, aneurysmal diameter=60 mm *100*
Figure 5.10. BSA=1.85 m^2, aneurysmal diameter=65 mm *101*
Figure 5.11. BSA=1.85 m^2, aneurysmal diameter=70 mm *101*
Figure 5.12. BSA=1.85 m^2, aneurysmal diameter=75 mm *102*
Figure 5.13. BSA=2.0 m^2, aneurysmal diameter=55 mm *102*
Figure 5.14. BSA=2.0 m^2, aneurysmal diameter=60 mm *103*
Figure 5.15. BSA=2.0 m^2, aneurysmal diameter=65 mm *103*
Figure 5.16. BSA=2.0 m^2, aneurysmal diameter=70 mm *104*
Figure 5.17. BSA=2.0 m^2, aneurysmal diameter=75 mm *104*
Figure 5.18. BSA=2.0 m^2, aneurysmal diameter=77.5 mm *105*
Figure 5.19. BSA=2.2 m^2, aneurysmal diameter=55 mm *105*
Figure 5.20. BSA=2.2 m^2, aneurysmal diameter=60 mm *106*
Figure 5.21. BSA=2.2 m^2, aneurysmal diameter=65 mm *106*
Figure 5.22. BSA=2.2 m^2, aneurysmal diameter=70 mm *107*
Figure 5.23. BSA=2.2 m^2, aneurysmal diameter=75 mm *107*
Figure 5.24. BSA=2.2 m^2, aneurysmal diameter=77.5 mm *108*
Figure 5.25. BSA=2.2 m^2, aneurysmal diameter=80 mm *108*
Figure 5.26. BSA = 1.65 m^2; (a) Average Stress (MPa) – Aneurysmal diameter (mm). (b) Maximum Total Deformation (mm) – Aneurysmal diameter (mm). *109*
Figure 5.27. BSA = 1.85 m^2; (a) Average Stress (MPa) – Aneurysmal diameter (mm). (b) Maximum Total Deformation (mm) – Aneurysmal diameter (mm). *109*
Figure 5.28. BSA = 2.00 m^2; (a) Average Stress (MPa) – Aneurysmal diameter (mm). (b) Maximum Total Deformation (mm) – Aneurysmal diameter (mm). *110*
Figure 5.29. BSA = 2.20 m^2; (a) Average Stress (MPa) – Aneurysmal diameter (mm). (b) Maximum Total Deformation (mm) – Aneurysmal diameter (mm). *110*

List of Tables

Table 2.1. Risk of Complications by Aortic Diameter and Body Surface Area with Aortic Size Index Given Within Chart. [8] *33*
Table 2.2. Subject Characteristics (BMI = body mass index; BP = blood pressure; HDL = high-density lipoprotein; HR = heart rate; LDL = low-density protein; MAP = mean arterial pressure.) *39*
Table 2.3. Clinical characteristics of the examined sample in Sorimachi's study. [25] *41*
Table 2.4. Numerical data on segments of Figure 2.6. ..... *45*

Nomenclature

Symbol	***Description***	***Unit***
A	*Aortic lumen cross section*	*[m^2]*
A_0	*Aortic lumen cross section at the upstream site*	*[m^2]*
ASI	*Aortic Size Index*	*[cm/m^2]*
B	*Taper factor*	-
BMI	*Body Mass Index*	*[kg/m^2]*
BSA	*Body Surface Area*	*[m^2]*
D_d	*Aortic lumen diameter at diaphragm level*	*[mm]*
D_{PA}	*Aortic lumen diameter at pulmonary artery bifurcation level*	*[mm]*
E	*Elastic Modulus*	*[MPa]*
E_{inc}	*Incremental Elastic Modulus*	*[MPa]*
h	*Aortic wall thickness*	*[mm]*
h_0	*Aortic wall thickness at the upstream site*	*[mm]*
hgt	*Height*	*[cm]*
L_{tot}	*Length of the aorta from valve to aortic bifurcation*	*[mm]*
MEM	*Maximum Elastic Modulus*	*[MPa]*
R	*Aortic lumen radius*	*[mm]*
R_0	*Aortic lumen radius at the upstream site*	*[mm]*
R_d	*Aortic lumen radius at diaphragm level*	*[mm]*
R_{PA}	*Aortic lumen radius at pulmonary artery bifurcation level*	*[mm]*
U	*Total Deformation*	*[mm]*
U_x	*Deformation in x direction*	*[mm]*
U_y	*Deformation in y direction*	*[mm]*
U_z	*Deformation in z direction*	*[mm]*
wgt	*Weight*	*[kg]*
x_d	*Length of the aorta from valve to diaphragm level*	*[mm]*
x_{PA}	*Length of the aorta from valve to pulmonary artery bifurcation level*	*[mm]*

Abbreviation

AAA	*Abdominal Aortic Aneurysm*
aPWV	*Aortic Pulse Wave Velocity*
aTAA	*Ascending Thoracic Aortic Aneurysm*
CAD	*Coronary Artery Disease*
CHD	*Coronary Heart Disease*
CT	*Computed Tomography*
CVA	*Cerebrovascular Aneurysm*
CVD	*Cardiovascular Disease*
DICOM	*Digital Imaging and Communication in Medicine*
FEM	*Finite Element Method*
IHD	*Ischemic Heart Disease*
MRI	*Magnetic Resonance Imaging*
PAD	*Peripheral Arterial Disease*
STL	*Stereolithography*
TIA	*Transient Ischemic Attack*

Greek Symbols

$\varepsilon/\varepsilon_e$	*Equivalent strain*	*[m/m]*
v	*Poisson's Ratio*	-
σ	*Stress*	*[MPa]*

Subscript

d	*Diaphragm*
e	*Equivalent*
inc	*Incremental*
PA	*Pulmonary Artery*
tot	*Total*

Introduction

The aorta is the main artery which transports blood from the heart to the rest of the body through a complex network of arteries and capillaries. It consists of the ascending aorta, the aortic arch, the descending aorta and the abdominal aorta. One of the most common diseases of the human aorta is the aneurysm which is a local dilatation of the vessel, due to weakening of the aortic wall [3, 4]. If the stress applied on the dilated tissue reaches a certain threshold value then this can lead to aneurysm rupture, which is a medical emergency that can prove to be fatal [5]. Surgical intervention to repair an aneurysm before rupture always undertakes risk, therefore accurate prediction of aneurysm rupture is of paramount significance. Clinically, the most widely used criterion for the decision of preemptive surgery is the maximum diameter of an aneurysm [4]. It is reported that hinge points for natural complications of aortic aneurysm were found at 6.0 cm for the ascending and 7.0 to 7.2 cm for the descending aorta [6, 7].

Aneurysmal diameter becomes even more accurate as an indicator for aortic rupture when it is correlated with the BSA of the patient. Davies R.R. and colleagues, in 2006, introduced the term of Aortic Size Index (ASI) as a ratio of the aortic diameter and BSA, and confirmed in their study that relative aortic size is more important than absolute aortic size in predicting complications [8].

One of the primary purposes of this thesis is the verification of the findings that Davies describes in his publication. As a result, we performed a stress analysis with finite element (FE) simulations on idealized geometric models of the human aorta with aTAA (Ascending Thoracic Aortic Aneurysm), as well as a on a three-dimensional (3D) FE model that was built from computed tomography (CT) scan data. The stress and the strain distributions in the aneurysmal wall were observed after imposing boundary conditions and loading the vessel with physiological and hypertensive values of blood pressure.

1. Theoretical Background

1.1 The Cardiovascular System

The cardiovascular system is made up by the heart and circulatory system. The heart works as a pump that pushes blood to the organs, tissues, and cells of the body through a complex network of arteries, arterioles, and capillaries. This way, blood delivers oxygen and other essential nutrients to every cell and removes carbon dioxide and waste products made by those cells. It, then, returns through the veins and venules in the lungs where it is enriched with oxygen. At that point, this oxygenated blood, flows to the heart from where, once again circulates through the whole body. The main function of the cardiovascular system is, therefore, to maintain blood flow to all parts of the body, to allow it to survive (Figure 1.1 shows the female and male circulatory system).

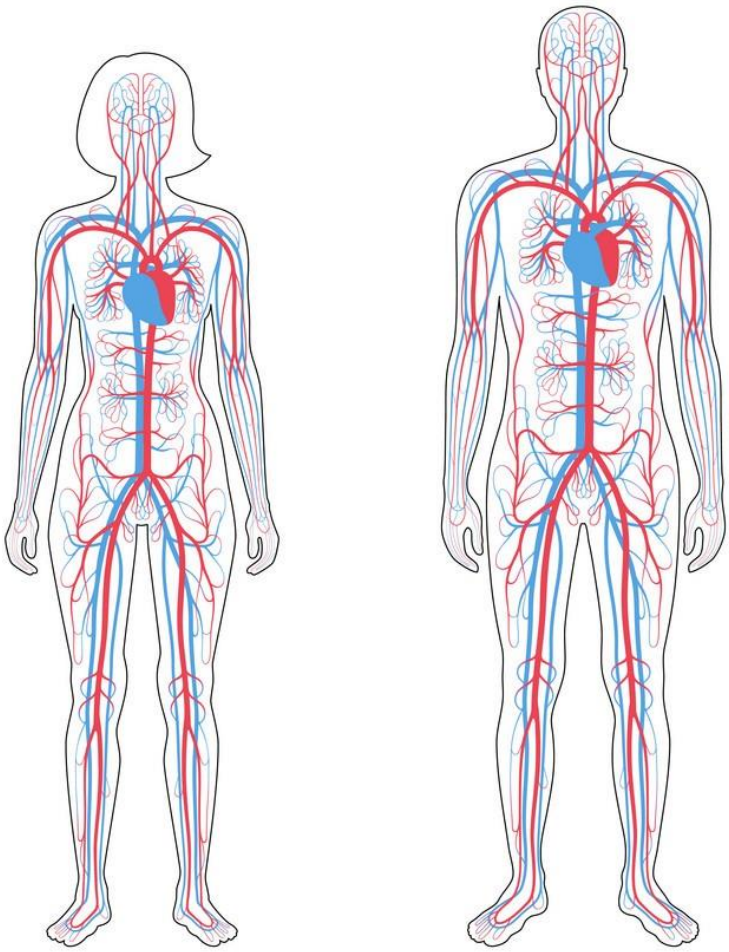

Figure 1.1. The Circulatory system. [9]

1.2 Cardiovascular Diseases

Cardiovascular disease (CVD) is a general term for conditions affecting the heart or blood vessels. It's usually associated with a build-up of fatty deposits inside the arteries (atherosclerosis) and an increased risk of blood clots. It can also be associated with damage to arteries in organs such as the brain, heart, kidneys and eyes. CVD is one of the main causes of death and disability in the world, but it can often largely be prevented by leading a healthy lifestyle.

There are many different types of CVD. Four of the main types are described below.

1.2.1 Aortic disease

Aortic disease is a term that refers to a group of diseases affecting the aorta or the body's main artery. This major blood vessel runs from the heart's left ventricle and extends to the abdominal area, splitting into two branches known as the common iliac arteries. The proper function and good condition of the aorta are highly important as it is responsible for transporting and distributing oxygenated blood to and from the heart and the rest of the body.

Aortic diseases often lead to the dysfunction of aorta and disruption in blood circulation, which can be life-threatening. Described below are the different types of aortic diseases.

Aortic valve regurgitation. This condition is characterized by the inability of the aortic valve to close properly, leading to the blood flowing backward into the heart's left ventricle instead of flowing into the different parts of the body. The regurgitation of the blood prevents the heart from functioning efficiently, leading to a number of symptoms such as fatigue and breathing difficulties. This condition typically develops over time, and in many cases, it takes years before the patient notices any signs or symptoms.

Aortic stenosis. This condition involves the narrowing of the aorta, which prevents the aortic valve from fully opening. It prevents the blood from flowing efficiently from the heart to the aorta, leading to inefficient blood oxygenation and circulation to the rest of the body. In such event, the heart will be forced to work harder to compensate for the condition. Over time, the overworked heart muscles can weaken and pose a serious threat to the life of the patient.

Aortic dissection. A dissection is a tear in the walls of the aorta, causing the blood to leak in the layers of the artery, where fluid is not supposed to be. This condition leads to the lack of proper amount of oxygen and other nutrients in the blood, which can result in serious risks and complications to various organs of the body.

Aortic aneurysm. An aortic aneurysm is the excessive enlargement of an artery, often leading to the weakening of its walls. The enlargement over stretches the tissues of the aortic walls; and when the aortic walls become too weak, they burst and cause excessive bleeding that can be fatal for the patient. These aneurysms can form in different parts of the aorta but are especially common in the abdominal region of the aorta. This disease is further investigated in the next chapters as it is the main concern of focus in this thesis.

Aortic diseases should be caught and treated early. It is best for individuals to undergo screening for such diseases every year, especially if they are at high risk of developing any of the diseases described above.

Chest MRI, ultrasound, arteriogram, and CT scans are just some of the available diagnostic imaging procedures that they can undergo.

1.2.2 Cerebrovascular disease

Cerebrovascular diseases are brain malfunctions related to the blood vessels supplying the brain. Like the heart, the brain does not anastomose or find alternative arterial routes to blocked vessels. Blockage of a cerebrovascular vessel can cause stroke, transient ischemic attack (TIA) or CVA (cerebrovascular aneurysm). Hypertension is a common cause of cerebrovascular disease. It damages the blood vessel lining. Sustained hypertension permanently changes the architecture of the blood vessels making them narrow, stiff, deformed, and more vulnerable to fluctuations in blood pressure. A fall in blood pressure during sleep can lead to a marked reduction in blood flow causing ischemic stroke or CVA. A sudden rise in blood pressure due to excitation can cause tearing of the blood vessels. Cerebrovascular disease affects people who are elderly, have a history of diabetes, smoking, or ischemic heart disease (IHD).

1.2.3 Coronary heart disease

Coronary heart disease (CHD) also known as coronary artery disease (CAD) or ischemic heart disease (IHD), involves the reduction of blood flow to the heart muscle, most commonly due to obstruction of the coronary arteries by atheromatous plaque. Coronary arteries form the network of blood vessels on the surface of the heart that feed it oxygen. If these arteries narrow, the heart may not receive enough oxygen rich blood, especially during physical activity and in severe cases can lead to heart attack. Factors that predispose to this condition (atherosclerosis) include hyperlipidemia, smoking, hypertension, diabetes and physical inactivity.

1.2.4 Peripheral arterial disease

Peripheral arterial disease (PAD) is a disorder of the peripheral arteries, defined as all the arteries of the body except coronary vessels. However, it is the circulation of the lower limb that is most frequently involved. Atherosclerosis is the major cause of chronic PAD. General interest in the management of patients with PAD has increased in recent years, and there has been a shift from vascular surgical domination to comprehensive vascular centers integrating surgical, endovascular and medical services. Patients afflicted with PAD are recognized as cardiovascular high-risk population and therefore primary and secondary prevention endovascular treatment options and novel gene therapeutic approaches in addition to classical vascular surgery, may hold potential for the future. [10]

During this study, aortic aneurysms and specifically those of the ascending aorta, are examined extensively. However, before we look into that we must firstly define the normal aorta and its role.

1.3 The normal aorta

1.3.1 Function

Appropriately called “the greatest artery” by the ancients, the aorta is admirably suited for its task. In an average lifetime, this thin but large and remarkably tough vessel must absorb the impact of 2.3 to 3 billion heartbeats while carrying roughly 200 million liters of blood through the body. Arteries can be categorized as either *conductance* or *resistance* vessels. Conductance vessels are the conduits for blood and the aorta is the ultimate conductance vessel.

The aorta is composed of three layers: the thin inner layer, or *intima;* a thick middle layer, or *media*; and a rather thin outer layer, the *adventitia* (Figure 1.2). The strength of the aorta lies in the media, which is composed of laminated but intertwining sheets of elastic tissue arranged in a spiral manner that affords maximum tensile strength. Indeed, as thin as it is, the aortic wall can withstand the experimental pressure of thousands of millimeters of mercury without bursting. In contrast to the peripheral arteries, the aortic media contains relatively little smooth muscle and collagen between the elastic layers. It is this tremendous accretion of elastic tissue that gives the aorta not only tensile strength but also distensibility and elasticity, which serve a vital circulatory role. The aortic intima is a thin and delicate layer that is lined by endothelium and easily traumatized. The adventitia contains mainly collagen and carries the important vasa vasorum, which nourish the outer half of the aortic wall, including much of the media.

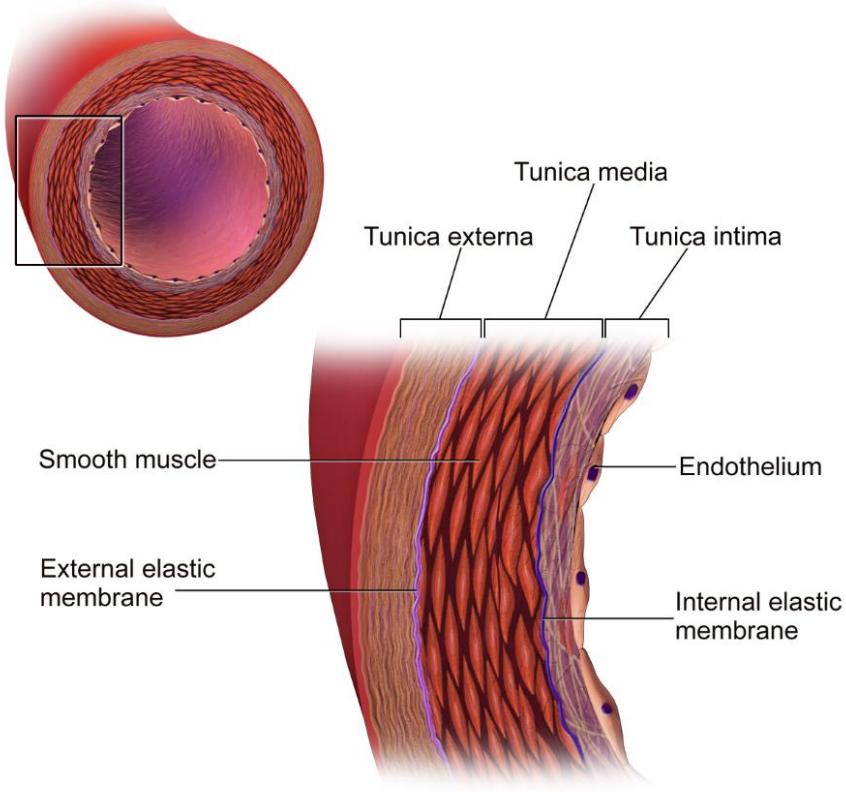

Figure 1.2. The structure of an artery wall. [11]

During ventricular systole, the aorta is distended by the force of the blood elected into it by the left ventricle, and in this manner part of the kinetic energy generated by the contracting left ventricle is converted into potential energy stored in the aortic wall. Then, during diastole, this potential energy is transformed back into kinetic energy as the aortic walls recoil, propelling the blood in the aortic lumen distally into the arterial bed. Thus, the aorta plays an essential role in maintaining forward circulation of the blood in diastole after it is delivered into the aorta by the left ventricle during systole. The pulse wave itself, with its milking effect, is transmitted along the aorta to the periphery at a speed of about 5 m/sec. This is much faster than the velocity of the intraluminal blood itself, which travels at only 40 to 50 cm/sec. The systolic pressure developing within the aorta is a function of the volume of blood ejected into the

aorta, the compliance or distensibility of the aorta and the resistance to blood flow. This resistance is determined primarily by the tone of the peripheral muscular arteries and arterioles and to a slight extent by the inertia of the column of blood in the aorta when systole commences. In addition to its conductance and pumping functions, the aorta also plays a role in indirectly controlling systemic vascular resistance and heart rate. Pressure-responsive receptors, analogous to those in the carotid sinus, lie in the ascending aorta and aortic arch and send afferent signals to the vasomotor center in the brain stem by way of the vagus nerves. Raising the intra-aortic pressure causes reflex bradycardia and reduction of systemic vascular resistance, whereas lowering the pressure increases the heart rate and vascular resistance.

1.3.2 Anatomical considerations

The aorta is divided anatomically into its thoracic and abdominal components. The thoracic aorta is further divided into the ascending, arch and descending segments (Figure 1.4), while the abdominal aorta consists of *suprarenal* and *infrarenal* segments.

The ascending aorta is about 5 cm long and has two distinct segments. The lower segment is the *aortic root*, beginning at the level of the aortic valve and extending to the sinotubular junction. This is the widest portion of the ascending aorta, measuring about 3.3 cm in width. The bases of the aortic leaflets are supported by the aortic root from which the three sinuses of Valsalva bulge outward to allow for the full excursion of aortic valve leaflets during systole. In addition, the two coronary arteries arise from these sinuses of Valsalva. The upper tubular segment of the ascending aorta rises to join the aortic arch. Normally the ascending aorta sits just to the right of midline, with its proximal portion lying within the pericardial cavity. Nearby structures include the pulmonary artery anteriorly and leftward the left atrium, right pulmonary artery, and right mainstem bronchus posteriorly, and the right atrium and superior vena cava to the right.

The *arch of the aorta* gives rise to all of the brachiocephalic arteries. From the ascending aorta it courses slightly leftward in front of the trachea and then proceeds posteriorly to the left of the trachea and esophagus. The pulmonary artery bifurcation and right pulmonary artery lie inferior to the arch, as does the left lung. The recurrent laryngeal nerve loops underneath the arch distally, and the phrenic and vagus nerves lie to the left.

The *descending thoracic aorta* begins in the posterior mediastinum to the left of the vertebral column and gradually courses in front of the vertebral column as it descends, occupying a position immediately behind the esophagus. Distally it passes through the diaphragm, usually at the level of the twelfth thoracic vertebra.

The point at which the aortic arch joins the descending aorta is called the *aortic isthmus*. The aorta is especially vulnerable to trauma at this site because it is here that the relatively mobile portion of the aorta - the ascending aorta and arch - becomes relatively fixed to the thoracic cage by the pleural reflections, the paired intercostal arteries, and the left subclavian artery. This is also where coarctations of the aorta are located. The abdominal aorta continues from the thoracic aorta, giving off the important splanchnic arteries and ending at its bifurcation at the level of the fourth lumbar vertebra.

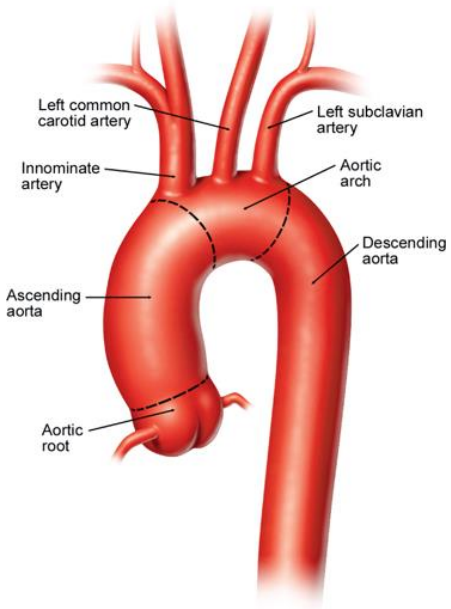

Figure 1.3. Illustration of normal thoracic aortic anatomy. The brachiocephalic vessels arise from the transverse aortic arch and are used as anatomic landmarks to define the aortic regions. The ascending aorta is proximal to the innominate artery, whereas the descending aorta is distal to the left subclavian artery.[12]

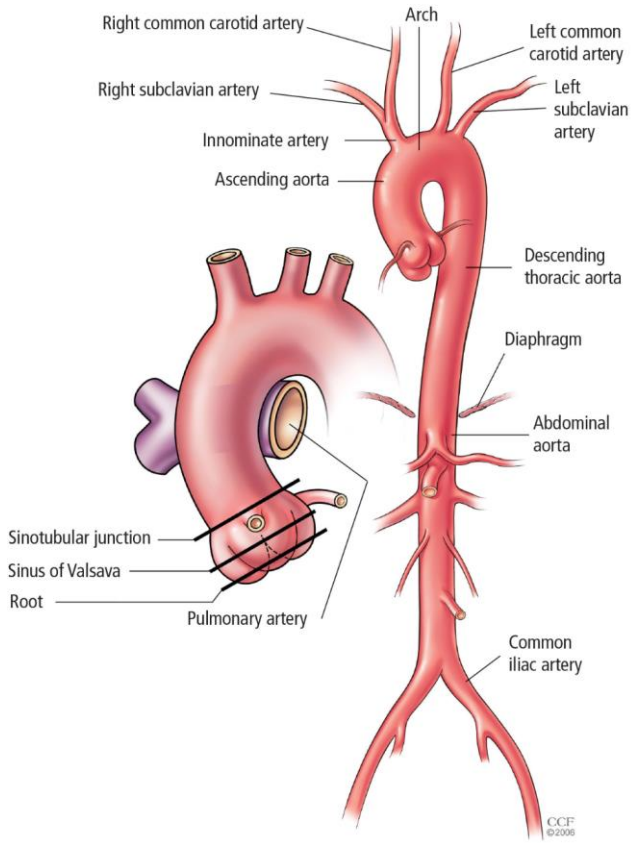

Figure 1.4. Diagram of the aorta and its named parts and branches.[13]

1.3.3 Aging of the aorta

As discussed above, the elastic properties of the aorta are crucial to its normal function. However, it has been well demonstrated that the elasticity and distensibility of the aorta decline with age. Such changes are seen even in normal healthy adults, and for unknown reasons these changes occur earlier and are more progressive among men than women. The loss of elasticity and aortic compliance likely accounts for the increase in pulse pressure commonly seen in the elderly. This progressive loss of aortic elasticity with aging is accelerated among those with hypertension compared with age-matched normotensive controls. Similarly, those with hypercholesterolemia or coronary artery disease show a greater loss of elasticity than do controls. Conversely, among healthy athletes, elasticity is higher than among their age-matched controls.

Histologically, the aging aortic wall exhibits fragmentation of elastin with a concomitant increase in collagen, resulting in an increased collagen-to-elastin ratio that contributes to the loss of aortic distensibility observed physiologically. Recent experimental animal data suggest that impairment of vasa vasorum flow to the aortic wall results in stiffening of the aorta with similar histological changes and may therefore be one cause of the degenerative changes seen with age.

In animal models it has been demonstrated that a loss of aortic distensibility directly affects the mechanical performance of the left ventricle, producing increases in left ventricular systolic pressure and wall tension and in end-diastolic pressure and volume. Furthermore, reduced aortic compliance causes a 20 to 40 per cent increase in myocardial oxygen consumption in order to maintain a given stroke volume. It is therefore likely that, over time, the changes in aortic compliance seen with age may cause clinically important alterations in cardiac function.

1.4 Diseases of the aorta

1.4.1 Aortic Aneurysms

The term *aortic aneurysm* refers to a pathological dilatation of the normal aortic lumen involving one or several segments. Although there is perhaps no universally accepted definition, an aortic aneurysm is best described as a permanent localized dilatation of the aorta having a diameter at least 1.5 times that of the expected normal diameter of that given aortic segment. Aneurysms are usually described in terms of their location, size, morphology, and etiology. The morphology of an aortic aneurysm is typically either *fusiform*, which is the more common shape, or *saccular*. A fusiform aneurysm is fairly uniform in shape, with symmetrical dilatation that involves the full circumference of the aortic wall. The dilatation seen in saccular aneurysms, on the other hand, is more localized, appearing as an outpouching of only a portion of the aortic wall. In addition, there may be a pseudoaneurysm or false aneurysm of the aorta, which is not actually an aneurysm at all but rather a well-defined collection of blood and connective tissue outside the vessel wall. This may be a consequence of a contained rupture of the aortic wall.

The presence of an aortic aneurysm may be a marker of more diffuse aortic disease. Overall, up to 13 per cent of all patients diagnosed with an aortic aneurysm are found to have multiple aneurysms, with up to 25 to 28 per cent of those with thoracic aortic aneurysms having concomitant abdominal aortic aneurysms.

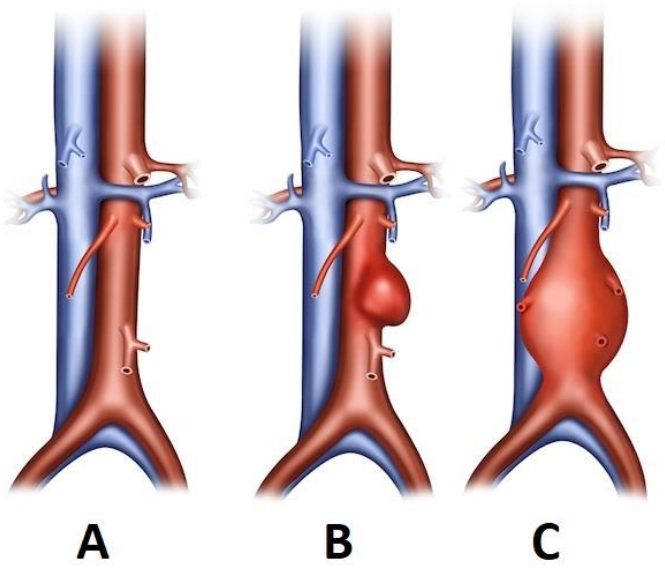

Figure 1.5. A. Normal Aorta, B. Saccular aneurysm, C. Fusiform aneurysm. [14]

1.4.2 Abdominal Aortic Aneurysms

Abdominal aortic aneurysms are much more common than are thoracic aortic aneurysms. Age is an important risk factor, as the incidence rises rapidly after 55 years of age in men and 70 years of age in women, and abdominal aortic aneurysms occur four to five times more frequently in men than in women. The incidence of abdominal aneurysms has increased threefold in recent decades from 8.7 per 100.000 person-years in 1951 to 1960 to 36.5 per 100.000 person-years in 1971 to 1980. Because the incidence of abdominal aneurysms of all sizes has increased, it is believed that these data at least in part reflect a true increase in the disease incidence. Other factors that may have contributed to the marked rise in the incidence of such aneurysms include the increasing mean age of the population, a greater awareness of the association of aneurysmal disease with other prevalent cardiovascular conditions and improvements in diagnostic evaluation. The prevalence of abdominal aortic aneurysms in the population 50 years of age and older is at least 3 per cent.

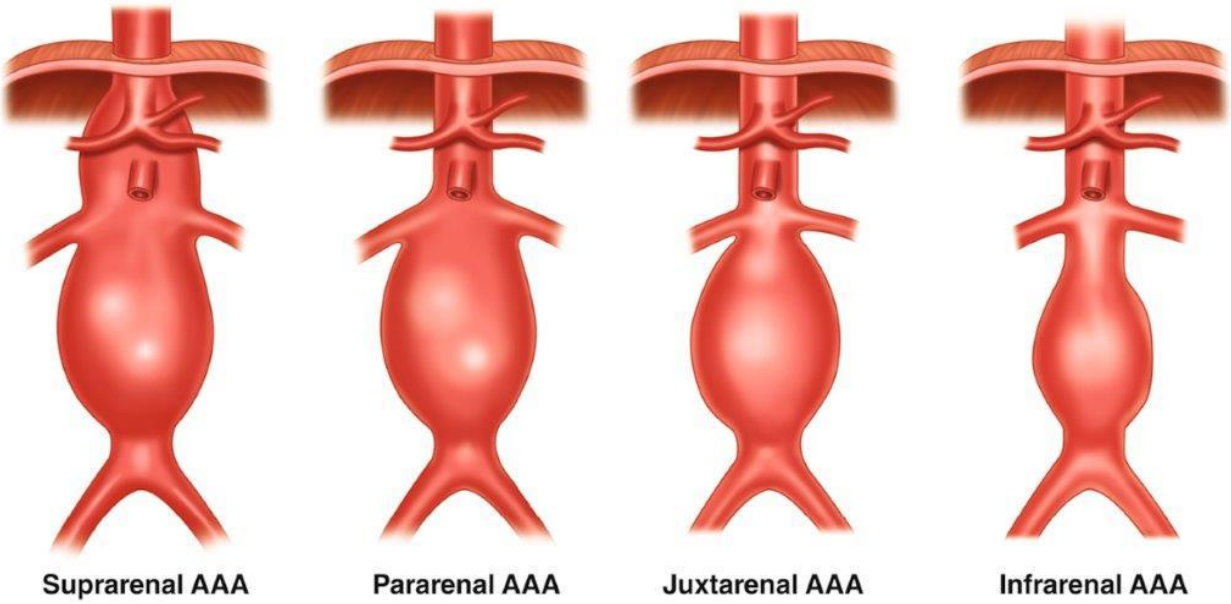

Figure 1.6. Abdominal aneurysms.[15]

1.4.3 Thoracic Aortic Aneurysms

Thoracic aortic aneurysms are much less common than are aneurysms of the abdominal aorta, and their incidence did not increase over the same 30-year period that saw marked increase in the incidence of abdominal aortic aneurysms (as noted above). Thoracic aneurysms are classified by the portion of aorta involved, i.e., the ascending, arch or descending thoracic aorta. This anatomical distinction is important because the etiology, natural history, and therapy of thoracic aneurysms differ for each of these segments. Aneurysms of the descending aorta occur most commonly (Figure 1.7), followed by aneurysms of the ascending aorta, whereas arch aneurysms occur much less often.

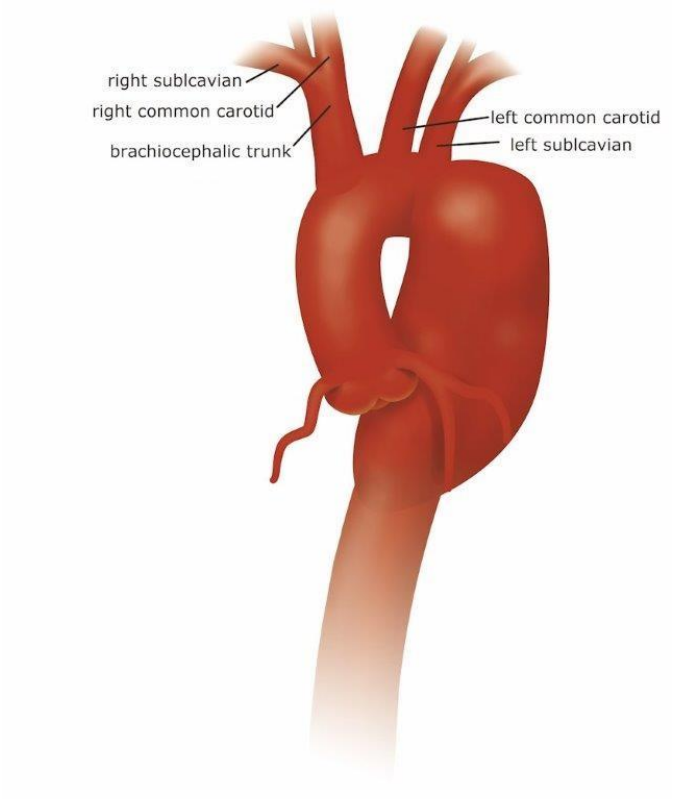

Figure 1.7. Descending Aortic Aneurysm

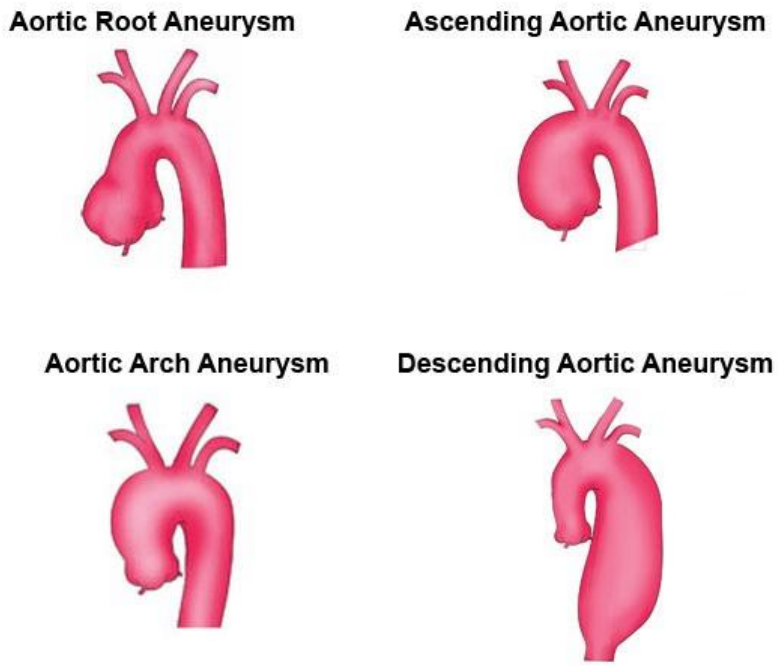

Figure 1.8. Thoracic Aortic Aneurysms.[16]

In addition, descending thoracic aneurysms may extend distally to involve the abdominal aorta, creating what is known as a *thoracoabdominal aortic aneurysm*. Sometimes the entire aorta may be ectatic, with localized aneurysms seen at sites in both the thoracic and abdominal aorta.

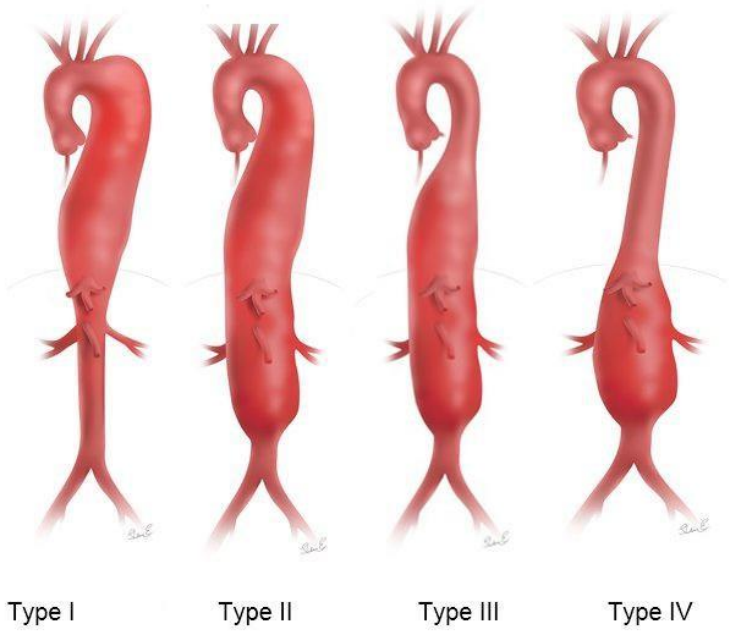

Figure 1.9. Thoracoabdominal aneurysms (Crawford Classification).[17]

1.4.4 Etiology and pathogenesis

Aneurysms of the ascending thoracic aorta most often result from the process of *cystic medial degeneration (or cystic medial necrosis)*. Histologically cystic medial degeneration has the appearance of smooth muscle cell necrosis and elastic fiber degeneration, with the appearance in the medial of cystic spaces filled with mucoid material. Although these changes occur most frequently in the ascending aorta, in some cases the entire aorta may be similarly affected. The histological changes lead to weakening of the aortic wall, which in turn results in the formation of a fusiform aneurysm. Such aneurysms often involve the aortic root and may consequently result in aortic regurgitation. The term annuloaortic ectasia is often used to describe this condition.

Cystic medial degeneration is found in virtually all cases of the Marfan syndrome and may be associated with other connective tissue disorders as well, such as Ehlers-Danlos syndrome. The Marfan syndrome is an autosomal dominant heritable disorder of connective tissue that has recently been discovered to be due to mutations of one of the genes for fibrillin, a structural protein that helps to direct and orient elastin in the developing aorta. These mutations result in a decrease in the amount of elastin in the aortic wall, together with a loss of the elastin's normally highly organized structure. As a consequence, from an early age the marfanoid aorta exhibits markedly abnormal elastic properties and increased systemic pulse wave velocities, and over time the aorta exhibits progressively increasing degrees of stiffness and dilatation.

In those patients without the Marfan syndrome, however, it is not possible to recognize the histological diagnosis of cystic medial degeneration prospectively (i.e., without surgery or necropsy). This fact has

significantly limited our understanding of medial degeneration and its natural history, and it remains unclear to what extent this this syndrome may represent an independent disease process versus a manifestation of another disease state. It has long been suspected that some patients who have annuloaortic ectasia and proven cystic medial degeneration without the classic phenotypic manifestations of the Marfan syndrome may, in fact, have a variation or forme fruste of the Marfan syndrome, although this remains unproved. On the contrary, many patients with ascending thoracic aneurysms appear to have nothing more than idiopathic cystic medial degeneration.

ATHEROSCLEROSIS. Atherosclerotic aneurysms infrequently occur in the ascending aorta and when they do, tend to be associated with diffuse aortic atherosclerosis.

Aneurysms in the aortic arch are often contiguous with aneurysms of the ascending or descending aorta. They may be due to atherosclerotic disease, cystic medial degeneration, syphilis, or other infections. The predominant cause of aneurysms of the descending thoracic aorta is atherosclerosis. These aneurysms tend to originate just distal to the origin of the left subclavian artery and may be either fusiform or saccular. The pathogenesis of such atherosclerotic aneurysms in the thoracic aorta may be similar to that of abdominal aneurysms but has not been extensively examined.

SYPHILIS. This was once a common cause of ascending thoracic aortic aneurysm, but today it has become a rarity in the most major medical centers as a result of aggressive antibiotic treatment of the disease in its early stages. The latent period from initial spirochetal infection to aortic complications may range from 5 to 40 years is most commonly 10 to 25 years. During the secondary phase of disease there is a direct spirochetal infection of the aortic media, most commonly involving the ascending aorta. The muscular and elastic media elements are destroyed by the infection and inflammatory response and replaced by fibrous tissue that frequently calcifies. Weakening of the aortic wall from medial destruction results in progressive aneurysmal dilatation. In addition, the infection may spread into the aortic root, and the subsequent root dilatation may result in aortic regurgitation.

INFECTIOUS AORTITIS. This rare cause of aortic aneurysm may result from a primary infection of the aortic wall, causing aortic dilatation with the formation of fusiform or saccular aneurysms. More commonly, infected or *mycotic* aneurysms may arise secondarily from an infection occurring in a preexisting aneurysm of another etiology. When an infected aneurysm involves the ascending aorta, it is often the consequence of direct spread from aortic bacterial endocarditis.

1.4.5 Natural history

Defining the natural history of thoracic aortic aneurysms is complex, given the numerous contributing factors. The cause of an aneurysm may affect both its rate of growth and propensity for rupture. The presence or absence of aneurysm symptoms is another important predictor, as symptomatic patients have a much poorer prognosis than those without symptoms, in large part because the onset of new symptoms is frequently a harbinger of rupture or death. Moreover, the high prevalence of additional cardiovascular diseases in these patients may have a dramatic impact on mortality; in fact, second to aneurysm rupture, the most common causes of death in this population are other cardiovascular diseases.

Several small studies of the natural history of thoracic aortic aneurysms have been reported, but the data are far more limited than those available regarding abdominal aortic aneurysms. In the largest modern series, the 1-, 3-, and 5-year survival rates for patients with thoracic aortic aneurysms not undergoing surgical repair were approximately 65, 36, and 20 per cent, respectively. Aneurysm rupture occurs in 32 to 68 per cent of patients not treated surgically, with rupture accounting for 32 to 47 per cent of all patient deaths. Fewer than half of the patients with rupture may arrive at the hospital alive, as mortality at 6 hours is 54 per cent and at 24 hours reaches 76 per cent. There is no apparent association between thoracic aneurysm location and the risk of death due to rupture.

Because size is an important predictor of the risk of aneurysm rupture, several studies have examined the rate of expansion of thoracic aortic aneurysms. As with abdominal aneurysms, initial size is the only independent predictor of the rate of thoracic aneurysm growth, although some data also suggest that descending thoracic aneurysms may expand more slowly than others. In a recent report, Dapunt et al. followed 67 patients with thoracic aortic aneurysm using serial CT scanning and found a mean rate of expansion of 0.43 cm/year. The only independent predictor of a rapid expansion (greater than 0.5 cm/year) was an initial aortic diameter larger than 5.0 cm: Those aneurysms that were 5.0 cm or smaller showed mean growth rates of 0.17 cm/year, whereas those larger than 5.0 cm grew by 0.79 cm/year. Unfortunately, even when controlling for initial aneurysm size, there was still substantial variation in individual aneurysm growth rates, making such mean growth rates of little value in predicting aneurysm growth for a given patient. More helpful, however, was the finding that growth rates among small aneurysms were more consistent, with only 1 of 25 aneurysms 4.0 cm or less at baseline showing rapid growth. Two additional findings in this series were that no aneurysm smaller than 5.0 cm ruptured during the follow-up period, and that the only variable predictor of survival was initial aneurysm size.

1.4.6 Surgical treatment

The optimal timing of surgical repair of thoracic aortic aneurysms remains uncertain for several reasons. First, as noted above, the available data on natural history of thoracic aneurysms are limited, especially with respect to the outcomes of surgical intervention. Second, with the high incidence of coexisting cardiovascular disease in this population, many patients die of other cardiovascular causes before their aneurysms ever rupture. Finally, significant risks are associated with thoracic aortic surgery, particularly in the arch and descending aorta, which in many cases may outweigh the potential benefits of aortic repair.

Surgery is currently recommended when thoracic aortic aneurysms reach 6.0 cm or larger, or often 7.0 cm or larger in patients at high operative risk. Indications for surgery in smaller aneurysms include rapid rate of expansion, associated significant aortic regurgitation, or the presence of aneurysm-related symptoms. In patients with the Marfan syndrome, given their higher risk of dissection and rupture, repair of thoracic aneurysms is recommend when they reach only 5.5 cm in size. Surgery should be considered

even sooner in Marfan patients at especially high risk, such as those with rapid and progressive aortic dilatation, those with a family history of the Marfan syndrome plus aortic dissection, or women planning pregnancy. Of course, the aggressiveness with which surgical repair is undertaken in any case should be appropriately influenced by the general condition of the individual patient.

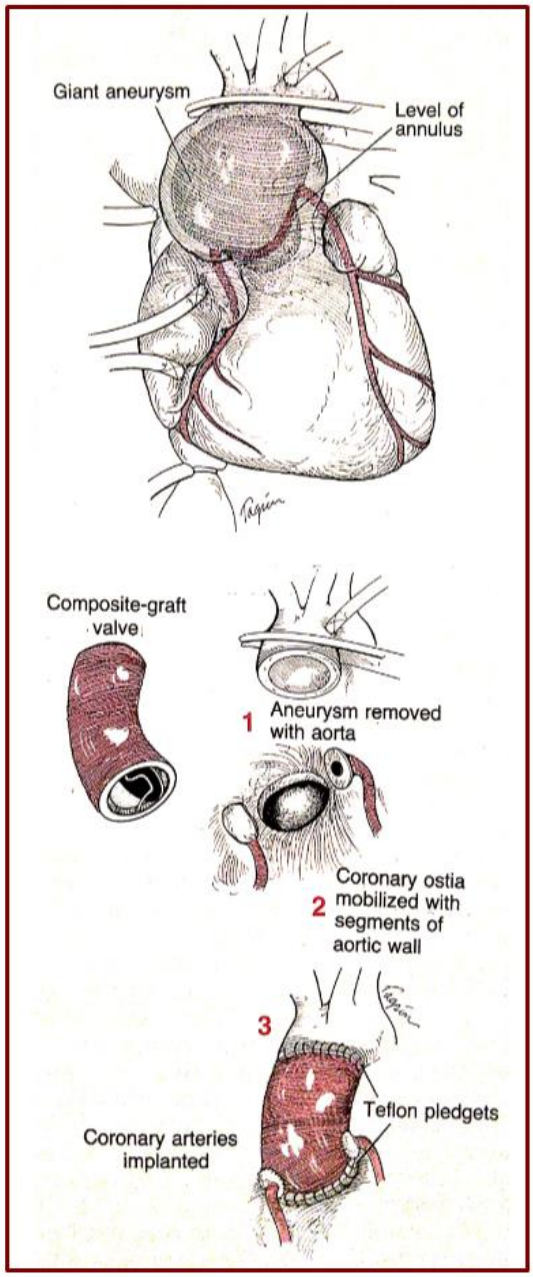

Figure 1.10.Technique for the composite graft replacement of an aneurysm of the ascending aorta.[1]

Thoracic aortic aneurysms are generally resected and replaced with a prosthetic sleeve of appropriate size (Figure 1.10). Cardiopulmonary bypass is necessary for the removal of ascending aortic aneurysms, and partial bypass to support the circulation distal to the aneurysm is often advisable in resection of descending thoracic aortic aneurysms. A temporary Gott shunt may be used from the proximal aorta to the aorta beyond the aneurysm in order to perfuse the distal circulation while the aortic site being repaired is cross-clamped. The use of such adjuncts is less important, however, than the nature and extent of the aneurysm in determining the incidence of postoperative complications.

The use of a composite graft consisting of a Dacron tube with a prosthetic aortic valve sewn into one end (Bentall procedure) is generally the method of choice in treating ascending thoracic aneurysms involving the root which are associated with significant aortic regurgitation. The valve and the graft are directly sewn into the aortic annulus, and the coronary arteries then reimplanted into the Dacron aortic graft (Figure 1.10). The operative risk for mortality is about 5 per cent. For those patients with structurally normal aortic valve leaflets whose aortic regurgitation is secondary to dilatation of the root, David et al. have successfully repaired the native valve by either reimplanting it in a Dacron graft or reconstructing the aortic root. In a recent series 41 of 45 patients had mild or no aortic regurgitation after this method of aortic valve repair and were stable at a mean of 18 months.

Aneurysms of the aortic arch may be successfully excised surgically, but the procedure may be particularly challenging. The brachiocephalic vessels must be removed from the aortic arch prior to its resection. Then, after interposition of the prosthetic tube graft, the island of native aortic tissue containing the brachiocephalic vessels is reimplanted into the graft and normal cerebral perfusion restored. There is, however, a significantly increased risk of stroke secondary to variable periods of cerebral ischemia. The incidence of stroke in recent series is 3 to 7 per cent. The standard method for carrying out this operation today is with the use of profound hypothermic circulatory arrest, as introduced by Griepp et al. in 1974.

Some have attempted to add selective cerebral perfusion during aneurysmectomy, but cannulation techniques are difficult. In fact, the incidence of stroke may actually be as high or higher with this method, possibly due to cannulation-induced cerebral emboli. 96,99 A more recent adjunct for cerebral protection during hypothermic arrest is the use of retrograde cerebral perfusion via a superior vena cava cannula.95 Not only does this technique provide nutrients and oxygen to the brain,100 but it may also serve to flush out both air and particulate matter from the cerebral and carotid arteries that would otherwise embolize. The results of retrograde cerebral perfusion have thus far been quite encouraging, with trends toward lower stroke rates in recent reports.

More than half of the patients undergoing surgical repair of a thoracic aortic aneurysm in Crawford's series had multiple aortic segments involved, and almost three-quarters of those with descending thoracic aneurysms had multiple involvement. Such widespread aneurysmal dilatation of the aorta presents a particular challenge to the surgeon and often precludes operation. However, Crawford et al. have demonstrated that it is possible to successfully replace virtually the entire diseased thoracic and abdominal aorta. A method known as the "elephant trunk" technique, carried out in sequential stages of aortic replacement, has been shown to facilitate such extensive surgical procedures and reduce the associated risks.

Elective surgical repair of ascending and descending thoracic aortic aneurysms has a 90 to 95 per cent early survival rate in most centers. Major complications are technical, especially hemorrhage from tearing of the diseased aorta. A catastrophic complication of resection of descending thoracic aneurysms is postoperative paraplegia secondary to interruption of the blood supply to the spinal cord. The incidence of paraplegia ranges from 0 to 17 per cent, although most series show an incidence of about 5 to 6 per cent. A number of methods have been proposed to reduce the likelihood of paraplegia, although none has proved to be consistently safe and effective. One of the more promising techniques involves maintaining distal aortic perfusion during surgery with the use of the heparinless Gott shunt (aorta-aorta bypass). Although some groups have achieved good success with such techniques, others have had mixed results. Controlled trials might better clarify the efficacy of these techniques.

An alternative approach of the surgical management of descending thoracic aneurysms, as recently reported by Dake et al., is the use of a transluminally placed endovascular stent-graft. This technique has the advantage of being far less invasive than surgery and has the potential of reducing the incidence of paraplegia from surgically induced spinal cord ischemia. The authors report successful device employment in all 14 of their patients, with documented thrombosis of the residual aneurysm lumen surrounding the stent-graft in 12. Although still experimental at present, such a device may in the future have an important role in the management of patients who are at risk for aortic rupture but are otherwise poor surgical candidates. Unfortunately, the curvilinear nature of the ascending aorta and arch makes application of similar techniques to aneurysms of these proximal aortic segments far more problematic.

Complications of associated atherosclerosis, such as myocardial infraction, cerebrovascular accidents, and renal failure, often become manifested under a massive physiological stress of aortic surgery. The most frequent causes of early postoperative death are myocardial infraction, congestive heart failure, stroke, renal failure, hemorrhage, respiratory failure, and sepsis. Advanced age, emergency operation, prolonged aortic cross-clamp time, extent of the aneurysm, diabetes, prior aortic surgery, aneurysm symptoms, and intraoperative hypotension are the most important factors determining perioperative morbidity and mortality. Many patients with atherosclerotic aneurysms are heavy smokers, and pulmonary

complications following surgery are common. The left lung may be severely traumatized by compression during resection of large aneurysms of the descending thoracic aorta, a complication that may seriously jeopardize the patient's survival, particularly in the setting of underlying pulmonary disease.

Late deaths are usually associated with cardiac complication, aneurysm rupture, respiratory failure, or stroke. Aneurysm rupture may be due to aneurysm formation at the graft margins or the appearance of new aneurysms at other aortic sites.

2. Defining the problem

2.1 Introduction

As stated above, there are significant risks associated with thoracic aortic surgery, particularly in the arch and descending aorta, which in many cases may outweigh the potential benefits of aortic repair. The two complications which are most important are rupture and dissection. To know when these complications occur would permit rational decision-making regarding elective, preemptive surgical intervention. It should be emphasized that these criteria apply to asymptomatic aneurysms while symptomatic aneurysms should be resected regardless of size.

Throughout the years, absolute aneurysm size has been used as the primary predictor of negative events. Surgical intervention is usually recommended as soon as the maximal diameter of the aorta reaches a certain limit. This limit varies slightly from study to study and depending on the location of the aneurysm along the aorta, the number can be different (e.g. 5.5 cm for the ascending and 6.5 cm for the descending aorta [7]). However, changes in risk, based on patient size, had never been demonstrated, until 2006, where Davies R.R. and colleagues carried out a study in which they tried to define the impact of body surface area (BSA) on aortic complications [8]. In the course of this study, they developed a new measurement, the aortic size index (ASI), which takes into account both aortic diameter and BSA. The aortic size index was calculated as: ASI = aortic diameter (cm) divided by body surface area (m^2). Body Surface Area was calculated using the Dubois and Dubois formula:

$$0.20247 * \left(wgt^{0.425} * \left(\frac{hgt}{100} \right)^{0.725} \right) \qquad (1)$$

Throughout all methods of their analysis, ASI was a better predictor of negative events (rupture, dissection, or death) than maximal aortic diameter. Conclusively, it was recommended that the patient should undergo elective operative repair before they enter the zone of moderate risk with ASI greater than 2.75 cm/m^2.

The interaction between BSA and aortic size is shown in Table 2.1.

	Aortic size (cm)									
BSA	**3.5**	**4.0**	**4.5**	**5.0**	**5.5**	**6.0**	**6.5**	**7.0**	**7.5**	**8.0**
1.30	2.69	3.08	3.46	3.85	4.23	4.62	5.00	5.38	5.77	6.15
1.40	2.50	2.86	3.21	3.57	3.93	4.29	4.64	5.00	5.36	5.71
1.50	2.33	2.67	3.00	3.33	3.67	4.00	4.33	4.67	5.00	5.33
1.60	2.19	2.50	2.80	3.13	3.44	3.75	4.06	4.38	4.69	5.00
1.70	2.05	2.35	2.65	2.94	3.24	3.53	3.82	4.12	4.41	4.71
1.80	1.94	2.22	2.50	2.78	3.06	3.33	3.61	3.89	4.17	4.44
1.90	1.84	2.11	2.37	2.63	2.89	3.16	3.42	3.68	3.95	4.22
2.00	1.75	2.00	2.25	2.50	2.75	3.00	3.25	3.50	3.75	4.00
2.10	1.67	1.90	2.14	2.38	2.62	2.86	3.10	3.33	3.57	3.80
2.20	1.59	1.82	2.05	2.27	2.50	2.72	2.95	3.18	3.41	2.64
2.30	1.52	1.74	1.96	2.17	2.39	2.61	2.83	3.04	3.26	3.48
2.40	1.46	1.67	1.88	2.08	2.29	2.50	2.71	2.92	3.13	3.33
2.50	1.40	1.60	1.80	2.00	2.20	2.40	2.60	2.80	3.00	3.20

= low risk (~4% per yr)
= moderate risk (~8% per yr)
= severe risk (~20% per yr)

Table 2.1. Risk of Complications by Aortic Diameter and Body Surface Area with Aortic Size Index Given Within Chart. [8]

What is more, recent studies reveal that the actual stress distribution is more dependent on the individual specific shape of an aneurysm, thus assessing risk of rupture judging only by the diameter is not a reliable criterion [4].

However, the aim of this study is to examine aneurysm size alone and so it was decided to remove shape as a parameter. In order to achieve this goal, we designed idealized aortic models with ascending thoracic aneurysm (aTAA), assuming a fusiform and completely spherical aneurysm. All of the models were designed similarly, changing only the diameter of the aneurysm.

In particular, we designed four different models of an aneurysmatic thoracic aorta that represent four different BSA values (1.65 m^2, 1.85 m^2, 2.0 m^2, 2.2 m^2). For each one of these four models we examine different cases of maximal aortic diameter corresponding to an ASI of the moderate risk zone up until the severe risk zone.

The purpose is to examine how does the interaction between BSA and maximal aorta diameter define risk of rupture in a fusiform aneurysm of the ascending aorta and confirm the results of Davies' study but also obtain an understanding of where exactly does the rupture happen and under which pressure condition.

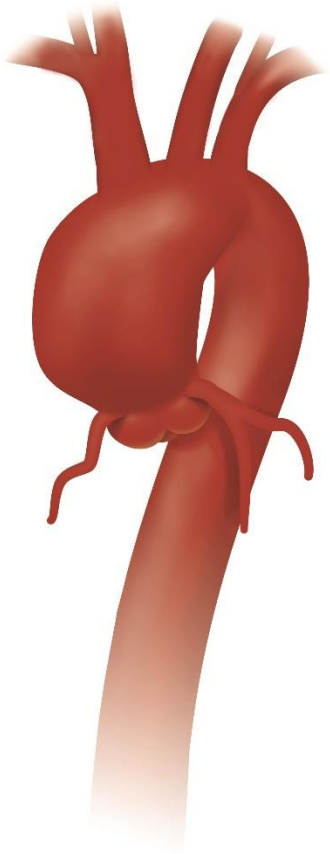

Figure 2.1. Ascending Thoracic Aortic Aneurysm (aTAA)

The process of collecting and calculating the geometrical data that were used to design these aortic models, is described, in detail, in the next pages.

2.2 Data collection and processing

2.2.1 Age determination

In 2013, Turkbey and colleagues [18] developed a formula for predicting the mean luminal diameter of the ascending aorta, at the level of the right pulmonary artery:

If the subject is a male the formula is:

$$D_{PA} = 14.99 + 0.12 * age + 1.79 + 4.63 * BSA \quad (2)$$

If the subject is a female then it becomes:

$$D_{PA} = 14.99 + 0.12 * age + 4.63 * BSA \quad (3)$$

However, sex was not considered a parameter during this analysis, on the grounds that the differences between male and female aortic diameters are negligible. And so, the mean luminal diameter of the ascending aorta was calculated as the average of the male and female diameter.

As shown in the equations above, the data needed to calculate the diameter at PA (Pulmonary Artery) level are age and BSA. In order to determine the age of the control case, we compiled data taken from six articles from scientific literature [19-24]. These articles refer to studies about ascending thoracic aortic aneurysms (aTAAs) and each one of them examines different samples of patients with different mean age. Combining the mean age of every study along with the mean standard deviation and with the use of the formulas below we determined a global age equal to **66.25 ± 9.588,** which is going to be used as the control case.

$$pooled\ mean = \frac{\sum_{i=1}^{k} n * x_i}{\sum_{i=1}^{k} n} \quad (4)$$

$$pooled\ standard\ deviation = \sqrt{\frac{\sum_{i=1}^{k} (n-1) * {s_i}^2}{\sum_{i=1}^{k} n - k}} \quad (5)$$

Where, x_i is the mean age of group i, n is sample size of group i, k is the number of samples (6) and s_i is the standard deviation

2.2.2 Calculation of aortic diameter at diaphragm level

In 2010, Hickson and colleagues [2], published a paper in which they tried to determine the impact of age on regional aortic pulse wave velocity (aPWV). For the needs of this study, a total of 162 subjects, aged 18 to 77 years and free of cardiovascular disease and medication, were recruited from the Anglo-Cardiff Collaborative Trial. Cine phase contrast magnetic resonance imaging was performed at 5 aortic levels: the ascending aorta (L1), located 1 cm distal to the aortic valve; the descending aorta (L2), in line with L1; at

the level of the diaphragm (L3); 3 cm above the level of the aortic bifurcation (L5), and midway between L3 and L5 (L4) (Figure 2.2). Systolic diameter and average blood flow were measured at each level and

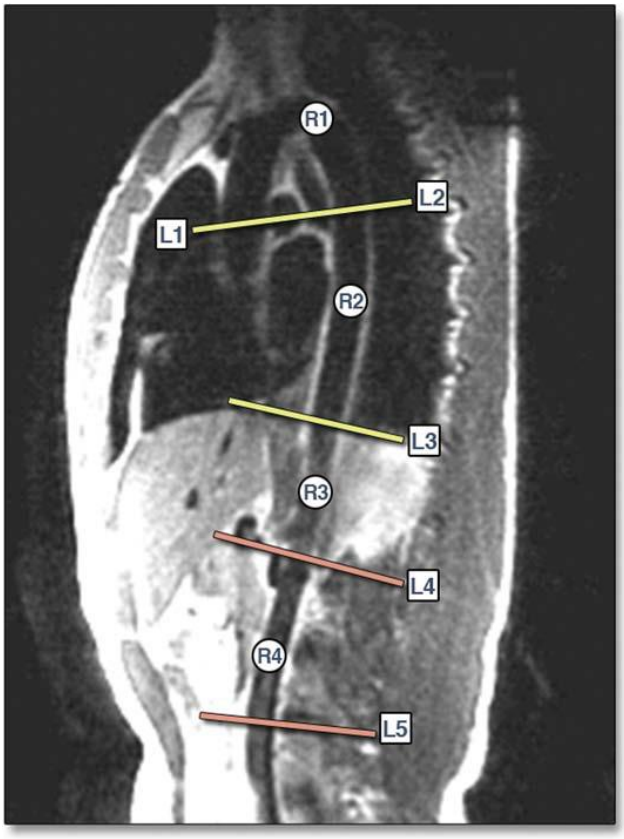

Figure 2.2. Sagittal Image of the Aorta from the Aortic Root to the Level of the Bifurcation.[2] L1 through L5 indicate the level of cine phase contrast magnetic resonance imaging image acquisition, and R1 through R4 indicate the region of pulse wave velocity measurement.

regional aPWV (regional aPWV measured by cine phase contrast magnetic resonance imaging) determined in 4 aortic segments: the arch (R1), the thoracic-descending aorta (R2), mid-descending aorta (R3), and the abdominal aorta (R4) and across the entire aorta. (Figure 2.2)

Age-related variation in aortic diameter. The average systolic diameters decreased moving distally (L1 to L5: 3.1 ± 0.4 cm, 2.3 ± 0.3 cm, 2.1 ± 0.3 cm, 1.9 ± 0.2 cm, and 1.7 ± 0.2 cm, respectively). Average systolic aortic diameters were greater in male than female subjects at all levels ($p < 0.01$). Values for L1 to L5 were 3.2 ± 0.3 cm, 2.5 ± 0.2 cm, 2.2 ±0.3 cm, 2.0 ± 0.2 cm, and 1.8 ± 0.3 cm in male subjects and 3.1 ± 0.4 cm, 2.3 ± 0.3 cm, 2.0 ± 0.4 cm, 1.8 ± 0.2 cm, and 1.8 ± 0.2 cm in female subjects. However, when adjusted for body surface area, the difference between sexes was eliminated. Systolic diameter at each aortic level correlated positively with age ($r = 0.25$ to 0.5, $p < 0.001$ for all levels). The greatest variation in aortic diameter as a function of age occurred in the ascending aorta, L1 (0.96 mm higher per decade), followed by L3 (0.85 mm higher per decade), L2 (0.78 mm higher per decade), L4 (0.64 mm higher per decade), and L5 (0.37 mm higher per decade, $p < 0.001$ for all levels) (Figure 2.3). Because, theoretically, increasing diameter offsets the effect of higher wall stiffness on PWV, the wall stiffness was calculated using the Moens-Korteweg equation, assuming a constant wall thickness. Although wall thickness does increase

with age, this is a very modest change, and this effect in the examined population was minimized by the inclusion of only healthy individuals. The impact of age on wall stiffness was very similar to that observed for aPWV, with the largest difference in the abdominal aorta and least in the proximal region.

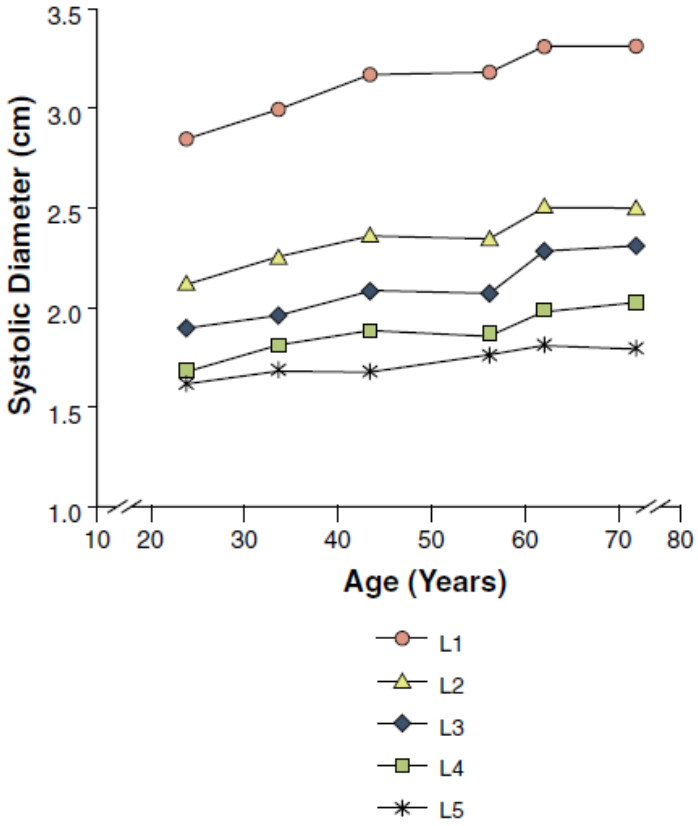

Figure 2.3. Association between Age and Systolic Diameter.

Age related variation in aortic length. It was found that the whole aorta was longer in older subjects (8 mm/decade, r = 0.36, p<0.001). This was entirely due to the longer length of the aortic arch (R1) (8 mm longer per decade, p < 0.001), as the other aortic segments remained constant with age (Figure 2.4). This trend remained when aortic length was adjusted for height and for body surface area.

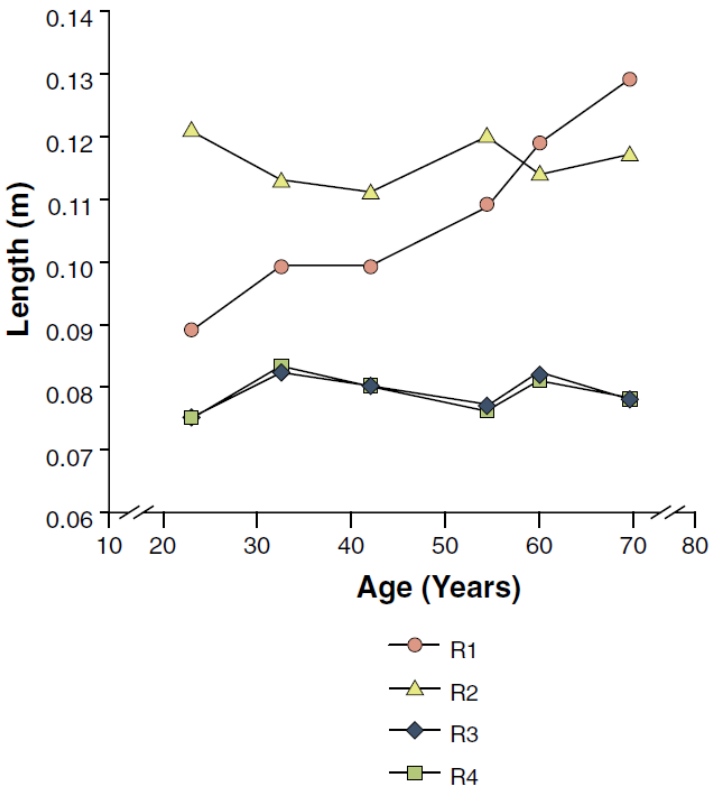

Figure 2.4. Association between Age and Aortic Length.[2]

Using an online tool WebPlotDigitizer[1] we digitized curve L3 from Figure 2.3. After exporting the data into Grapher[2] - a scientific graphing software - we performed a linear regression on the data for the ages 60 to 69 years old. We obtain the following expression for the aortic diameter at diaphragm level:

$$D_d = 0.00252684793 * age + 2.128285285 \quad (6)$$

Since the data that was used to derive the above formula corresponds solely to the age group 60 to 69 y.o., it becomes obvious that according to Table 2.2 this formula refers only to BSA=1.9 m^2.

Thus, for BSA = 1.9 m^2 we get D_d = 22.9568896 mm

[1] *Rohatgi Ankit, WebPlotDigitizer 4.3; https://automeris.io/WebPlotDigitizer*
[2] *Grapher™ from Golden Software, LLC (www.goldensoftware.com)*

Characteristic	Age Group					
	20–29 Yrs	30–39 Yrs	40–49 Yrs	50–59 Yrs	60–69 Yrs	70–79 Yrs
Age, yrs	24 ± 3	34 ± 3	45 ± 2	57 ± 3	63 ± 3	73 ± 2
Sex, male/female	11/17	11/12	11/16	13/13	14/16	11/12
Height, m	1.71 ± 0.09	1.71 ± 0.09	1.67 ± 0.10	1.68 ± 0.10	1.70 ± 0.09	1.66 ± 0.10
Weight, kg	67.0 ± 11.9	73.8 ± 10.5	73.0 ± 15.0	73.4 ± 13.3	75.2 ± 13.4	69.2 ± 10.3
BMI, kg/m^2	23 ± 3	25 ± 3	25 ± 4	26 ± 4	26 ± 4	25 ± 2
BSA, m^2	1.8 ± 0.2	1.9 ± 0.2	1.8 ± 0.2	1.8 ± 0.2	1.9 ± 0.2	1.8 ± 0.2
HR, beats/min	63 ± 10	62 ± 7	67 ± 9	67 ± 10	69 ± 12	69 ± 10
Supine systolic BP, mm Hg	115 ± 12	121 ± 7	126 ± 16	120 ± 11	130 ± 18	137 ± 19
Supine diastolic BP, mm Hg	70 ± 8	77 ± 5	78 ± 9	75 ± 7	78 ± 8	78 ± 12
Supine MAP, mm Hg	85 ± 8	92 ± 5	94 ± 11	90 ± 8	95 ± 10	98 ± 13
Supine central systolic BP, mm Hg	98 ± 10	103 ± 7	112 ± 13	107 ± 12	118 ± 15	125 ± 14
Total cholesterol, mmol/l	4.3 ± 0.9	4.7 ± 0.8	5.0 ± 0.8	5.5 ± 1.0	5.4 ± 1.0	5.7 ± 1.1
LDL, mmol/l	2.5 ± 0.8	2.7 ± 0.5	2.9 ± 0.7	3.4 ± 0.9	3.4 ± 0.7	3.6 ± 0.8
HDL, mmol/l	1.5 ± 0.4	1.6 ± 0.3	1.6 ± 0.4	2.5 ± 4.6	1.4 ± 0.3	1.5 ± 0.5
Glucose, mmol/l	4.1 ± 0.6	4.2 ± 0.7	4.4 ± 0.7	4.5 ± 1.1	4.5 ± 1.0	4.6 ± 0.8

Table 2.2. Subject Characteristics (BMI = body mass index; BP = blood pressure; HDL = high-density lipoprotein; HR = heart rate; LDL = low-density protein; MAP = mean arterial pressure.)

In order to calculate the diameter at the diaphragm level L3 for the BSA values that we examine, we assume that there is a constant ratio between D_d and D_{PA}. We calculate the percentage:

$$a = \frac{D_d}{D_{PA}}(\%) \qquad (7)$$

2.2.3 Calculation of total aortic length

In 2019, Sorimachi and colleagues published a study in which they examined the CT data of 443 patients. After computing the aortic length and volume of the patient cases, they performed linear regression analyses to assess the independent contributions of sex and its interaction with left ventricular (LV) function before and after adjusting for the CT-derived aortic length and volume. In the seventh page of their publication, a diagram is placed that shows the relationship between aortic length and BSA for both

men and women (Figure 2.5). The aortic length is measured by plotting the center of the vessel lumen from the sinotubular (ST) junction to the aortic bifurcation

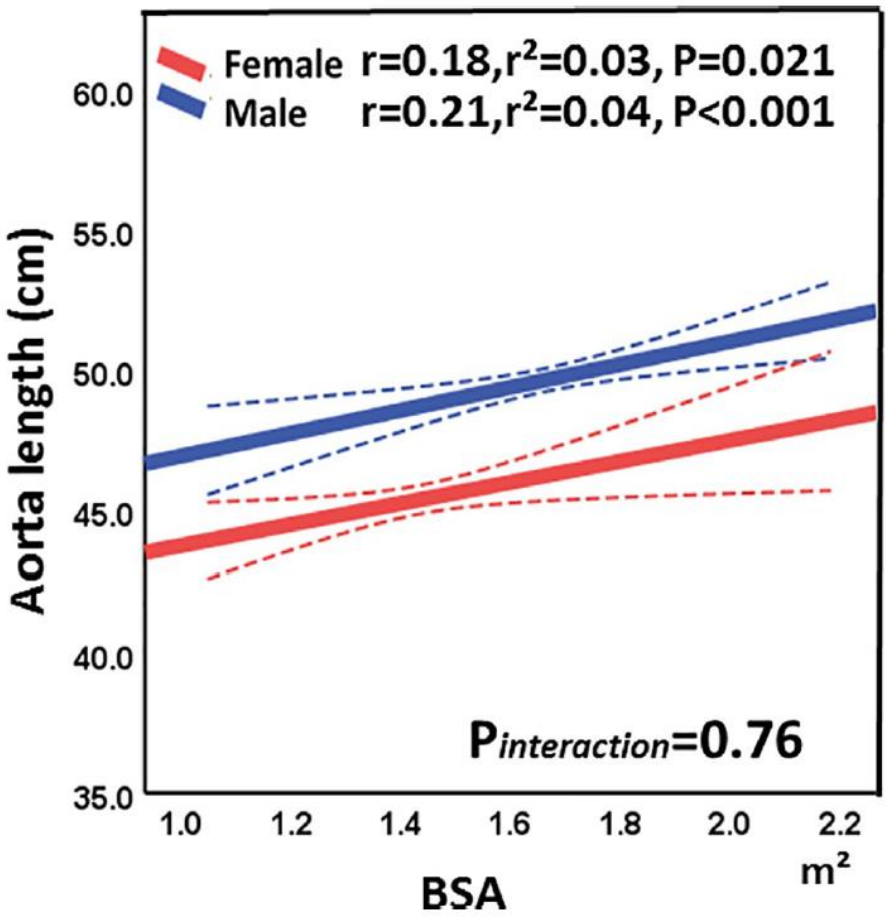

Figure 2.5. Association of aorta length and body surface area (BSA). [25]

We digitize Figure 2.5 and calculate the average of those two curves, thus eliminating the gender parameter. As a result, we extract a mathematical relationship between total aortic length and BSA:

$$L_{tot} = 3.936097259 * BSA + 41.51621962 \quad (8)$$

Where L_{tot} represents the total aortic length measured from the ST junction to the aortic bifurcation.

In this way, the different aortic lengths L_{tot} for the examined BSA values could be calculated.

The relationship above applies to the age of 73 (as shown in Table 2.3) since this is the average age of the sample examined by Sorimachi. However, these lengths are not what we need for this study as our goal is to calculate the characteristics for the age of 66.25. This creates the need to build a factor that will allow us to reduce these lengths to lengths that apply to the age we want.

	WHOLE sample(n = 443)				AGE-MARCHED sample(n = 324)		
	Overall (n = 443)	Male (n = 274)	Female (n = 169)	p value	Male (n = 162)	Female (n = 162)	p value
Age, years	73(65, 81)	72(65, 80)	74(66, 83)	0.062	74(67, 82)	74(66, 82)	0.58
Height, cm	159±10	164±7	151±7	<0.001	163±7	151±7	<0.001
Weight, kg	57±13	61±12	50±10	<0.001	59(52, 67)	49(44, 56)	<0.001
Body surface area, m^2	1.6±02	1.7±0.2	1.4±0.2	<0.001	1.64(1.54, 1.74)	1.43(1.34, 1.55)	<0.001
Body mass index, kg/m^2	22.4±3.8	22.7±3.9	22.0±3.7	0.081	22.4(19.8,24.7)	21.9(1.94, 24.8)	0.48
Comorbidities							
Hypertension	239(54)	150(54)	89(53)	0.67	95(58)	86(53)	0.29
Diabetes mellitus	109(25)	80(29)	29(17)	0.004	49(30)	29(17)	0.009
Dyslipidemia	112(25)	78(29)	34(20)	0.050	48(29)	34(21)	0.074
Ischemic heart disease	71(17)	55(20)	16(10)	0.003	31(19)	16(10)	0.020
Smoking	207(47)	177(65)	30(18)	<0.001	105(65)	30(18)	<0.001
Hb, mg/dl	12.3±2.3	12.7±2.4	11.8(10.4,13.0)	<0.001	12.3±2.4	12.0±1.9	0.004
Creatinine, mg/dl	0.78(0.64,1.01)	0.89(0.73,1.13)	0.68(0.55,0.96)	<0.001	0.91(0.74, 1.18)	0.68(0.55, 0.86)	<0.001
eGFR, $mL/min/1.73\ m^2$	68.0±25.5	67.3±24.7	69.3±26.9	0.43	65.0±24.6	68.9±25.3	0.19
BNP, pg/ml†	49.2(21.7, 136.7)	39.6(18.8, 116.8)	72.5(31.2, 196.5)	0.008	48.4(22.4,136.0)	70.0(31.2, 200.2)	0.14
Medications							
Aspirin	67(15)	47(17)	20(12)	0.13	23(15)	18(11)	0.41
Clopidegrel	56(13)	39(14)	17(10)	0.20	29(18)	17(11)	0.062
Ca-blocker	144(32)	89(33)	55(32)	0.89	40(25)	51(32)	0.58
Beta-blockers	64(15)	43(16)	21(13)	0.36	23(14)	22(14)	0.82
ACEIs/ARBs	104(24)	63(23)	41(24)	0.78	39(24)	38(23)	0.86
Diuretics	46(10)	30(11)	16(10)	0.61	21(13)	12(8)	0.13
Statins	84(19)	59(22)	25(15)	0.073	34(21)	25(15)	0.20
Hemodynamic Parameters							
Heart rate, beats/min.	71(61, 81)	70(60, 79)	73(64, 82)	0.039	70(60, 79)	73(64, 83)	0.044
Systolic BP, mmHg	128(114, 141)	128(113, 140)	129(114, 144)	0.28	128(113, 141)	130(115,146)	0.20
Diastolic BP, mmHg	72(63, 83)	72(63, 83)	72(63, 83)	0.93	71(61, 82)	73(63, 84)	0.14
mean BP, mmHg	90(81, 103)	90(81, 103)	91(81, 102)	0.78	89(79, 102)	92(81, 103)	0.20
Pulse pressure, mmHg	54(45, 64)	53(44, 63)	55(46, 66)	0.18	55(45, 64)	55(46, 66)	0.79
Ea, mmHg/ml	2.6(2.1, 3.1)	2.3(1.9, 2.9)	3.0(2.5, 3.6)	<0.001	2.4(1.9, 2.9)	3.0(2.5, 3.7)	<0.001
SVRI, $dyne{\cdot}m^2/s{\cdot}cm^{-5}$	3580(2924, 4611)	3562(2867, 4509)	3597(3020, 4706)	0.50	3497(2819, 4452)	3642(3037, 4841)	0.17
Arterial compliance, ml/ mmHg	0.83(0.65, 1.08)	0.93(0.74, 1.17)	0.70(0.55, 0.87)	<0.001	0.91(0.73, 1.15)	0.70(0.56, 0.89)	<0.001
baPWV, cm/sec‡	1796(1589, 2097)	1777(1536, 2037)	1872(1648, 2142)	0.26	1791(1537, 2001)	1880(1669, 2192)	0.18

Table 2.3. Clinical characteristics of the examined sample in Sorimachi's study. [25]

2.2.4 Age transform coefficient

The first step for the construction of the age transform coefficient was to digitize the R1 curve from Figure 2.4. We extracted the points that corresponded to ages over 60 and applied a linear regression. The following straight line expression emerged:

$$L_{R1} = 0.1059821792 * age + 5.533805351 \quad (9)$$

What this line represents is the change in L_{R1} length depending on age and so the length for the age of 66.25 can be derived from this.

We follow the same procedure for the curves R2, R3, R4 only this time after the export of the points, we apply a linear regression in a way that a straight line parallel to the horizontal axis emerges, expressing in this way the fact that the length of the segments represented by the curves R2, R3, R4 remains the same throughout the years. As a result, we only get these three numbers:

L_{R2} =11.59 cm

L_{R3} =7.91 cm

L_{R4} =7.90 cm

In order to calculate the entire length of the aorta from the aortic valve to the aortic bifurcation for the age of 66.25 the following equation is created:

$$L_{tot,66.25} = 1\ cm + L_{R1,66.25} + L_{R2} + L_{R3} + L_{R4} + 3\ cm \quad (10)$$

Similarly, for the age of 73, we calculate L_{R1} while the rest of the sections retain their length, and so we derive:

$$L_{tot,73} = 1\ cm + L_{R1,73} + L_{R2} + L_{R3} + L_{R4} + 3\ cm \quad (11)$$

As can be seen, we add 1cm and 3cm in order to calculate the entire aortic length. The reason for this is that, as mentioned in subchapter 2.2.2, the length of the aortic segment R1 is measured 1cm distal to the valve and the length of R4, 3 cm above the level of the aortic bifurcation.

Eventually, the reduction factor can be described by the equation bellow:

$$age\ transformation\ coefficient = \frac{L_{tot,73} - L_{tot,66.25}}{L_{tot,73}} \quad (12)$$

With the help of this factor, the lengths derived from equation (8) which apply to age 73, can be reduced to lengths that apply to the age of 66.25

2.2.5 Cross section tapering

The next pages describe the steps followed in order to calculate the decrease in the aortic diameter from the valve until the aortic bifurcation.

Overall, according to Fung Y.C. [26], the aorta may be described as tapered. The change of area fits the exponential equation:

$$A = A_0 * e^{-\frac{B*x}{R_0}} \quad (13)$$

where *A* is the area of the aorta, A_0 and R_0 are, respectively, the area and radius at the upstream site, *x* is the distance from that upstream site, and *B* is a "taper factor".

This can be transformed into:

$$\pi R^2 = \pi R_0^2 * e^{\frac{B*x}{R_0}} \rightarrow R^2 = R_0^2 * e^{-B\frac{x}{R_0}}$$

It becomes evident that the parameters that need to be calculated are B and R_0 and in order to do so, we have to construct two equations, at least.

At the level of the pulmonary artery bifurcation, we get:

$$R_{PA}^2 = R_0^2 * e^{-B\frac{x_{PA}}{R_0}} \quad (14)$$

Where, x_{pa} and R_{PA} are known variables that have been previously computed.

Likewise, at the level of the diaphragm (L3-according to Hickson):

$$R_d^2 = R_0^2 * e^{-B\frac{x_d}{R_0}} \quad (15)$$

Where x_d and R_d are the known variables.

Dividing (14) and (*15*), we get:

$$\frac{R_{PA}^2}{R_d^2} = e^{-B\frac{x_{PA}}{R_0}} * e^{-B\frac{x_d}{R_0}} \rightarrow \left(\frac{R_{PA}}{R_d}\right)^2 = e^{-B\frac{x_{PA}-x_d}{R_0}} \rightarrow \ln\left(\frac{R_{PA}}{R_d}\right)^2 = -B\frac{x_{PA}-x_d}{R_0} \rightarrow$$

$$-\frac{B}{R_0} = \frac{1}{x_{PA}-x_d}\ln\left(\frac{R_{PA}}{R_d}\right)^2 \quad (16)$$

Then, combining (*15*) and (16), we solve for R_0, as such:

$$R_d^2 = R_0^2 * e^{\frac{x_d}{x_{PA}-x_d}\ln\left(\frac{R_{PA}}{R_d}\right)^2} \rightarrow R_0^2 = R_d^2 * e^{-\frac{x_d}{x_{PA}-x_d}\ln\left(\frac{R_{PA}}{R_d}\right)^2} \rightarrow$$

$$R_0 = R_d * \sqrt{e^{-\frac{x_d}{x_{PA}-x_d}\ln\left(\frac{R_{PA}}{R_d}\right)^2}} \quad (17)$$

In that way, we compute R_0, that is, the diameter at the beginning of the ascending aorta (level of sinotubular junction) and hence, the cross-sectional area A_0.

Solving for B in (16), yields:

$$B = -\frac{R_0}{x_{PA}-x_d}\ln\left(\frac{R_{PA}}{R_d}\right)^2 \quad (18)$$

Then, by using the exponential formula (13) again we can calculate the cross-sectional areas for various points along the aorta. Resulting from this, the radii of the areas will be used in the construction of the aortic model.

$$R = R_0 * \sqrt{e^{-B\frac{x}{R_0}}} \qquad or \qquad D = D_0 * \sqrt{e^{-B\frac{x}{R_0}}}$$

2.2.6 Thickness and tapering of the aortic wall

In 1969, Westerhof and colleagues [27], designed an electrical analog of the arterial system that consists of 121 segments which are shown schematically in Figure 2.6.

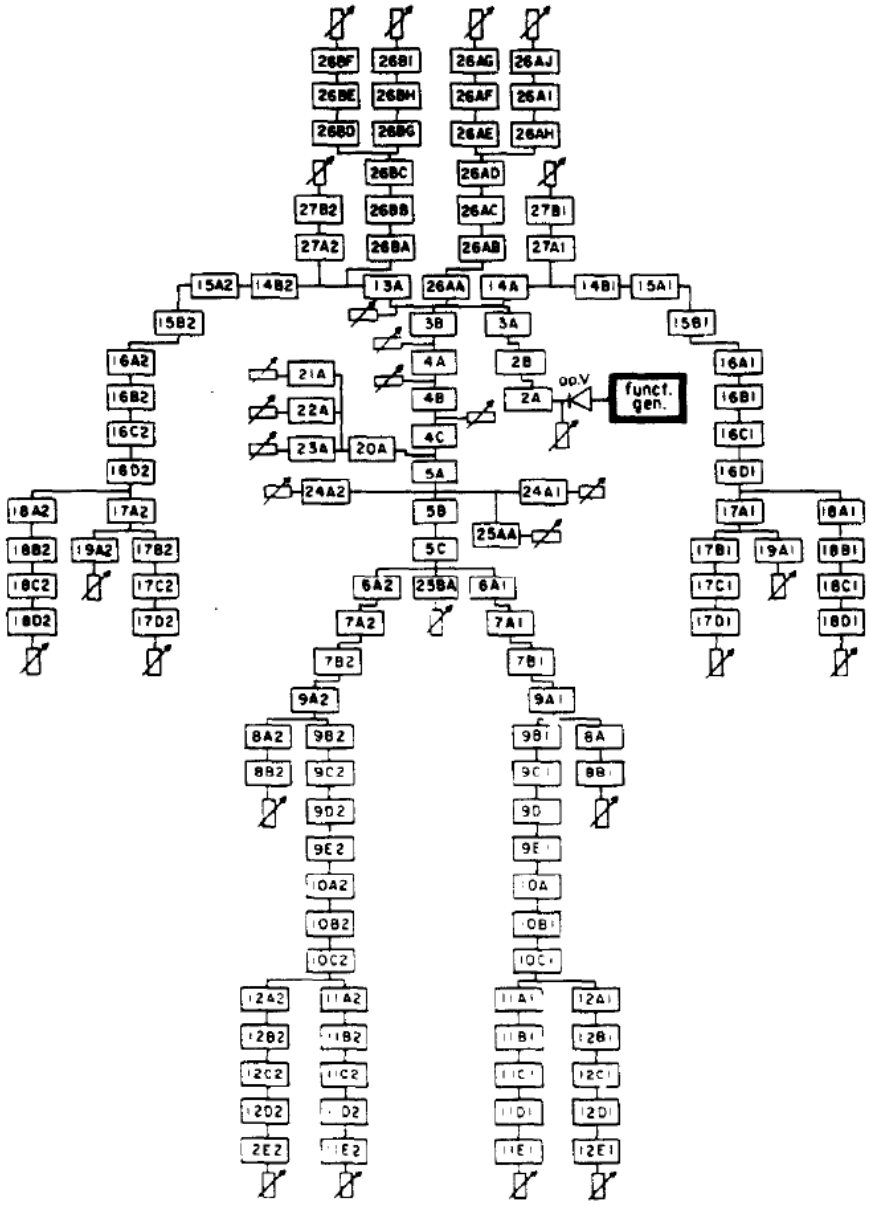

Figure 2.6. Layout of electrical model of the human systemic arterial tree. (Rectangles with arrows represent regional peripheral resistances).

The proximal end of the arterial system is the root of the ascending aorta immediately distal to the aortic valve, but the system does not include the coronary arteries.

The various radii, lengths and detailed data of Young's modulus, together with other relevant data pertaining to the 121 arterial segments represented by the present model, are listed in Table 2.4. These

geometric data are considered representative of a healthy young adult, with a height of 175 cm and a mass of 75 kg.

Notation of segment (*D*: paired segment)		Name of artery	Length of Δz (cm)	Internal radius r (cm)	Wall-thickness h (cm)	Young's modulus (10^6 g cm^{-1}sec^{-2})	Last element in Z_t	Total segment Compliance C (10^{-6} g^{-1} cm^{4}sec^2)	L_1 (g cm^{-4})	R_1 (g cm^{-4} sec^{-1})
	2A	Aorta ascendens	2·0	1·47	0·164	4·0	R_5	53·4	0·309	0·0327
	2B	Aorta ascendens	2·0	1·44	0·161	4·0	R_5	51·0	0·322	0·0358
	3A	Arcus aorta	2·0	1·12	0·132	4·0	R_5	29·6	0·533	0·0971
	3B	Arcus aorta	3·9	1·07	0·127	4·0	R_5	52·1	1·14	0·227
	4A	Aorta thoracalis	5·2	0·999	0·120	4·0	R_5	59·7	1·74	0·397
	4B	Aorta thoracalis	5·2	0·675	0·090	4·0	R_5	25·1	3·82	1·62
	4C	Aorta thoracalis	5·2	0·645	0·087	4·0	R_5	22·5	4·18	2·31
	5A	Aorta abdominalis	5·3	0·610	0·084	4·0	R_5	20·4	4·72	2·88
	5B	Aorta abdominalis	5·3	0·580	0·082	4·0	L_5	18·1	5·28	3·58
	5C	Aorta abdominalis	5·3	0·548	0·078	4·0	L_5	15·8	5·94	4·52
D	6A	A.iliaca communis	5·8	0·368	0·063	4·0	R_4	6·88	14·34	24·4
D	7A	A.iliaca externa	5·8	0·290	0·055	4·0	R_4	3·88	23	62·8
D	7B	A.iliaca externa	2·5	0·290	0·055	4·0	R_4	1·72	9·94	27
D	8A	A.profundus	6·3	0·255	0·052	16·0	L_4	0·78	32·4	114
D	8B	A.profundus femoris	6·3	0·186	0·046	16·0	L_4	0·35	60·9	402
D	9A	A.femoralis	6·1	0·270	0·053	4·0	R_4	3·48	28	87·6
D	9B	A.femoralis	6·1	0·259	0·052	4·0	R_4	3·30	30·4	104
D	9C	A.femoralis	6·1	0·249	0·051	4·0	R_4	2·82	33·2	123
D	9D	A.femoralis	6·1	0·238	0·050	4·0	R_4	2·24	36·2	146
D	9E	A.femoralis	7·1	0·225	0·049	4·0	R_4	2·62	46·6	210
D	10A	A.poplitea	6·3	0·213	0·048	8·0	R_4	1·02	46·2	232
D	10B	A.poplitea	6·3	0·202	0·047	8·0	L_4	0·884	51·8	292
D	10C	A.poplitea	6·3	0·190	0·046	8·0	L_4	0·764	58·6	373
D	11A	A.tibialis posterior	6·7	0·247	0·051	16·0	L_4	0·770	36·7	138
D	11B	A.tibialis posterior	6·7	0·219	0·049	16·0	L_4	0·578	46·7	223
D	11C	A.tibialis posterior	6·7	0·192	0·046	16·0	L_4	0·420	60·8	377
D	11D	A.tibialis posterior	6·7	0·165	0·044	16·0	L_4	0·282	82·3	691
D	11E	A.tibialis posterior	5·3	0·141	0·041	16·0	L_4	0·156	89·1	1020
D	12A	A.tibialis anterior	7·5	0·130	0·039	16·0	R_3	0·184	148	2010
D	12B	A.tibialis anterior	7·5	0·130	0·039	16·0	R_3	0·184	148	2010
D	12C	A.tibialis anterior	7·5	0·130	0·039	16·0	R_3	0·184	148	2010
D	12D	A.tibialis anterior	7·5	0·130	0·039	16·0	R_3	0·184	148	2010
D	12E	A.tibialis anterior	4·3	0·130	0·039	16·0	R_3	0·106	85	1160
	13A	A.anonyma	3·4	0·620	0·086	4·0	L_5	13·5	2·96	1·76
	14A	A.subclavia	3·4	0·423	0·067	4·0	R_4	5·60	6·35	8·11
D	14B	A.subclavia	6·8	0·403	0·066	4·0	R_4	10·0	14	19·7
D	15A	A.axillaris	6·1	0·364	0·062	4·0	R_4	7·04	15·4	26·6
D	15B	A.axillaris	5·6	0·314	0·057	4·0	R_4	4·60	19	44
D	16A	A.brachialis	6·3	0·282	0·055	4·0	L_4	3·96	26·5	76·1
D	16B	A.brachialis	6·3	0·266	0·053	4·0	L_4	3·46	29·8	96·1
D	16C	A.brachialis	6·3	0·250	0·052	4·0	L_4	2·92	33·7	123
D	16D	A.brachialis	4·6	0·236	0·050	4·0	L_4	1·89	27·6	113
D	17A	A.ulnaris	6·7	0·215	0·049	8·0	L_4	1·11	48·5	240
D	17B	A.ulnaris	6·7	0·203	0·047	8·0	L_4	0·966	54·3	301
D	17C	A.ulnaris	6·7	0·192	0·046	8·0	L_4	0·836	60·7	377
D	17D	A.ulnaris	3·7	0·183	0·045	8·0	L_4	0·408	36·9	252
D	18A	A.radialis	7·1	0·174	0·044	8·0	L_4	0·676	78·4	592
D	18B	A.radialis	7·1	0·162	0·043	8·0	L_4	0·586	90·4	788
D	18C	A.radialis	7·1	0·150	0·042	8·0	R_3	0·482	106	1070
D	18D	A.radialis	2·2	0·142	0·041	8·0	R_3	0·133	36·4	413
D	19A	A.interossea volaris	7·9	0·091	0·028	16·0	L_3	0·090	319	8800
	20A	A.coelica	1·0	0·390	0·064	4·0	R_4	1·36	2·20	3·30
	21A	A.gastrica sin.	7·1	0·180	0·045	4·0	L_4	1·51	73·2	517
	22A	A.lienalis	6·3	0·275	0·054	4·0	L_4	3·74	27·8	84·2
	23A	A.hepatica	6·6	0·220	0·049	4·0	L_4	2·30	45·6	216
D	24A	A.renalis	3·2	0·260	0·052	4·0	L_4	1·67	15·8	53·5
	25AA	A.mesenterica sup.	5·9	0·435	0·069	4·0	R_4	10·4	10·4	12·6
	25BA	A.mesenterica inf.	5·0	0·160	0·043	4·0	R_3	0·792	65·3	583
	26AA	A. carotis com. sin.	5·9	0·370	0·063	4·0	R_4	7·12	14·4	24
	26AB	A. carotis com. sin.	5·9	0·370	0·063	4·0	R_4	7·12	14·4	24
	26AC	A.carotis com.sin.	5·9	0·370	0·063	4·0	R_4	7·12	14·4	24
	26AD	A. carotis com. sin.	3·1	0·370	0·063	4·0	R_4	3·74	7·59	12·6
	26AE	A.car.int.sin.	5·9	0·177	0·045	8·0	L_4	0·600	62·9	459
	26AF	A.car.int.sin.	5·9	0·129	0·039	8·0	R_3	0·288	118	1630
	26AG	A.cerebri anterior sin.	5·9	0·083	0·026	16·0	L_3	0·055	286	9070
	26AH	A.car.ext.sin.	5·9	0·177	0·045	8·0	L_4	0·600	62·9	459
	26AI	A.car.ext.sin.	5·9	0·129	0·039	8·0	R_3	0·288	118	1630
	26AJ	A.car.ext.sin.	5·9	0·083	0·026	16·0	L_3	0·055	286	9070
	26BA	A.car.com.dextra	5·9	0·370	0·063	4·0	L_4	7·12	14·4	24
	26BB	A.car.com.dextra	5·9	0·370	0·063	4·0	L_4	7·12	14·4	24
	26BC	A.car.com.dextra	5·9	0·370	0·063	4·0	L_4	7·12	14·4	24
	26BD	A.car.ext.dextra	5·9	0·177	0·045	8·0	L_4	0·600	62·9	459
	26BE	A.car.ext.dextra	5·9	0·129	0·039	8·0	R_3	0·288	118	1630
	26BF	A.car.ext.dextra	5·9	0·083	0·026	16·0	L_3	0·055	286	9070
	26BG	A.car.int.dextra	5·9	0·177	0·045	8·0	L_4	0·600	62·9	459
	26BH	A.car.int.dextra	5·9	0·129	0·039	8·0	R_3	0·288	118	1630
	26BI	A.cerebri anterior dex.	5·9	0·083	0·026	16·0	L_3	0·055	286	9070
D	27A	A.vertebralis	7·1	0·188	0·046	8·0	L_4	0·836	67·1	434
D	27B	A.vertebralis	7·7	0·183	0·045	8·0	L_4	0·846	77	525

Table 2.4. Numerical data on segments of Figure 2.6.

We graphically place these points on a thickness - aortic length diagram and perform an exponential regression. These values apply to the patient case examined by Westerhof, i.e. for young, healthy adults.

In terms of wall thickness at older ages, Turkbey measured the thickness of the aortic wall at the pulmonary artery level, in a sample of patients (45-84 years old) and concluded that it remained constant and equal to h = 2.8mm, regardless of age and sex.

The PA level according to Westerhof corresponds to about 3 cm above the aortic valve where the thickness there is equal to,

$$h = 1.61 \ mm$$

So, considering that the exponential change of thickness in young people is maintained in older ages, we shift upwards the exponential curve that emerged, by the difference,

$$\Delta h = 2.8 - 1.61 = 1.19 \ mm$$

In this way we obtain the exponential function that governs the change in the thickness of the aortic wall in older ages and consequently in the age of 66.25 years old.

This function is:

$$h = 2.940517442 * e^{-0.001534059647*x} \qquad (19)$$

Now equation (19) can be transformed, which has a form of:

$$h = h_0 * e^{B_1*x}$$

into equation (20), which resembles the formula described by Fung:

$$h = h_0 * e^{\frac{B_h*x}{R_0}} \qquad (20)$$

where,

$$B_1 = \frac{B_h}{R_0} \rightarrow B_h = B_1 * R_0 \qquad 0.02 \leq B_h \leq 0.05$$

2.3 Design of the 3D models

2.3.1 Idealized model

The CAD software that was used to create the 3D models of the aorta was SOLIDWORKS 2018 by Dassault Systèmes. SOLIDWORKS is the world's most renowned software in the field of 3D mechanical design and it is used predominantly in the industrial section. Its user base ranges from individuals to large corporations, and covers a very wide cross-section of manufacturing market segments.

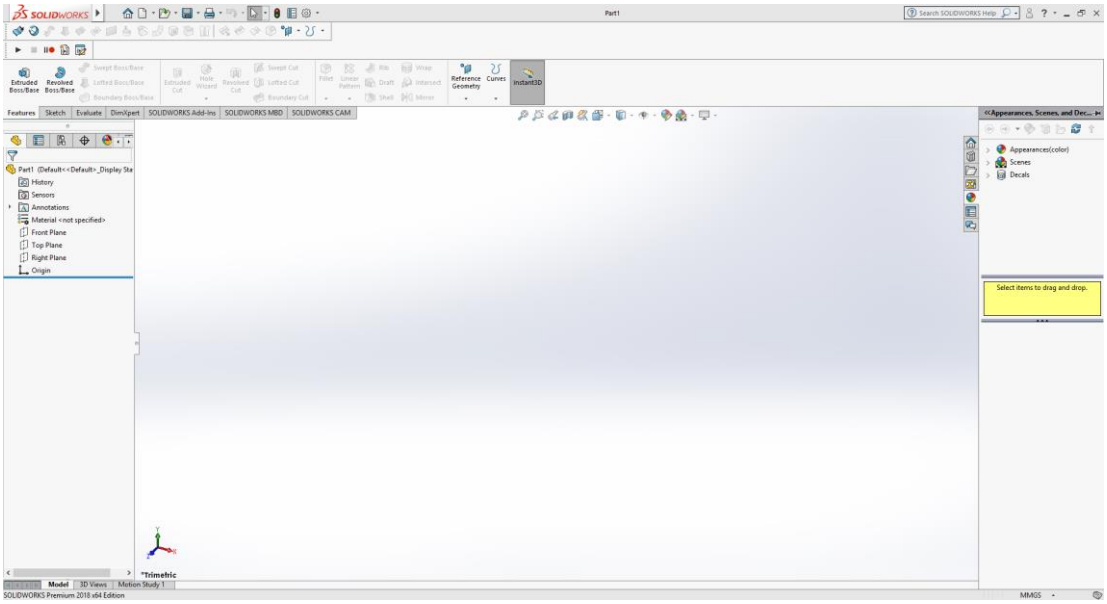

Figure 2.7. Solidworks 2018 user interface.

The first step in designing the aorta models was to insert the values of the parameters that were calculated in the previous chapter. These include, amongst others, the length of the various aortic segments, the luminal diameters and thickness of the wall (Figure 2.8).

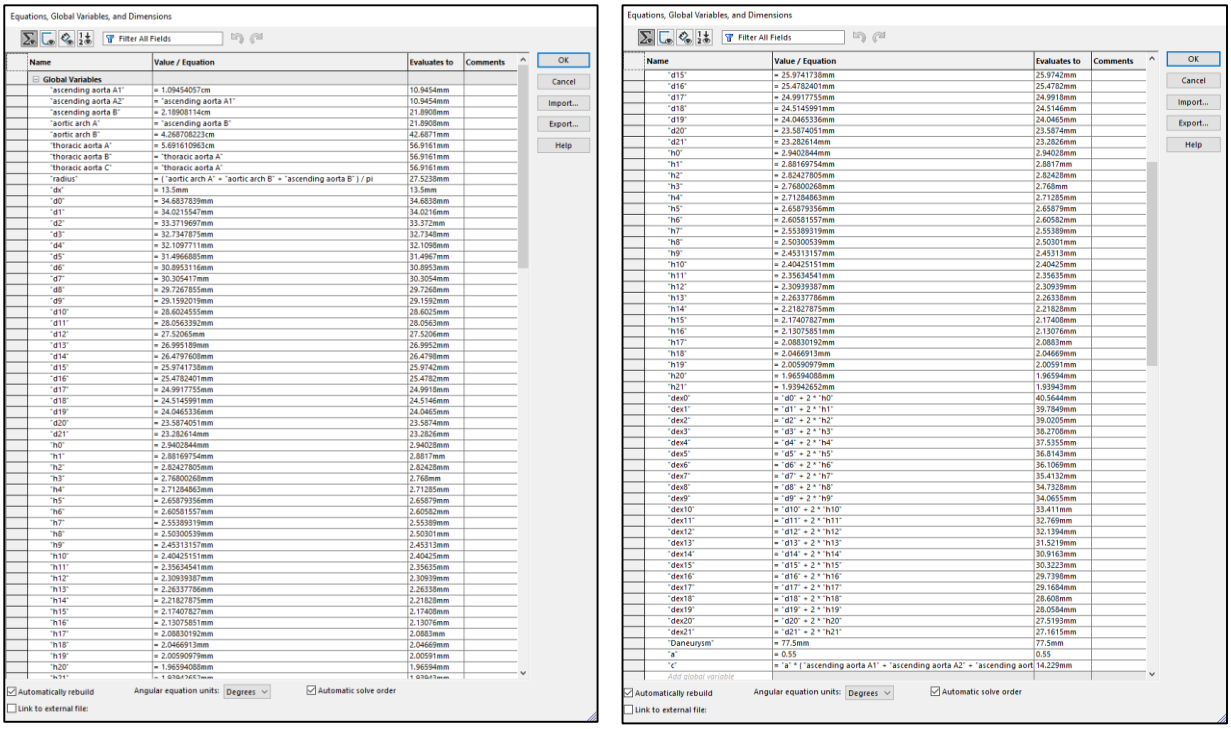

Figure 2.8. Inserting variables and dimensions into the program.

The next step was drawing the centerline of the aorta. As mentioned before, the segments, in which the aorta was divided into, were determined according to Westerhof's model of the human arterial system (Figure 2.6). In order to simplify the nature of the problem, the brachiocephalic artery, left common carotid and left subclavian were neglected during the model design. Thus, the centerline was a sum of the ascending aorta A, ascending aorta B, aortic arch A, aortic arch B, thoracic aorta A, thoracic aorta B and thoracic aorta C. The calculations for the length of these segments were described in Chapter 2.2 and their values differ among the different BSA classes. It should also be noted that the aortic arch A and B along with the last part of the ascending aorta (ascending aorta B) were assumed to form a circular arc of 180 degrees (Figure 2.9).

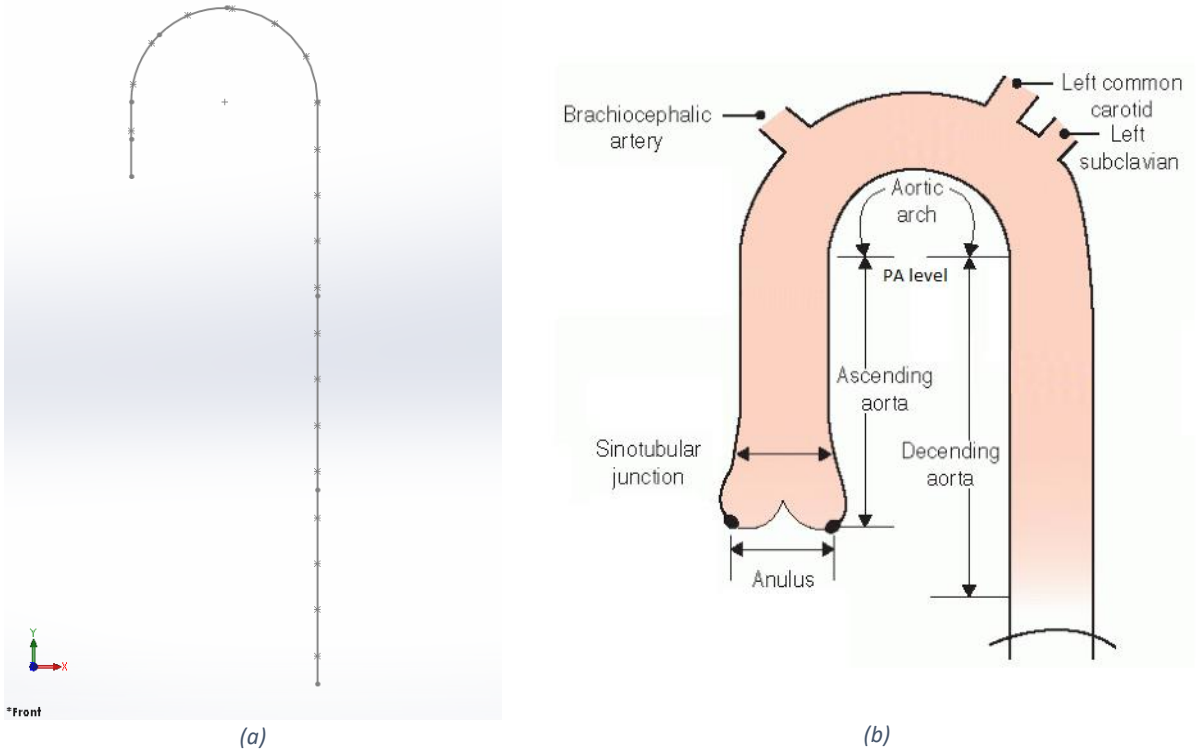

(a) (b)

Figure 2.9. (a). Centerline of the aortic model; brachiocephalic artery, left common carotid and left subclavian are not included in the design of the model. (b). Animation of thoracic aorta anatomy. PA : Pulmonary Artery [28]

Then, twenty equidistant points (first and last point not included) were placed along the centerline, each of which defined a different plane. The planes were positioned so that they were tangential to each point and perpendicular to the centerline and they were created for reference purposes. Particularly, they were used to draw circles with specific diameters on each one of them. These circles represented the thickness of the aortic vessel and at each point the diameter of the circular profiles was different so as to define the tapering of the aortic lumen and that of the wall's thickness as well.

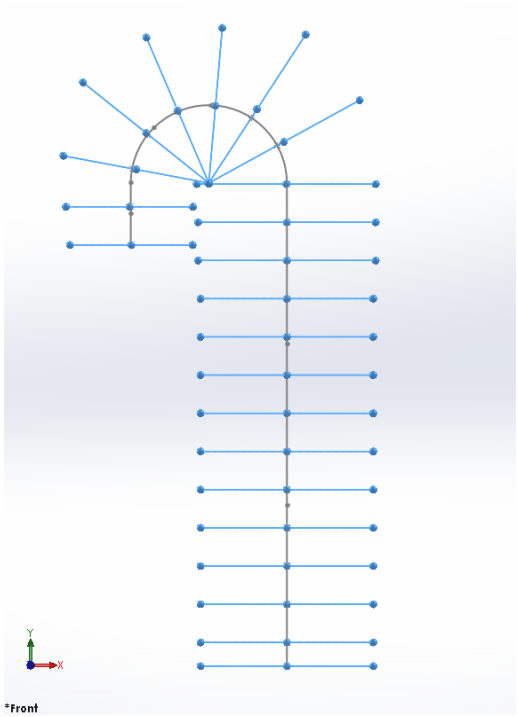

Figure 2.10. Planes positioned perpendicularly along the centerline.

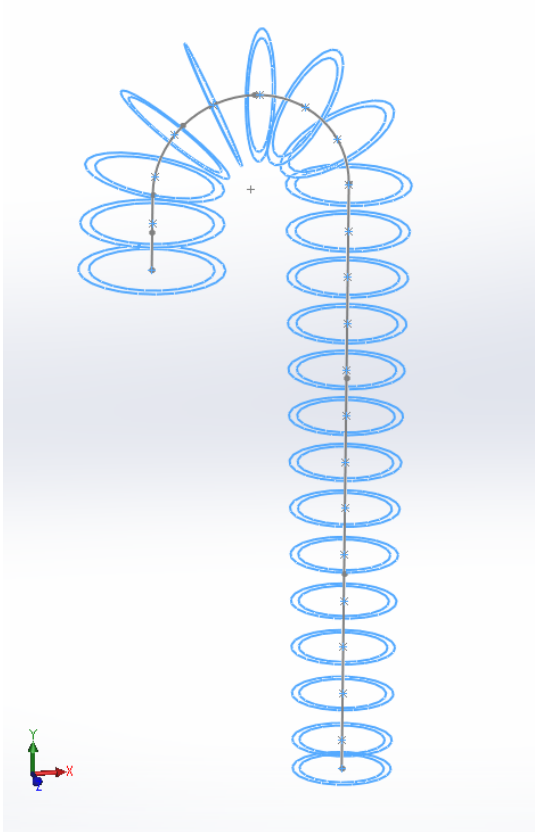

Figure 2.11. Sketched circles

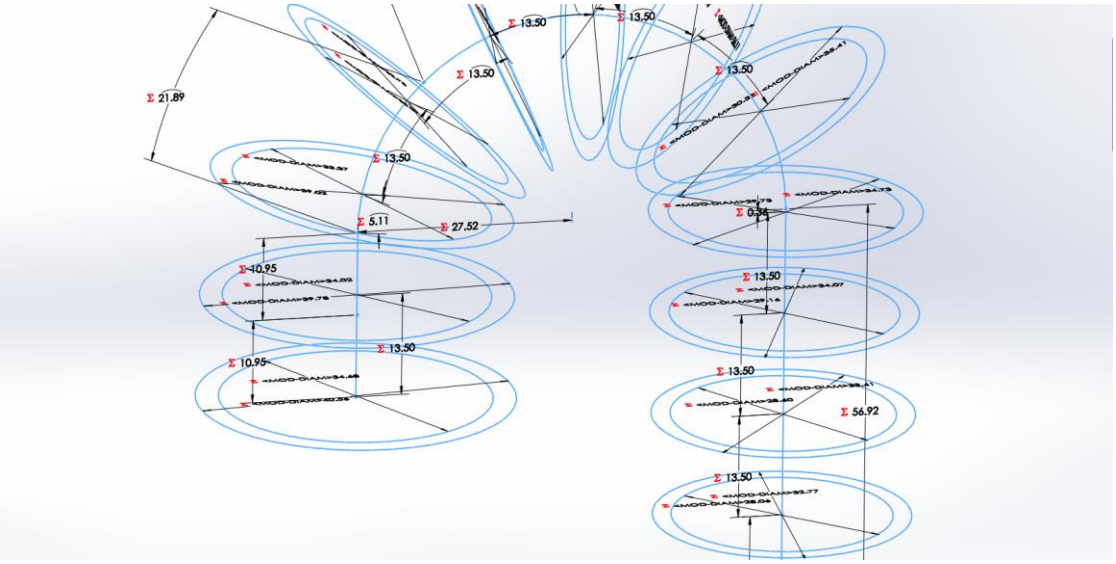

Figure 2.12. Close up view of the sketched circles and the applied dimensions.

In the subsequent stages, using the centerline and the aforementioned circles as guide curves, two lofts were created by applying the corresponding command, i.e. two solid bodies that were intersecting with each other (Figure 2.13).

After that, using the “Combine” and then “Subtract” option, the hollow vessel was created by simply subtracting the larger body from the smaller one (Figure 2.14).

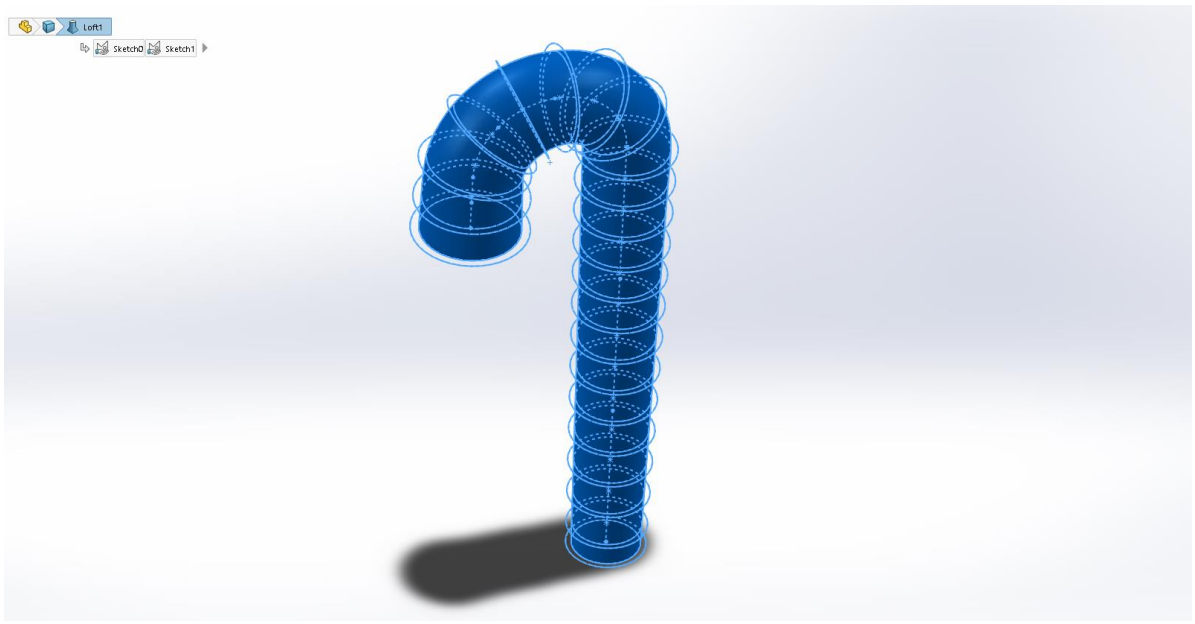

(a)

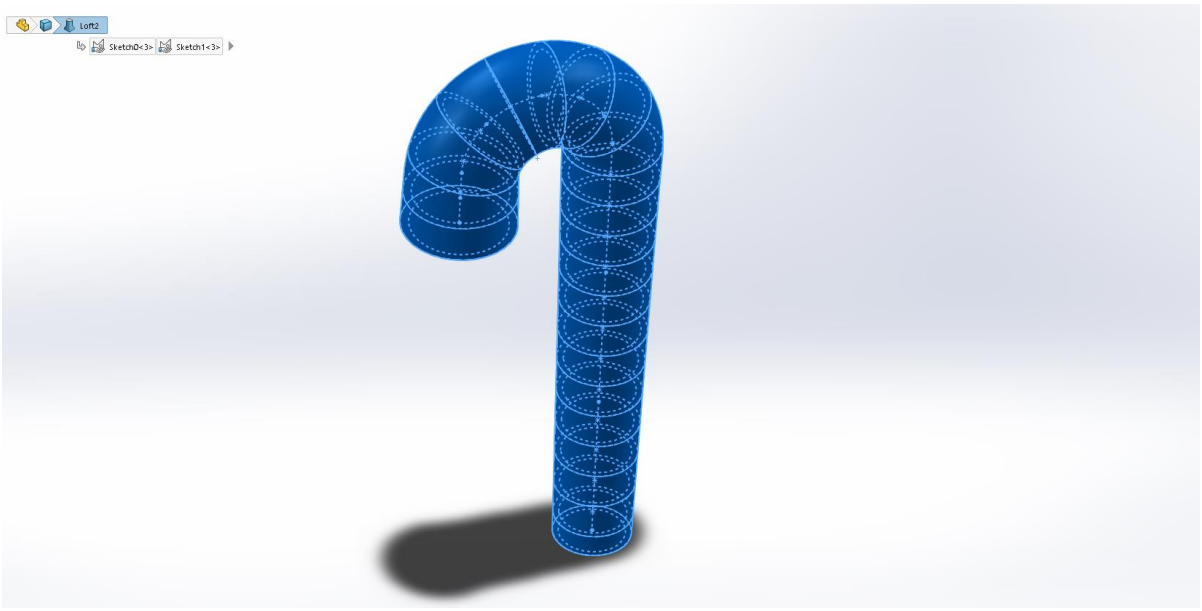

(b)

Figure 2.13. Creating the small (a) and large (b) solid by using the "Loft" command.

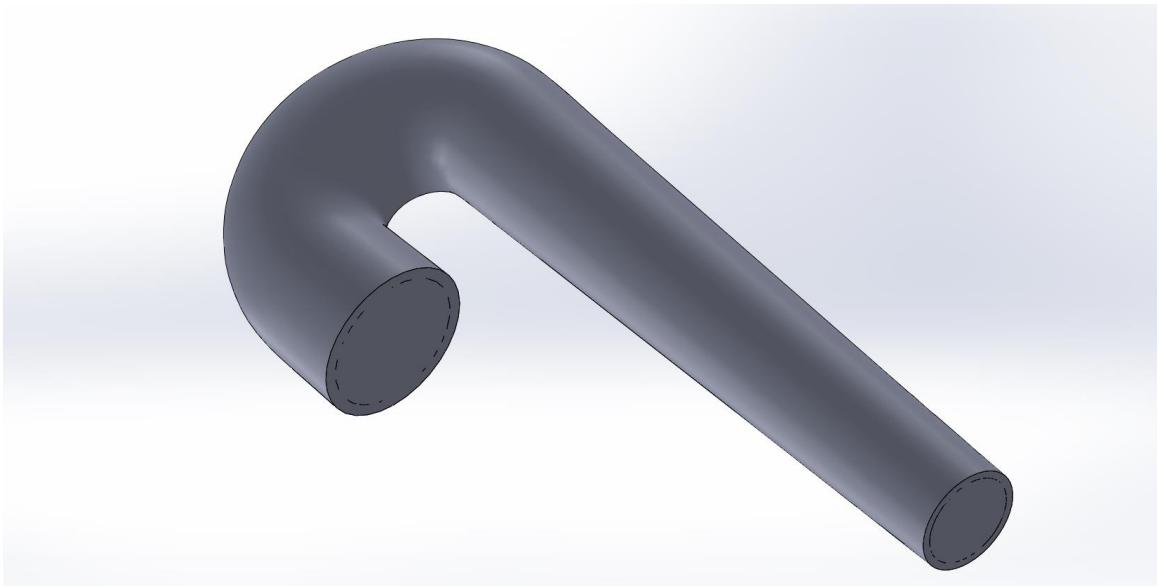

(a)

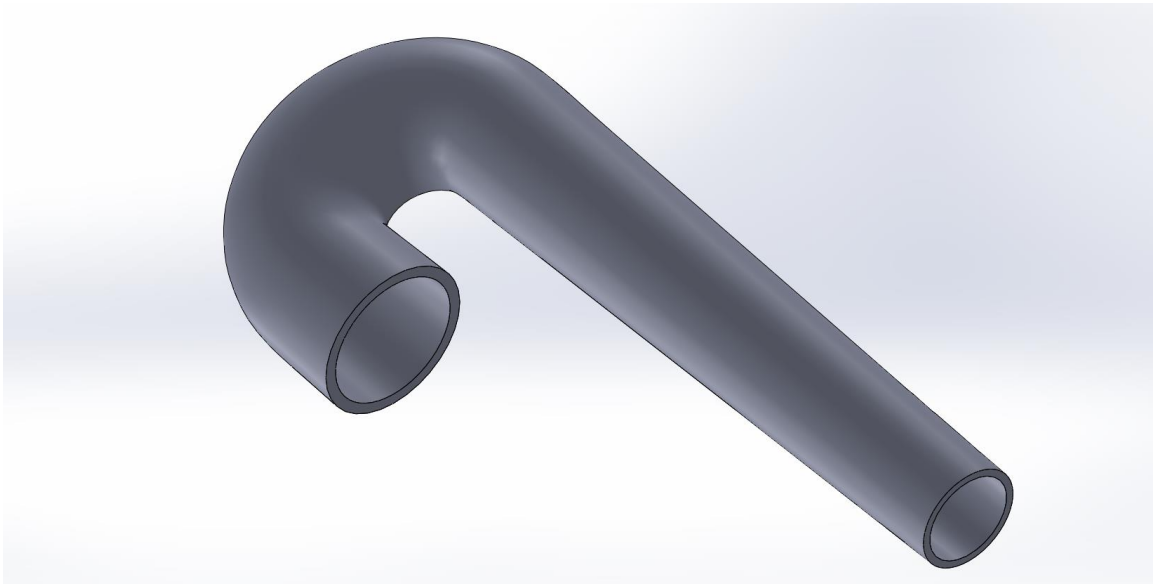

(b)

Figure 2.14. (a); both solid bodies created from the "Loft" command are merged into each other (b); the smaller body had been subtracted from the larger one creating this way the wanted cavity.

Once the model of the normal aorta was completed, the following step was to design the pathological state, i.e. design the fusiform, spherical aneurysm of the ascending aorta.

At first, a circle was sketched in the XY plane and using the revolve command a spherical solid was created. In order to maintain a logical similarity among the way in which the aneurysmatic models were designed for different BSA values, it was assumed that the center of this circle lied on a line that started from the curvature center of the aortic arch and passed through the midpoint of the centerline segment that

includes the ascending aorta and the aortic arch. Moreover, the sketch was made so that the midpoint would split the line into two uneven sections of which the outer one would amount to two thirds of the line's total length and the inner one to one third. The circle was centered on that line so that it passed through the outer end, as can be seen from Figure 2.15.

By changing the length of this line, we were able to design aneurysms with a wide range of diameters. In particular, as stated in the introduction, we examined different cases of maximal aortic diameter corresponding to an ASI of the moderate risk zone up until the severe risk zone, so ultimately, we designed models with diameters from 52.5 mm to 70 mm for body surface area equal to 1.65 m^2, 52.5 mm-75 mm for 1.85 m^2, 55 mm-77.5 mm for 2.0 m^2 and 55 mm-80 mm for 2.2 m^2.

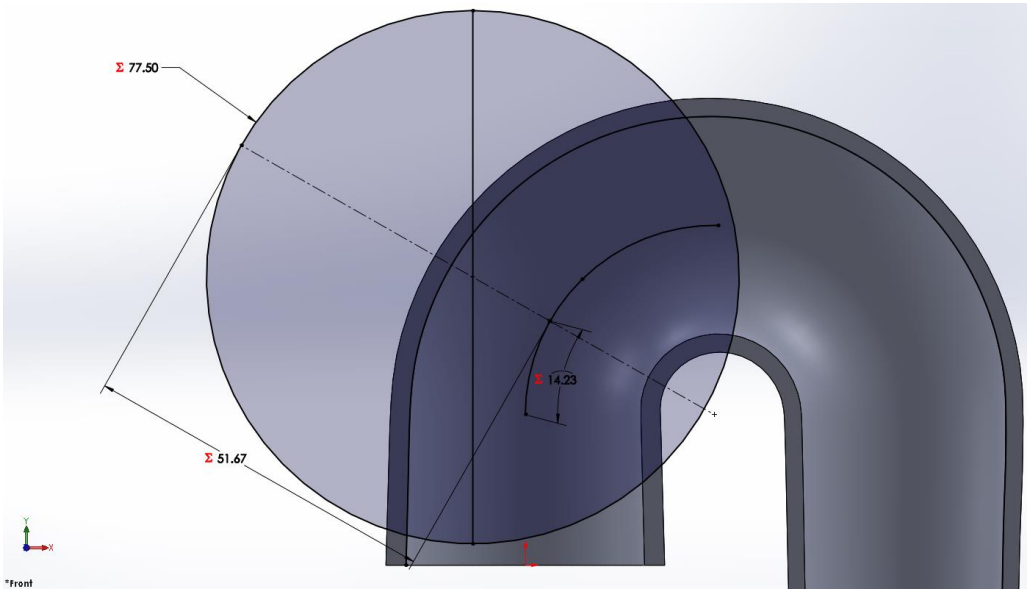

Figure 2.15. Section view of model; BSA=2.0 m^2, aneurysmal diameter= 77.5 mm, showing the 2D sketch of the spherical aneurysm.

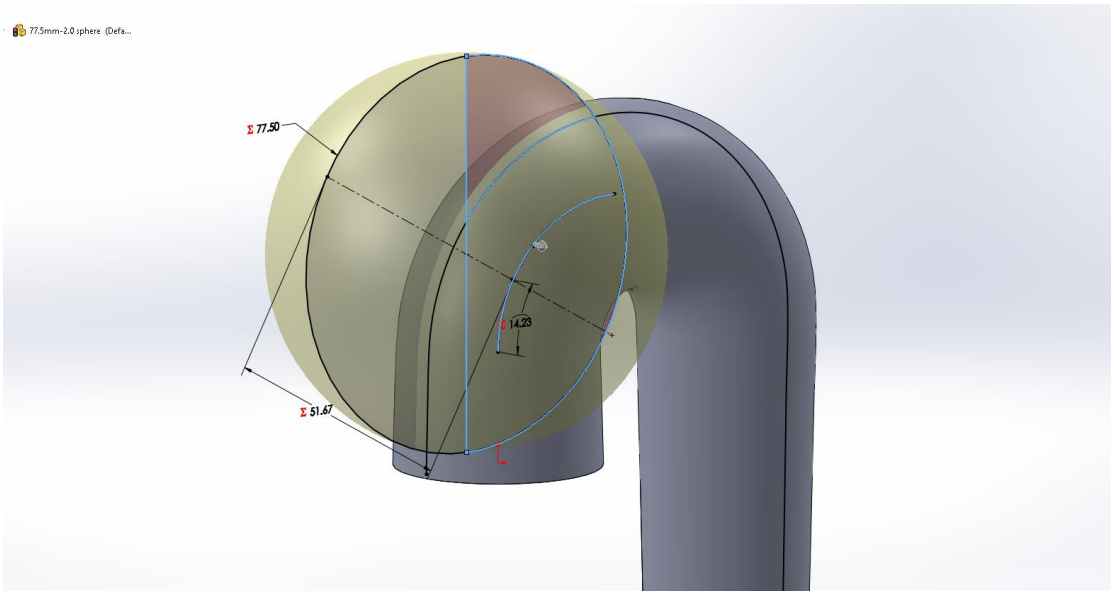

Figure 2.16. Preview of the revolution of the sketch.

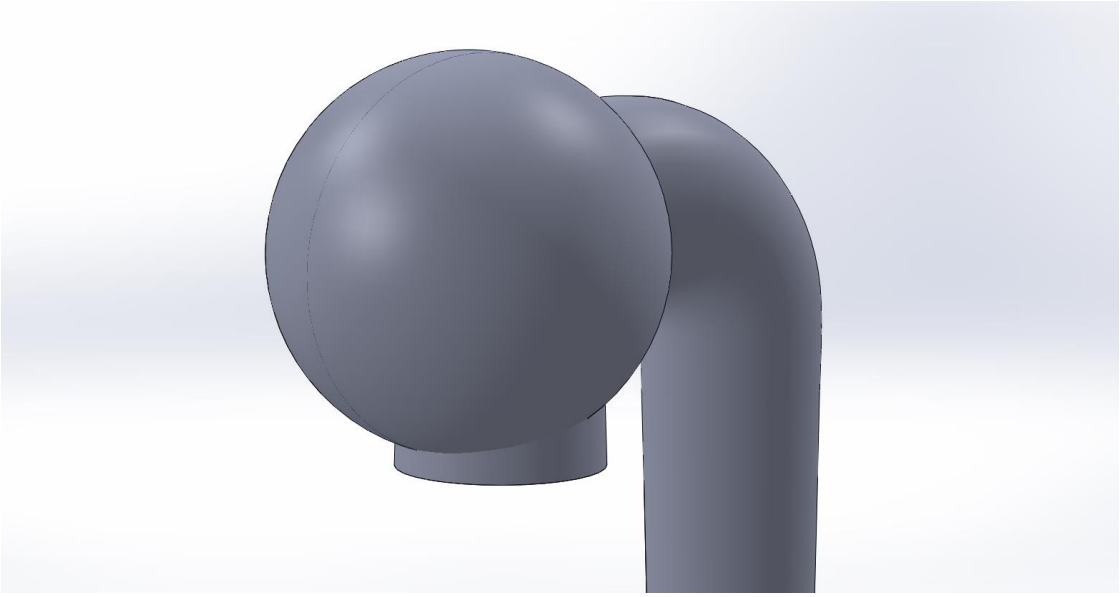

Figure 2.17. The created solid sphere as a result of the "Revolve" command.

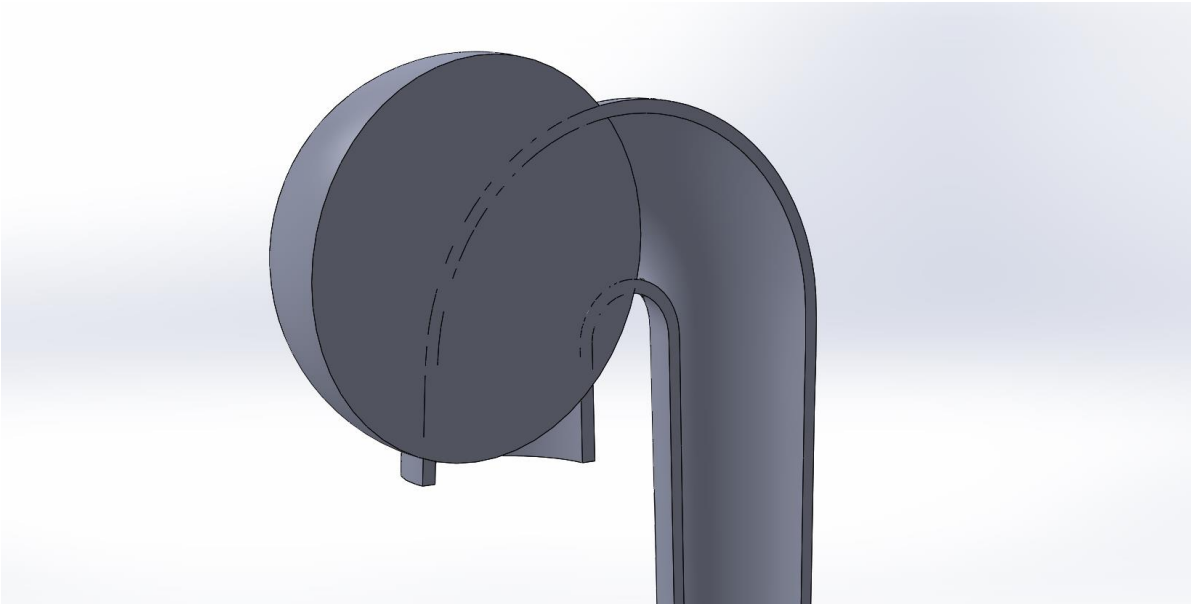

Figure 2.18. Section view of the model that shows the spherical solid intersecting with the normal geometry.

Having produced the spherical solid, we proceeded to hollow the part by choosing the “shell” command, creating this way an outward shell so that the dimension of 77.5 mm, as showed in Figure 2.16, represents the luminal diameter of the aneurysmal sphere. The thickness of the aneurysmatic shell was derived from a study carried out by Van Puyvelde and colleagues, in 2015 [29]. As can be seen from Figure 2.19, it was found that the thickness of the aortic wall for aneurysmal patients is on average equal to 1.526 mm or 1526 μm and the experimental measurements refer to a regression model that demonstrates the medial wall thickness in elective aortic root replacement incorporating the aortic diameter.

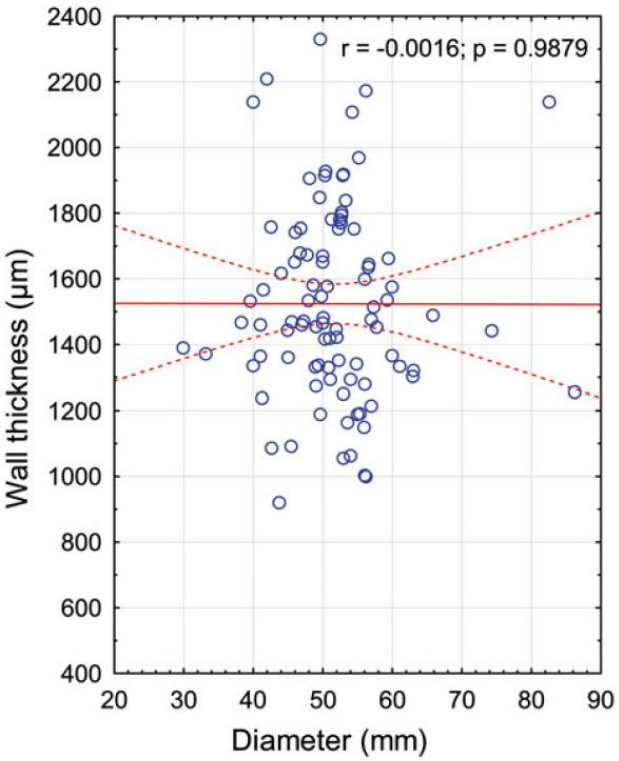

Figure 2.19. Scatterplot of wall thickness (µm) against aortic diameter (mm) [29]

Then, once the intersecting parts of the two hollow solids were removed, we placed fillets on all of the edges of the model.

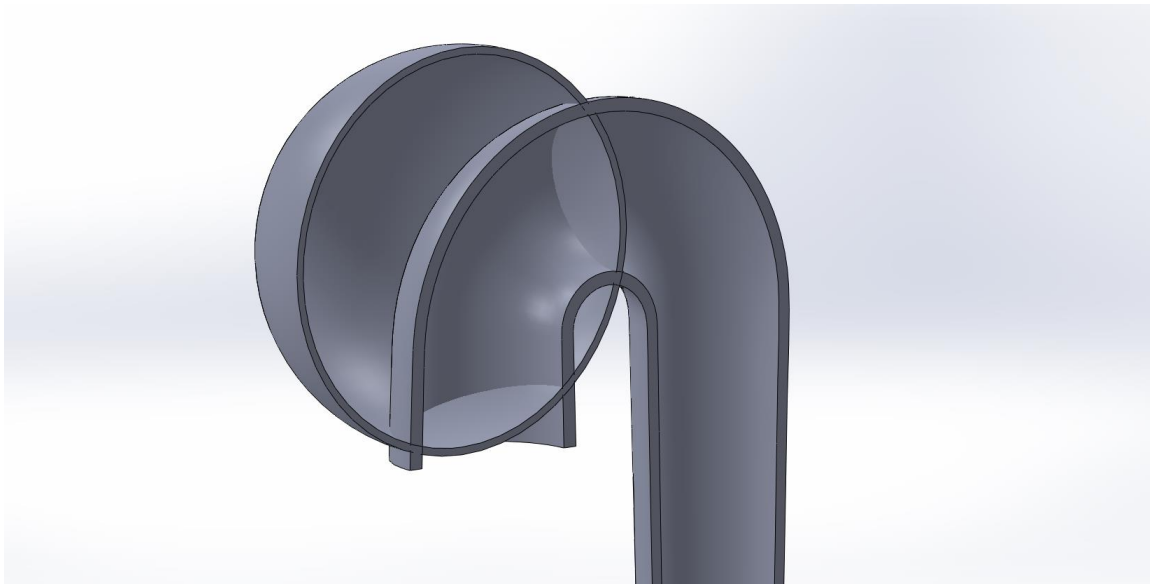

(a)

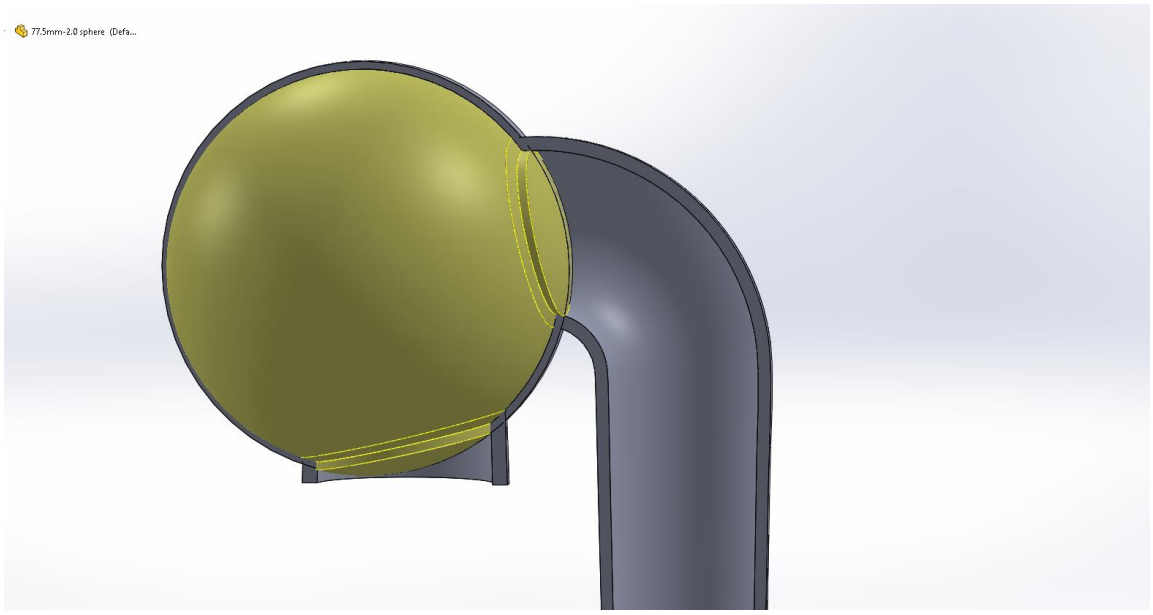

(b)

Figure 2.20. (a) The intersecting parts of the hollow sphere with the normal aortic model. (b) Preview of the "Intersect" command; after selecting the intersecting sections (highlighted areas), the command enables the removal of those parts and the merge of the remaining ones into one solid body.

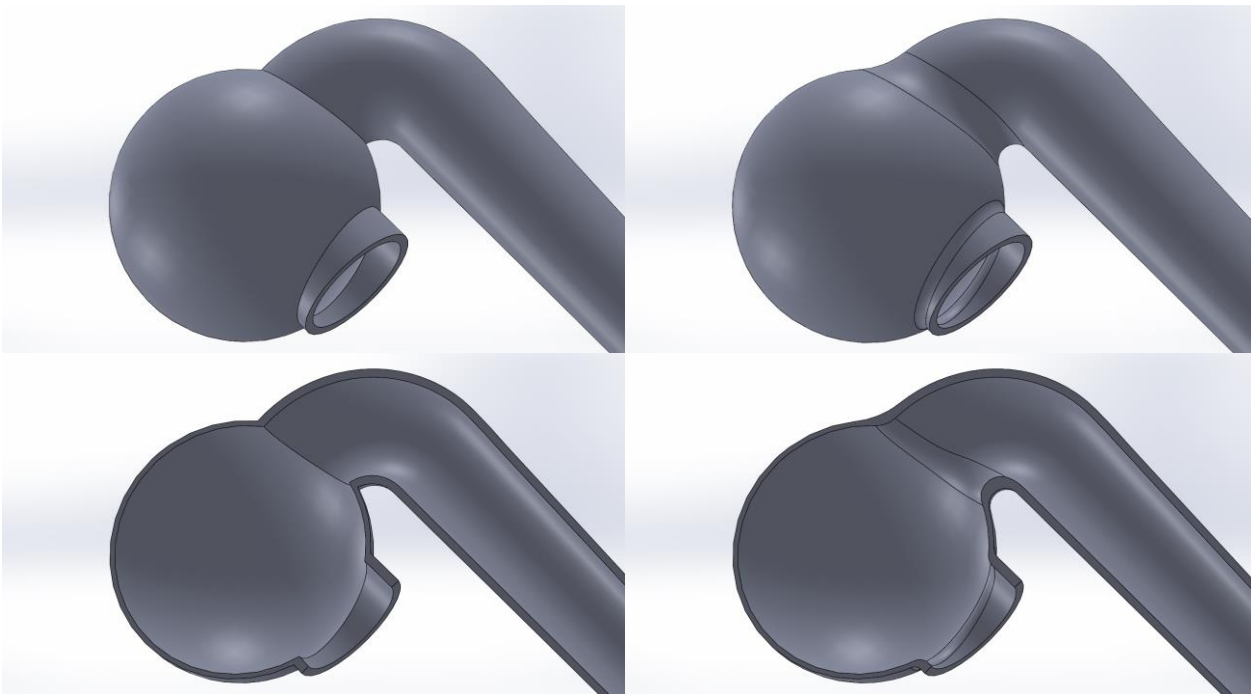

Figure 2.21. Creating fillets on sharp edges in order to achieve a more realistic result; the primary stage (before fillet) is depicted on the left set of pictures. The pictures in the bottom show a section view of the pictures in the top of the figure.

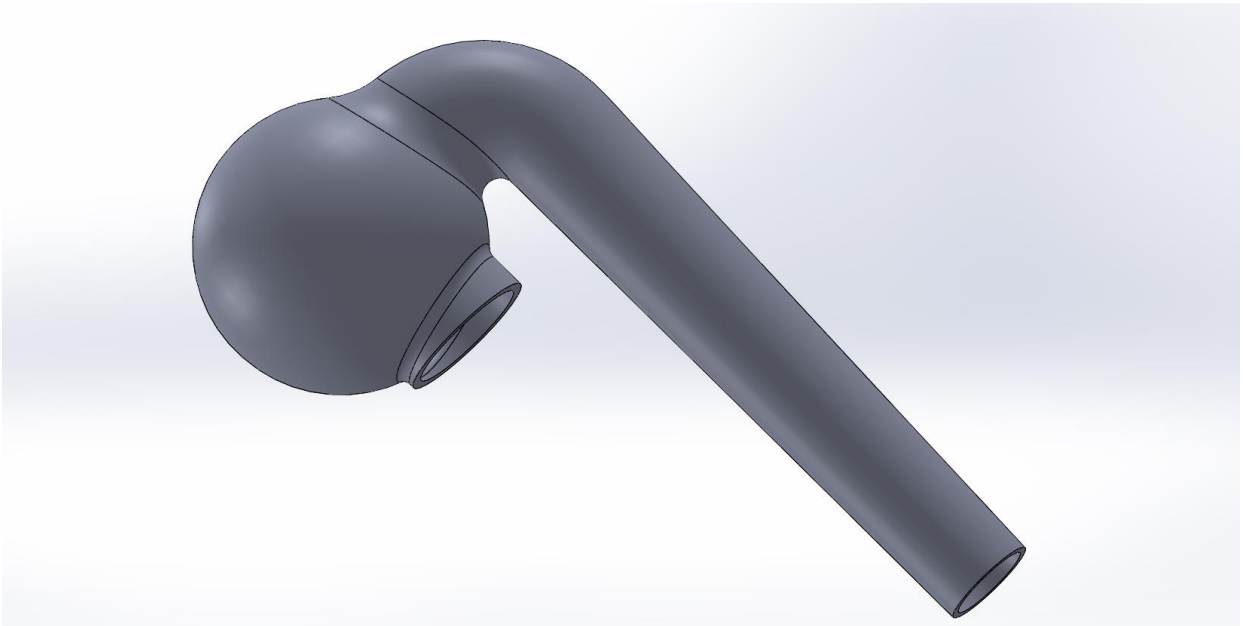

Figure 2.22. Final form of the idealized pathological aortic model.

2.3.2 Patient-specific model

The patient-based analysis relies on the non-contrast gated computed tomography (CT) scan of a patient, who suffered from ascending thoracic aortic aneurysm (aTAA) and underwent aortic repair surgery at "Ippokrateio" General Hospital of Athens in 2013. The CT data was made available for further processing, with informed patient consent, by the Attending Physician - cardiac surgeon at the Cardiac Surgery Department of "Ippokrateio" General Hospital of Athens. Basic clinical data, such as the weight (85 Kg) and height (1.74 m), was also obtained to calculate the body surface area (BSA=2.0 m^2) of the patient, by using the DuBois formula.

CT imaging protocol. The CT scan was performed on a 16-slice multidetector computed tomography (MDCT) scanner (Activion 16, Model TSX-031A, Toshiba). A protocol of 1 mm slice thickness was used with 120 kV, 60 mA tube current, 330 mm field of view for reconstruction and a sharp reconstruction kernel. The CT was performed in the craniocaudal direction, from the base of the skull to the level of the renal arteries, in a single breath-hold (Figure 2.24).

Figure 2.23.Toshiba's Activion 16 Multislice CT system.

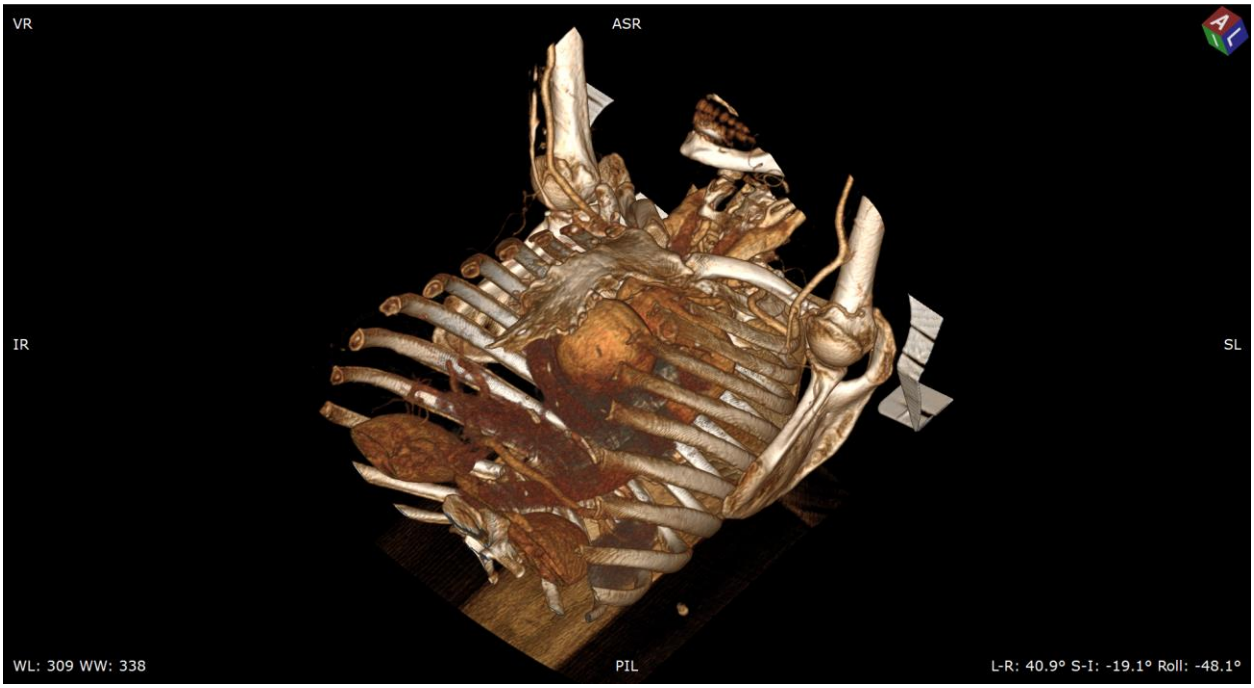

Figure 2.24. 3D view of the CT scan

The Mimics software (Materialise Inc.) was used for their processing of the CT series consisting of 328 DICOM files.

Mimics is an advanced medical technology toolbox which enables the processing and three-dimensional reconstruction of computed tomography (CT) and magnetic resonance imaging (MRI) scans. Researchers and engineers use the certified toolkits of Mimics software to develop state-of-the-art medical device designs, individual implants, and life-saving surgical instruments.

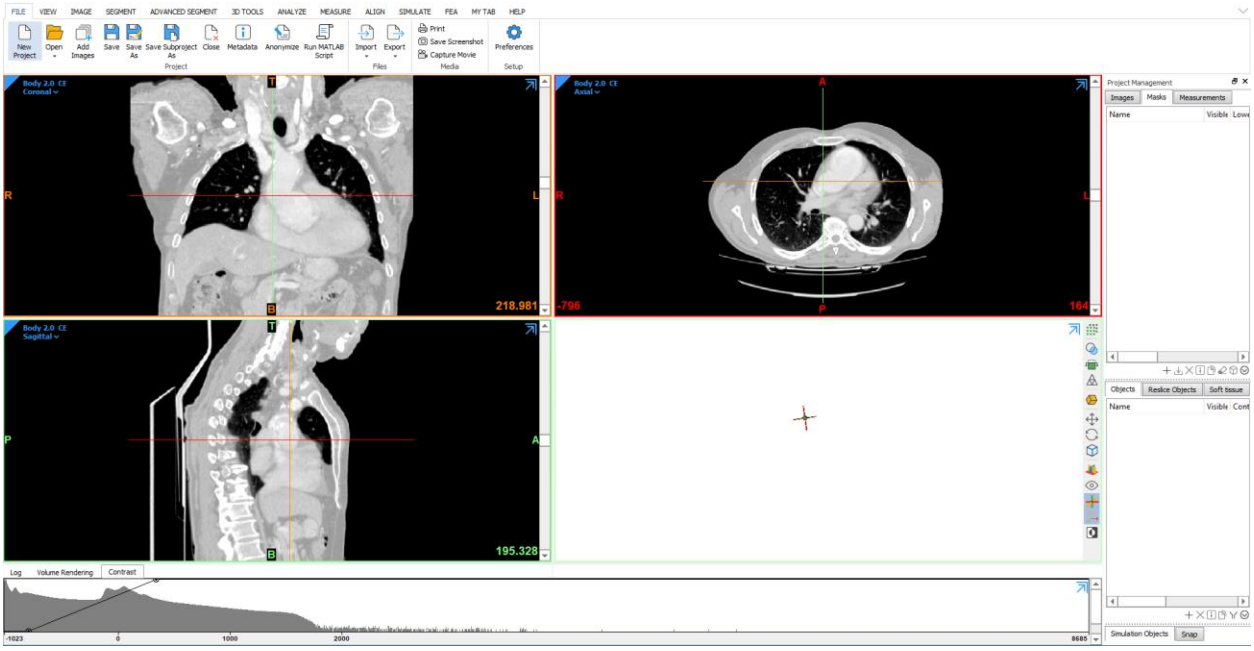

Figure 2.25. Mimics user interface.

Mimics enables the examination of CT scans in four views: 1) the coronal view in the upper left area of Figure 2.25, 2) the sagittal view at the bottom left, 3) the axial view at the upper right area, and 4) the 3D view at the bottom right area of Figure 2.25, where the reconstructed anatomic part of interest is accessible. The four views are interrelated, adapting to the selected intersection and the crosshair pinpoint.

The aorta was initially isolated from the surrounding bones and organs using the automated “Dynamic region growing” process in Mimics that is based on their gray value connectivity. The aorta was further restricted to the desired bounds (the aortic arch upwards and the aortic bifurcation downwards) by batch-removing the out-of-bounds segmented cross-sections. The segmentation of the aorta was further optimized, with a special focus on the aortic wall calcifications (not included in the final reconstruction), via a slice-by-slice manual process, removing also any leftover segmented artifacts.

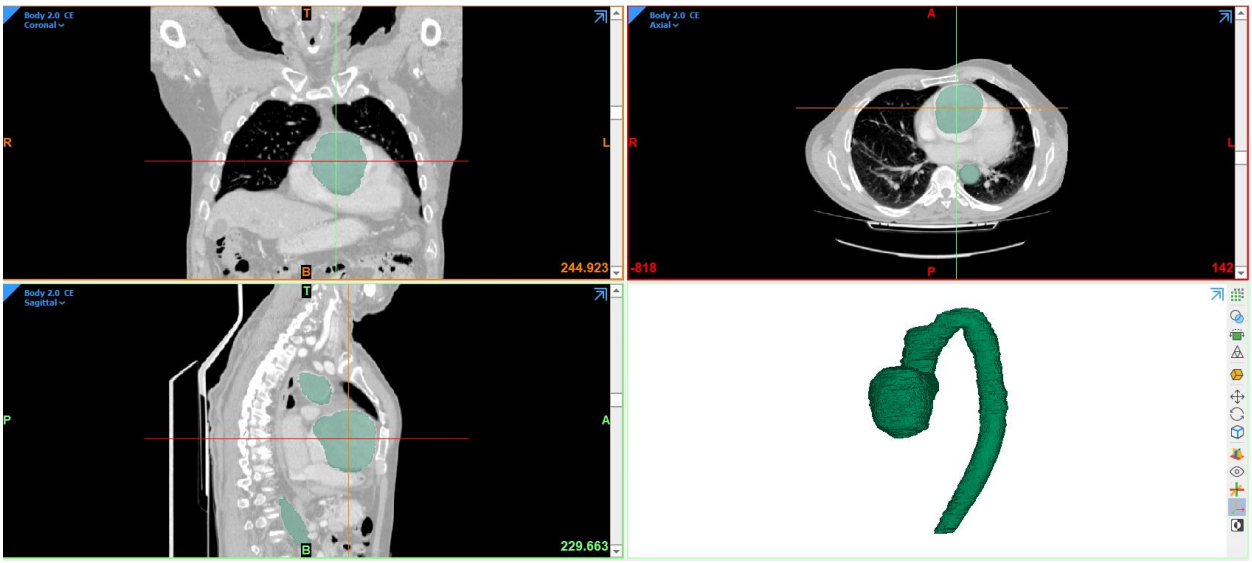

Figure 2.26. The aTAA model in different views after isolating the aortic lumen.

The initial reconstructed thoracic aorta model features rough artificial edges on its surface that would hamper the upcoming structural simulations if left unrefined. To this end, the model was further processed by applying smoothing operations both at the 2D (cross-sections) and the 3D levels.

Smoothing is an iterative process for the reduction of the surface roughness, provided that the least deviation from the original data is ensured. During the smoothing process, it was observed that the cross-sectional area (and the volume of the aorta in extend) depended on the number of smoothing iterations and the smooth factor. More iterations lead to a more natural result, while the smooth factor had a heavy impact on the shape of the aorta. Conclusively, it was decided to perform several iterations (500) and keep the smooth factor to a minimum value (0.1). It is also worth noting that during the segmentation process, we applied a small expansion of the segmentation mask to compensate for the volume shrinkage due to the smoothing, ending up with a volume-preserving model of the thoracic aorta (with respect to the original data).

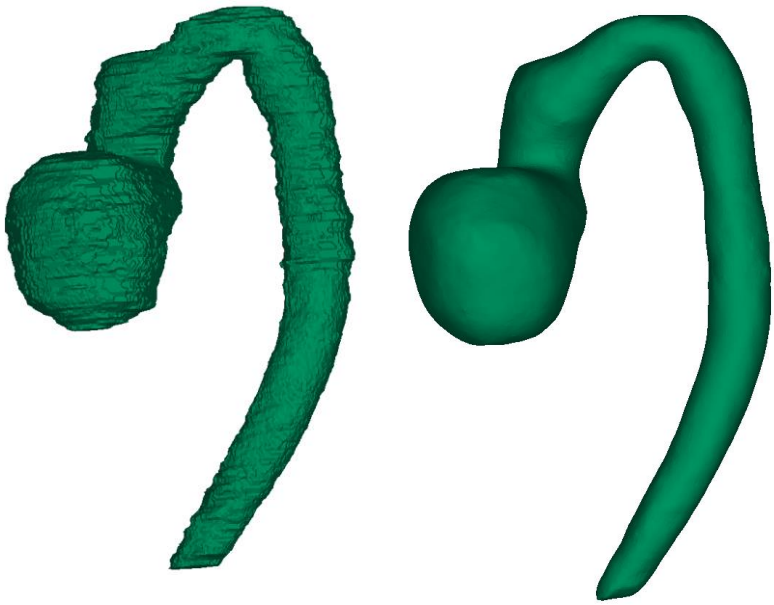

Figure 2.27. 3D aTAA model before (a) and after (b) smoothing.

To identify the aortic valve, the left ventricle of the heart was also segmented and reconstructed. Specifically, a hole, representing the aortic valve without its cusps, was opened on the aortic surface by removing the intersected area between the left ventricle and the aorta surfaces using the Visualization Toolkit (VTK) library. The final patient-based aTAA model is depicted in Figure 2.28 (b).

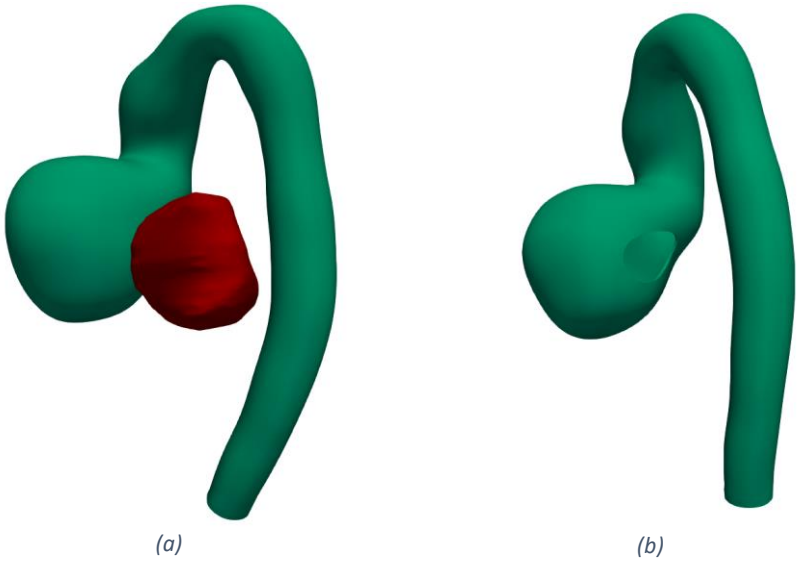

Figure 2.28. (a) Superposition of the aTAA and left ventricle surfaces and (b) resulting aTAA model after intersection featuring the aortic valve opening.

Mesh generation. After completing the segmentation, reconstruction, smoothing and surface preprocessing (described in the previous paragraphs), the aTAA model is represented by an open surface without thickness, in STL format. Towards performing the structural simulations, a solid model with a given wall thickness and the corresponding computational mesh needed to be generated. In this direction, a multi-step workflow involving several open-source software and Python libraries, was put in place. The aTAA model (STL file) was initially imported into the free Autodesk Meshmixer software (Autodesk Inc.) where the surface was extruded outwards in the normal direction with an offset of 1.526mm corresponding to the wall thickness of a typical aTAA, as mentioned before [29]. The extruded surface, also in STL format, was subsequently imported into the SimVascular software for the generation of the computational mesh. SimVascular is a fully open source software package that provides a complete pipeline from medical image data segmentation to patient specific blood flow simulation and analysis [30]. Another advantage of SimVascular is that it successfully extracts the parts of the model exterior where boundary conditions are applied, specifically, the surfaces representing the inner and the outer wall and the rings taking shape upon extrusion at the inlet (aortic valve) and the outlet (descending aorta). The aTAA model is subsequently discretized into tetrahedral elements also using SimVascular and the computational grid is exported by default in VTU format (unstructured grid format used by VTK). Finally, the VTU mesh is converted to INP format using the meshio Python library. This file format is operational in the FEBio software which was chosen as the Finite Element Analysis package for the conduct of the simulations.

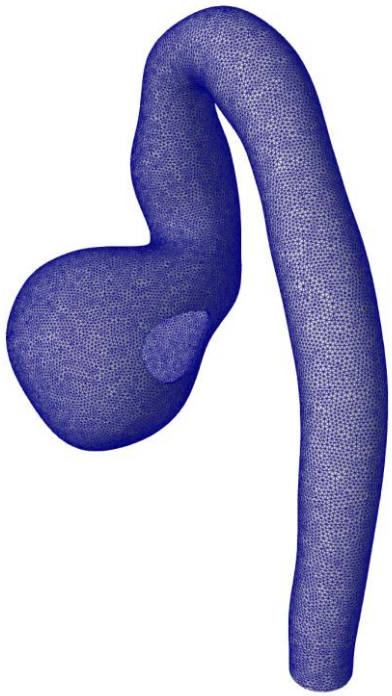

Figure 2.29. Final result of the meshed aneurysmatic aortic model.

2.4 Materials and Methods

2.4.1 Idealized geometry case preparation

The simulations of the idealized aortic models were carried out in ANSYS[3] R19.0. Ansys develops and markets engineering simulation software for use across the product life cycle. Ansys Mechanical finite element analysis software is used to simulate computer models of structures, electronics, or machine components for analyzing strength, toughness, elasticity, temperature distribution, electromagnetism, fluid flow, and other attributes. Ansys is used to determine how a product will function with different specifications, without building test products or conducting crash tests. For example, Ansys software may simulate how a bridge will hold up after years of traffic, how to best process salmon in a cannery to reduce waste, or how to design a slide that uses less material without sacrificing safety.

Most Ansys simulations are performed using the Ansys Workbench system, which is one of the company's main products. Typically, Ansys users break down larger structures into small components that are each modeled and tested individually. A user may start by defining the dimensions of an object, and then adding weight, pressure, temperature and other physical properties. Finally, the Ansys software simulates and analyzes movement, fatigue, fractures, fluid flow, temperature distribution, electromagnetic efficiency and other effects over time.

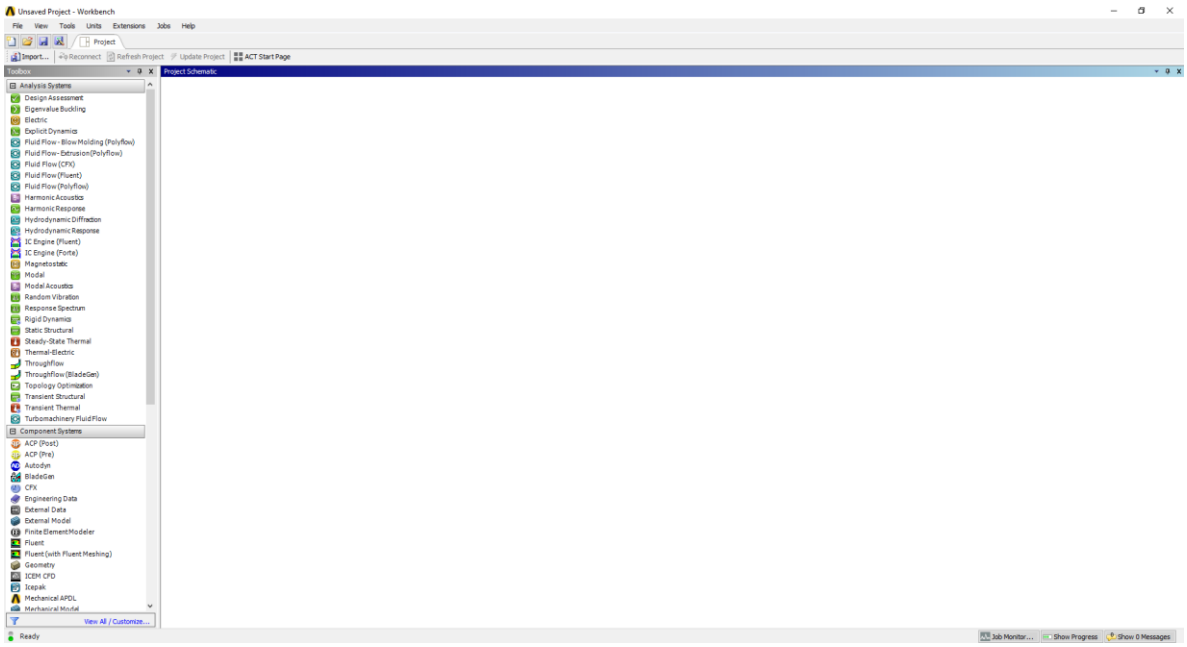

Figure 2.30. ANSYS Workbench R19.0 User Interface.

It was found from literature that it is reasonable to model the arterial wall as a linear elastic isotropic material, i.e. Hooke law was applied:

$$\sigma = E * \varepsilon$$

[3] *Ansys® Academic Research Mechanical, Release 19.0*

According to scientific articles that are referenced below, biological tissues are often defined by a Poisson coefficient that ranges between 0.45 and 0.49 (approaching 0.5 for nearly incompressible material) [31-39]. After test simulations it was calculated that applying a Poisson's ratio of 0.49 yields higher stresses and thus it is the worst-case scenario (Figure 2.31). It was this conclusion that lead to finally choosing 0.49 as the optimal value for this study.

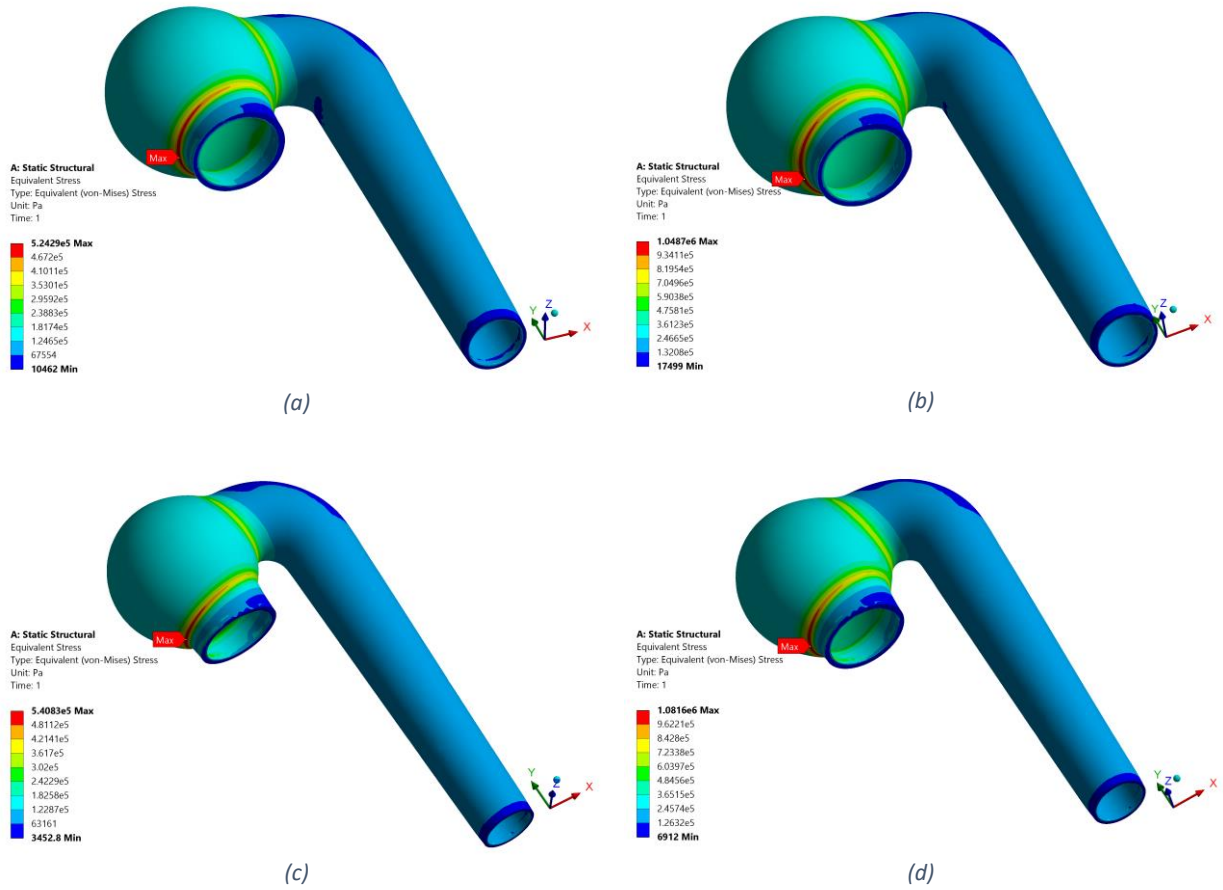

Figure 2.31. (a) and (b) represent a Poisson coefficient of v=0.45 while (c) and (d) were computed for v=0.49. The models on the left are loaded with 120 mmHg and the ones on the right with 240 mmHg. All models refer to a BSA of 2.0 m^2 and an aneurysmal diameter equal to 65 mm.

Additionally, an elastic modulus needed to be specified. For this, we relied on the findings of Koullias [40] and Khanafer [41]. What Koullias and colleagues deduced was that the incremental elastic modulus (E_{inc}) rises as aortic diameter increases. In particular, E_{inc} mean values in aortic aneurysms were significantly higher than in normal aortas. Within ascending aortic subgroups of different sizes that were examined during the study, aneurysms less than 4 cm in diameter had significantly lower E_{inc} values than those with diameter higher than 5 cm, implying that larger ascending aortic aneurysms have already been stretched to near their limits. E_{inc} increased progressively with each rise in aneurysm diameter (Figure 2.32).

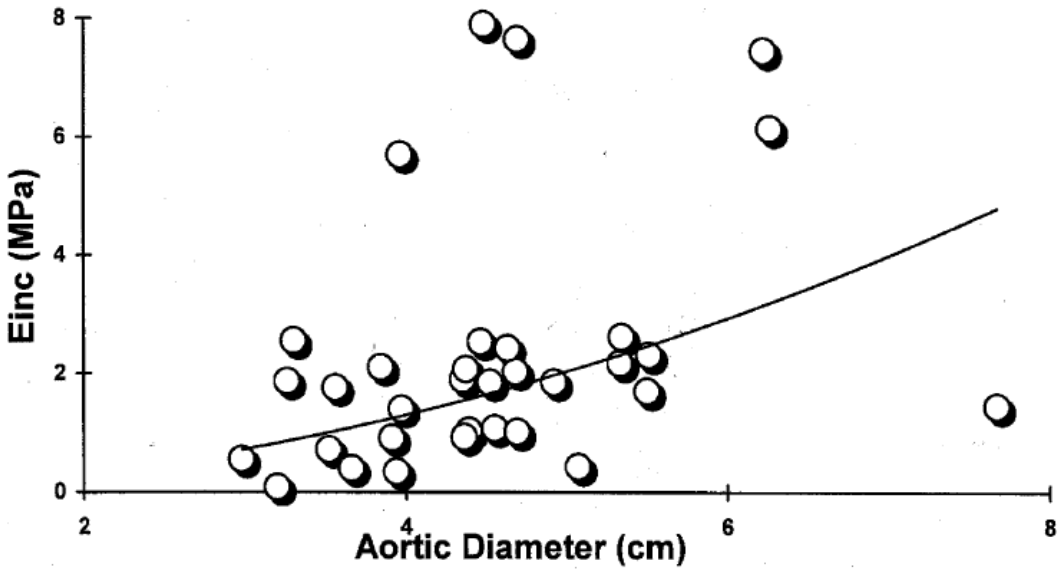

Figure 2.32. Relationship between E_{inc} and aortic diameter in ascending aortic aneurysms.[40]

However, the conclusions above were drawn exclusively for the normal pressure of 120 mm Hg. Using the study done by Khanafer, we were able to reduce the elastic modulus-diameter relationship for the hypertensive case of 240 mm Hg. More specifically, by calculating the difference between the physiological and hypertensive moduli of Khanafer's specimen we managed to calculate the corresponding difference for Koullias' study and hence construct the expression which describes the interaction between the modulus and the aneurysmal diameter for the pressure of 240 mm Hg.

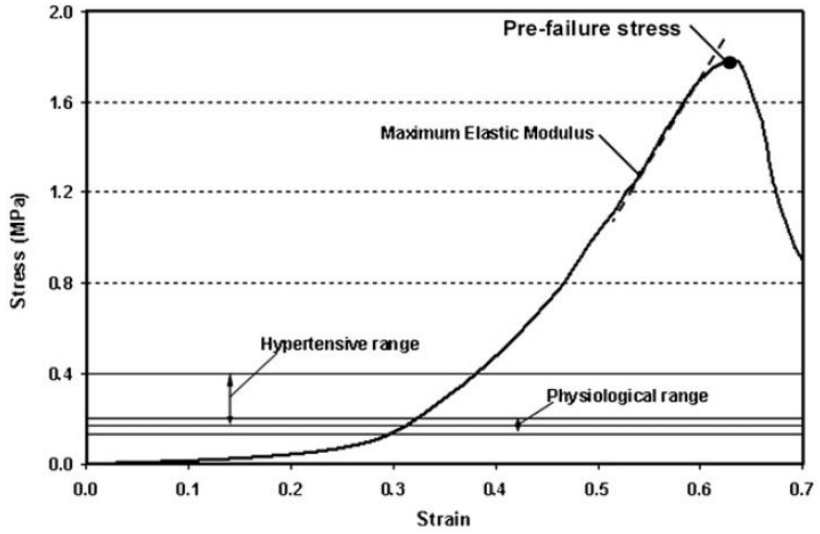

Figure 2.33. Principles of calculating the physiologic range, hypertensive range, and Maximum Elastic Modulus (MEM).[41]

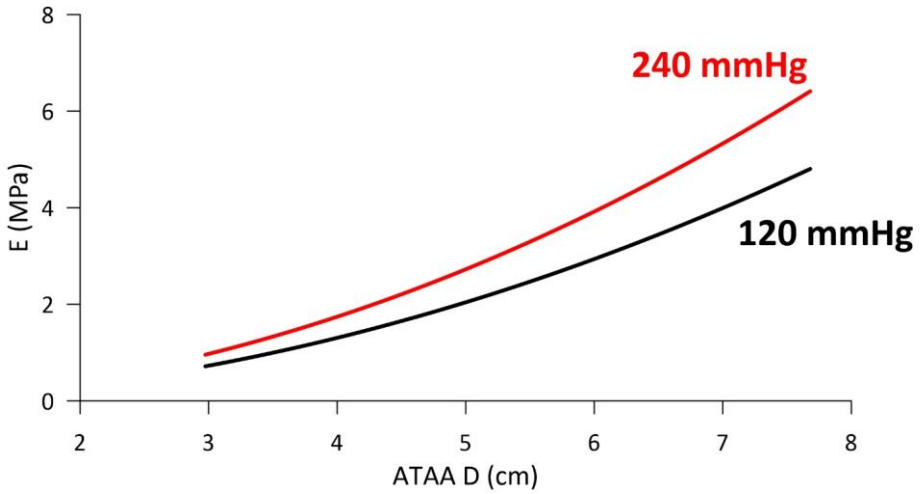

Figure 2.34. Relationship between the diameter of the ascending thoracic aortic aneurysm ATAA D (cm) and the elastic modulus E (MPa) for the pressures of 120 mmHg (red curve) and 240 mmHg (black curve)

All freedom of motion was fixed for the nodes in the proximal aortic root and the aortic bifurcation (Figure 2.36). The aortic lumen was then loaded with a uniform pressure of 120 mm Hg (physiological) and 240 mm Hg (hypertensive), perpendicular to its inner surface in both cases (Figure 2.35). The results extracted were deformation, strain and stress with the Von Mises stresses having been computed in pascals (Pa).

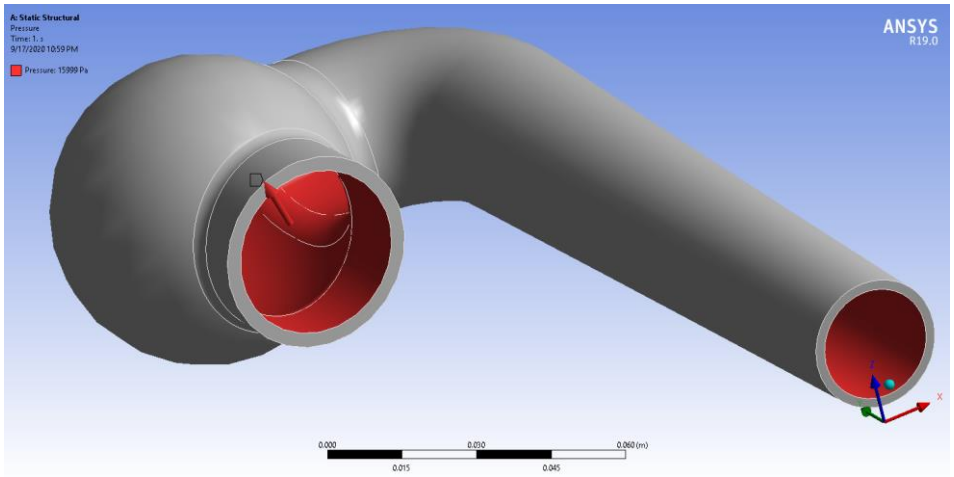

Figure 2.35. Setting a uniform and normal to the internal surface pressure. (120 mmHg = 15999 Pa)

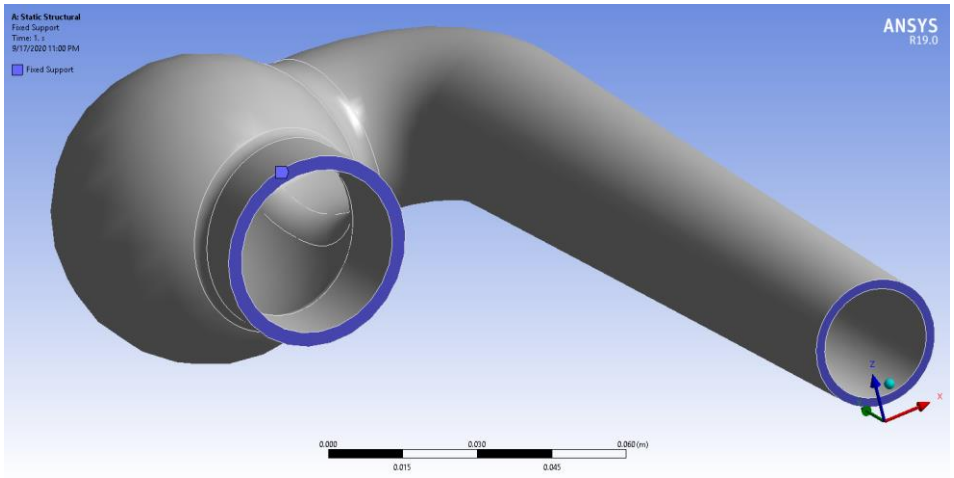

Figure 2.36. Inserting boundary conditions in ANSYS.

According to ANSYS User's Guide[4] the equivalent stress, strain and deformation are computed as such:

Equivalent stress is related to the principal stresses by the equation:

$$\sigma_e = \left[\frac{(\sigma_1 - \sigma_2)^2 + (\sigma_2 - \sigma_3)^2 + (\sigma_3 - \sigma_1)^2}{2}\right]^{\frac{1}{2}}$$

Equivalent stress (also called *von Mises stress*) is often used in design work because it allows any arbitrary three-dimensional stress state to be represented as a single positive stress value. Equivalent stress is part of the maximum equivalent stress failure theory used to predict yielding in a ductile material.

The von Mises or **equivalent strain ε_e** is computed as:

$$\varepsilon_e = \frac{1}{1+v}\left(\frac{1}{2}[(\varepsilon_1 - \varepsilon_2)^2 + (\varepsilon_2 - \varepsilon_3)^2 + (\varepsilon_3 - \varepsilon_1)^2]\right)^{\frac{1}{2}}$$

v = effective Poisson's ratio, which is defined as follows:

- Material Poisson's ratio for elastic and thermal strains computed at the reference temperature of the body.
- 0.5 for plastic strains.

Deformation

Physical deformations can be calculated on and inside a part or an assembly. Fixed supports prevent deformation; locations without a fixed support usually experience deformation relative to the original location. Deformations are calculated relative to the part or assembly world coordinate system.

[4] *Ansys® Academic Research Mechanical, Release 19.0, Mechanical User's Guide, ANSYS, Inc.*

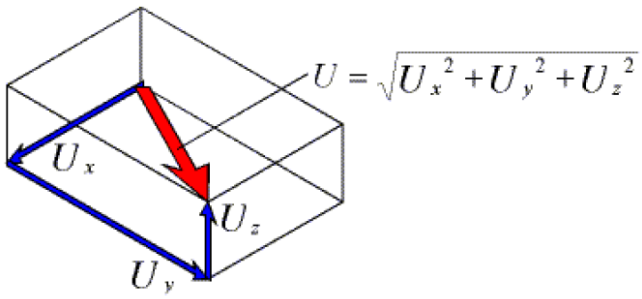

- Component deformations (**Directional Deformation**)
- Deformed shape (**Total Deformation** vector)

The three component deformations U_x, U_y, and U_z, and the deformed shape U are available as individual results.

Adaptive Convergence (Adaptive Mesh Refinement)

In ANSYS Workbench 19.0, the user has the ability to control the relative accuracy of a solution in two ways. They can use the meshing tools to refine the mesh before solving, or they can use convergence tools as part of the solution process - by inserting a Convergence object under each result- to refine solution results on a particular area of the model.

When using the latter method, the application can fully automate the solution process, while the user can control the convergence by specifying a level of accuracy for the selected results. The specified accuracy is achieved by means of adaptive and iterative analysis, whereby h-adaptive methodology is employed. The h-adaptive method begins with an initial finite element model that is refined over various iterations by replacing coarse elements with finer elements in selected regions of the model. This is effectively a selective remeshing procedure. The criterion for which elements are selected for adaptive refinement depends on geometry and on what ANSYS Workbench product results quantities are requested. The result quantity $\boldsymbol{\phi}$**,** the expected accuracy **E** (expressed as a percentage), and the region **R** on the geometry that is being subjected to adaptive analysis may be selected. The user-specified accuracy is achieved when convergence is satisfied as follows:

$$100\left(\frac{\varphi_{i+1} - \varphi_i}{\varphi_i}\right) < E\,, \qquad i = 1,2,3,\dots,n\ (in\ R)$$

where **i** denotes the iteration number. It should be clear that results are compared from iteration **i** to iteration **i+1**. Iteration in this context includes a full analysis in which h-adaptive meshing and solving are performed.
For the needs of this thesis, an accuracy of *E=0.5%* was prescribed as a convergence criterion.

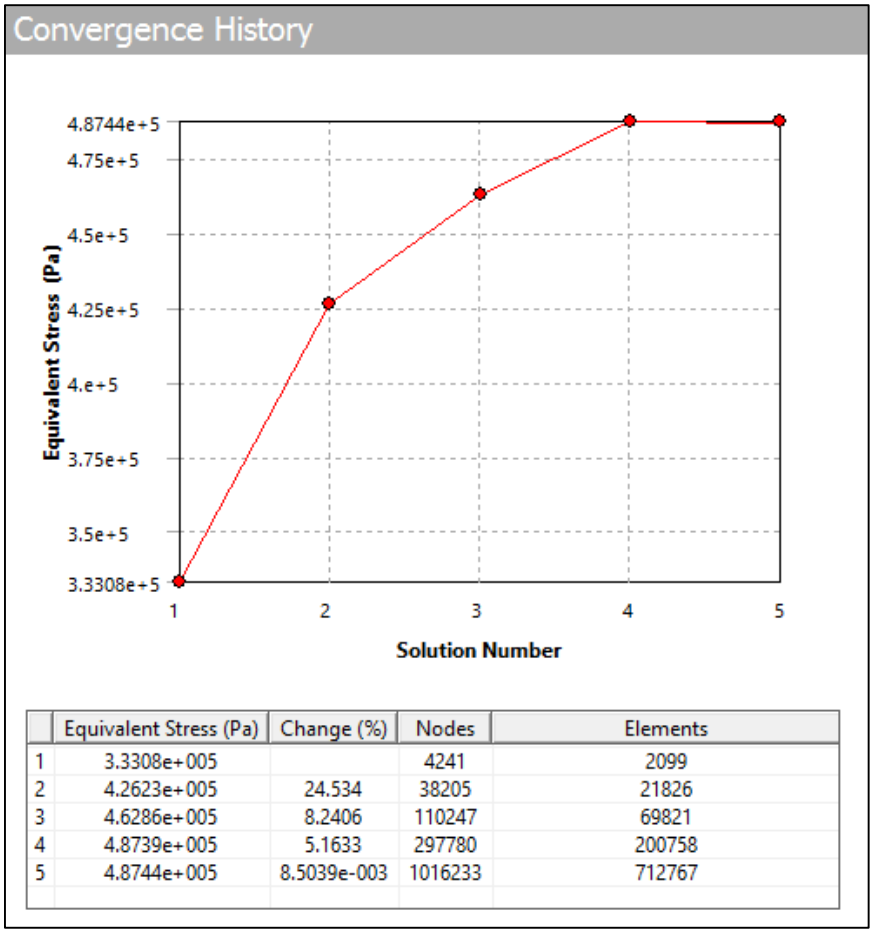

	Equivalent Stress (Pa)	Change (%)	Nodes	Elements
1	3.3308e+005		4241	2099
2	4.2623e+005	24.534	38205	21826
3	4.6286e+005	8.2406	110247	69821
4	4.8739e+005	5.1633	297780	200758
5	4.8744e+005	8.5039e-003	1016233	712767

Figure 2.37. The window that appears during the solution process in ANSYS and shows the convergence progress by presenting graphically the calculated value of the selected result (here: maximum stress) for every solution. The table below the chart presents the error (change (%)) as well as the density of the mesh in every iteration. It is clear that the criterion of 0.5% has been fulfilled in this simulation.

2.4.2 Patient-specific case preparation

For the simulation of the real-life geometry that was reconstructed from the CT scan data, the FEBio Studio software was used. FEBio is a nonlinear finite element solver that is specifically designed for biomechanical applications. It offers modeling scenarios, constitutive models and boundary conditions that are relevant to numerous research areas in biomechanics. Development, distribution and support is a joint effort between Jeff Weiss's lab at the University of Utah and Gerard Ateshian's lab at Columbia University.[42]

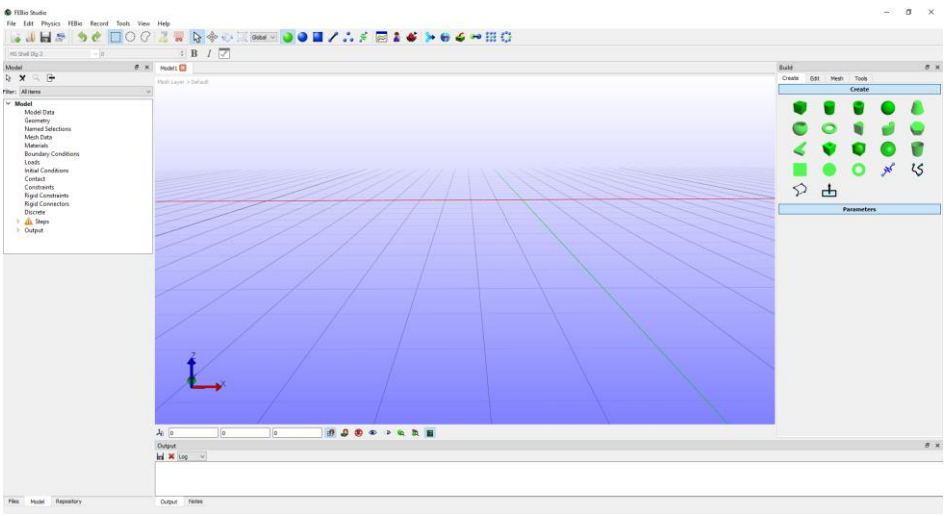

Figure 2.38. FEBio Studio user interface.

The exact same procedure, as in subchapter 2.4.1 Idealized geometry case preparation, was followed in order to set up the patient model for simulation, i.e. fixing all freedom of motion at the two ends of the model and selecting the aortic lumen to carry out the stress study with a normal and a hypertensive pressure value.

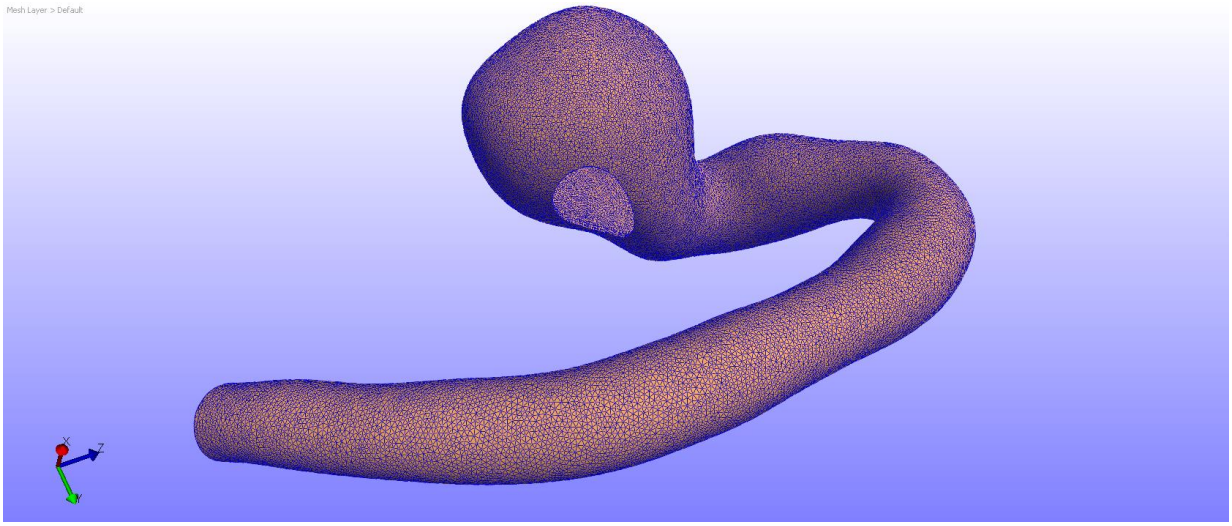

Figure 2.39. Mesh of the model.

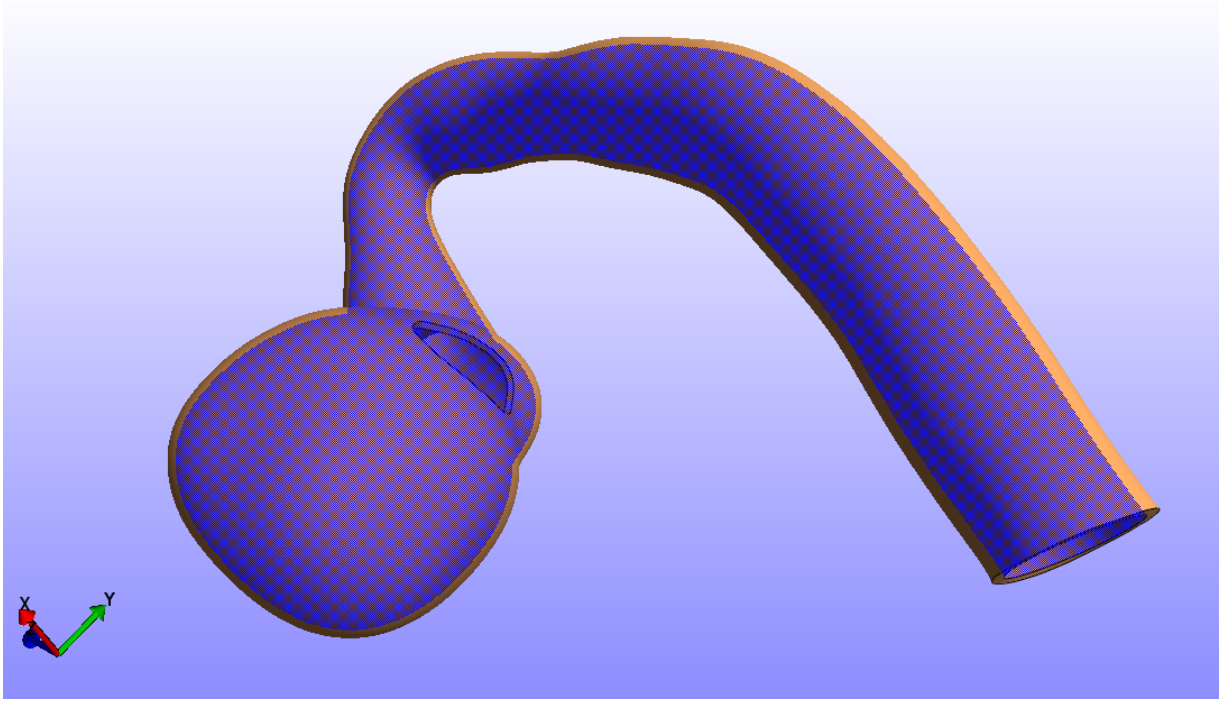

Figure 2.40. Selection of the internal surface in order to apply a uniform pressure.

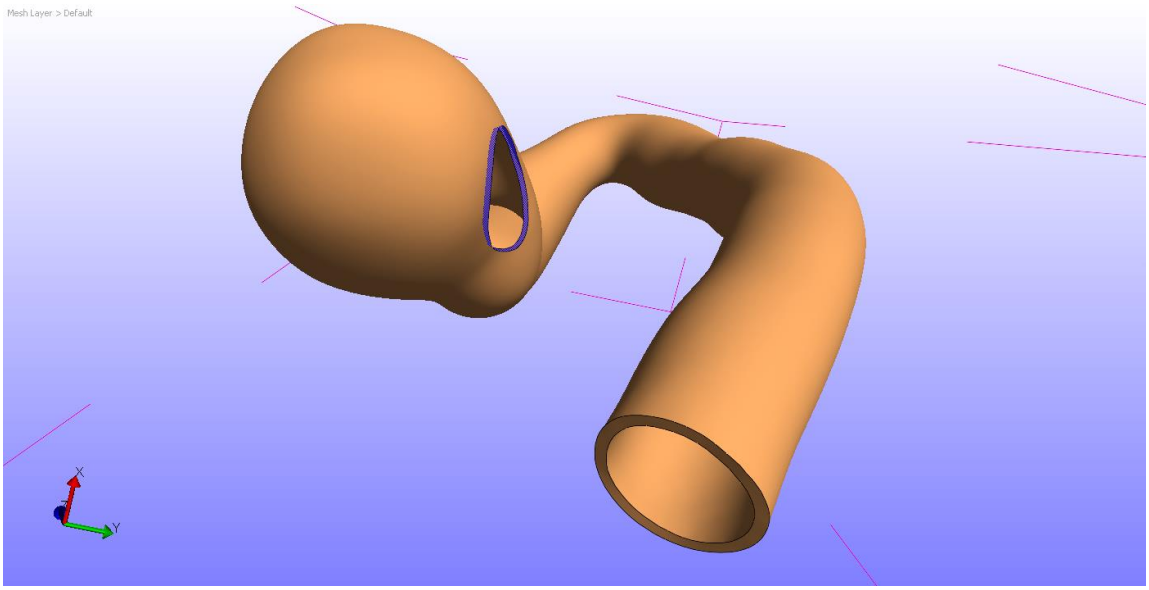

(a)

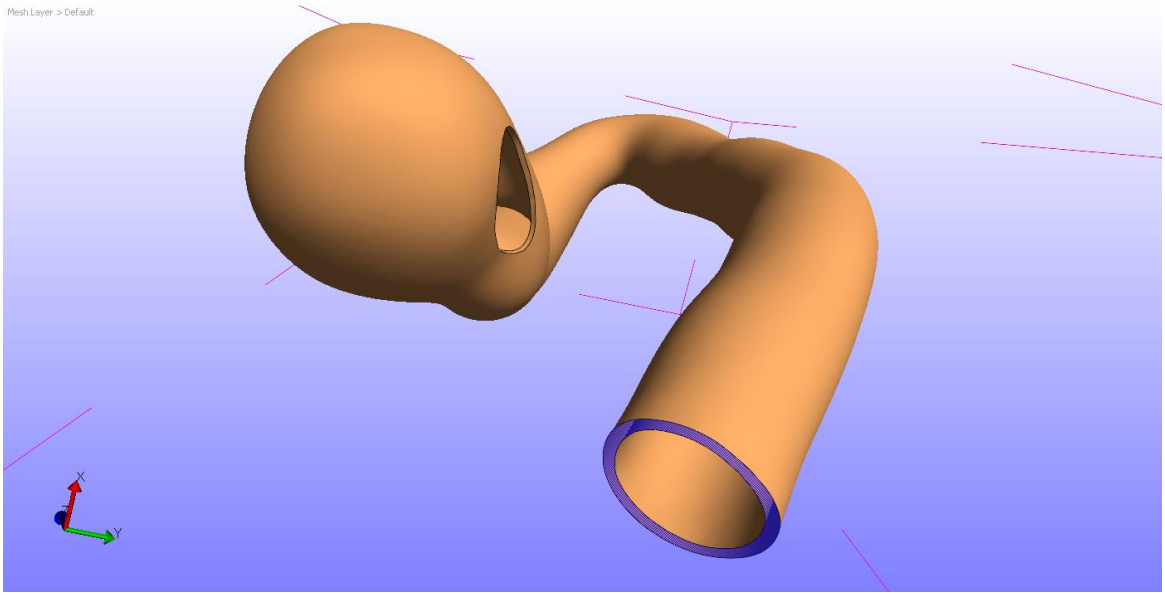

(b)

Figure 2.41. Fixing both ends of the aorta model.

Similarly, the same linear elastic, isotropic material was used with a Poisson coefficient of 0.49 and the elastic modulus was calculated from (Figure 2.34) for both pressures, using an aneurysmal diameter value of 70 mm, as it was observed from the CT scan data that the aneurysmatic tissue stretched up to 7 cm at its most extended point (Figure 2.42).

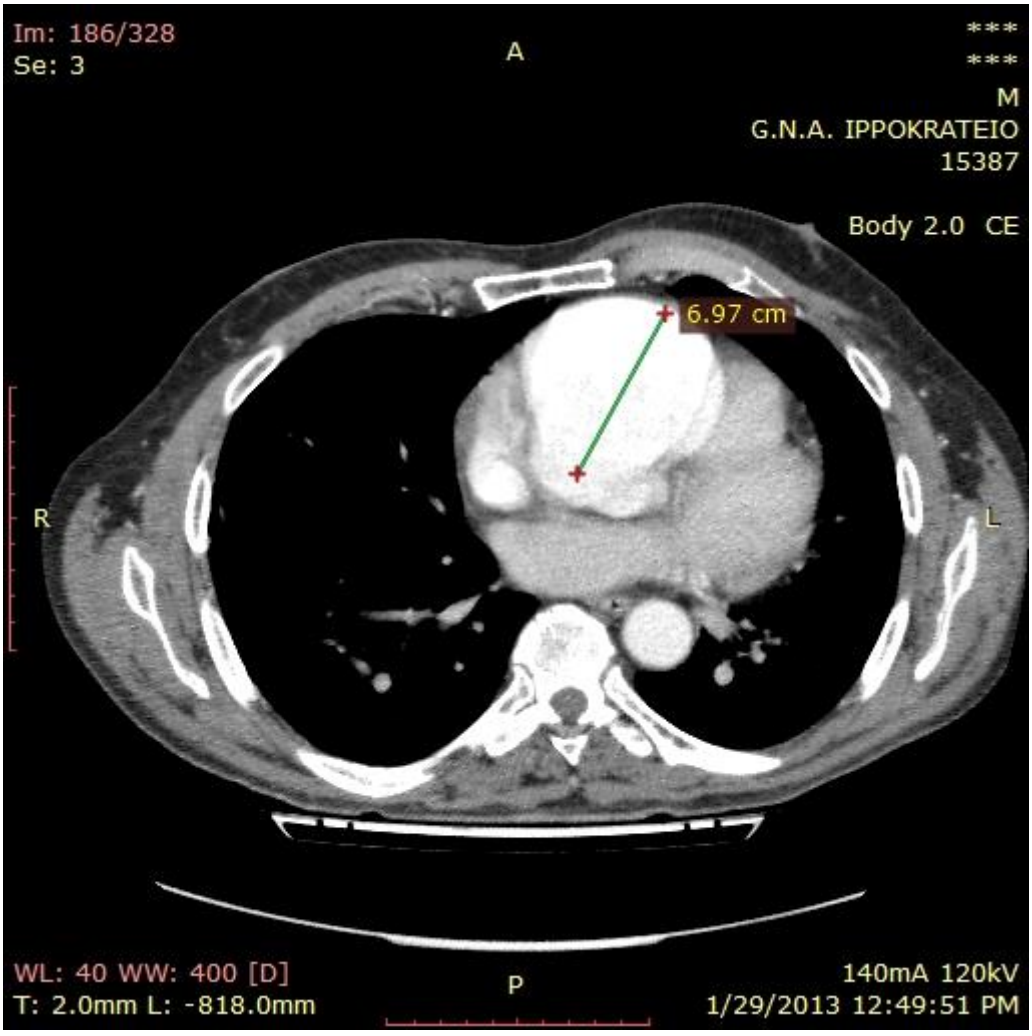

Figure 2.42. CT slice showing the maximal diameter of the aneurysm extending up to 7 cm.

At this point, having thoroughly described the analysis in this chapter and taking into account the plethora of steps that were followed in order to complete the study, it was decided that a flowchart would help to better understand and visualize the entire process. To this end, the diagram below was drawn.

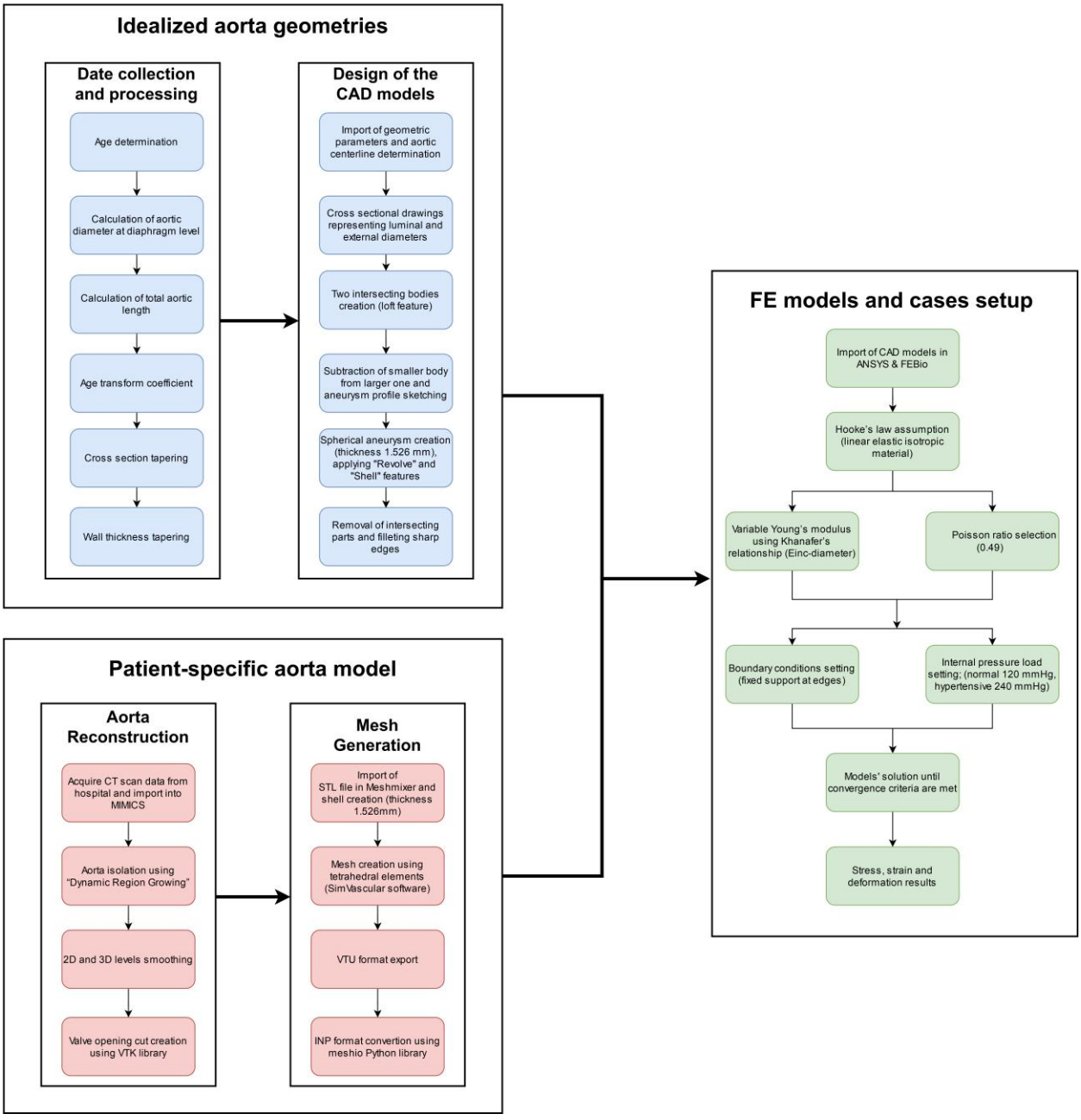

Figure 2.43. Flowchart illustrating the consecutive stages of the analysis.

3. Results

3.1 Pathological cases

Once the FEA simulations were completed, we were able to visualize the stress and strain distributions for the idealized models and the patient specific geometry and list them in the form of screenshots. It can be easily observed that both the CAD models and the patient-specific geometry develop high stress and strain values in the outer surface of the vessel, at the beginning of the aneurysm bulge.

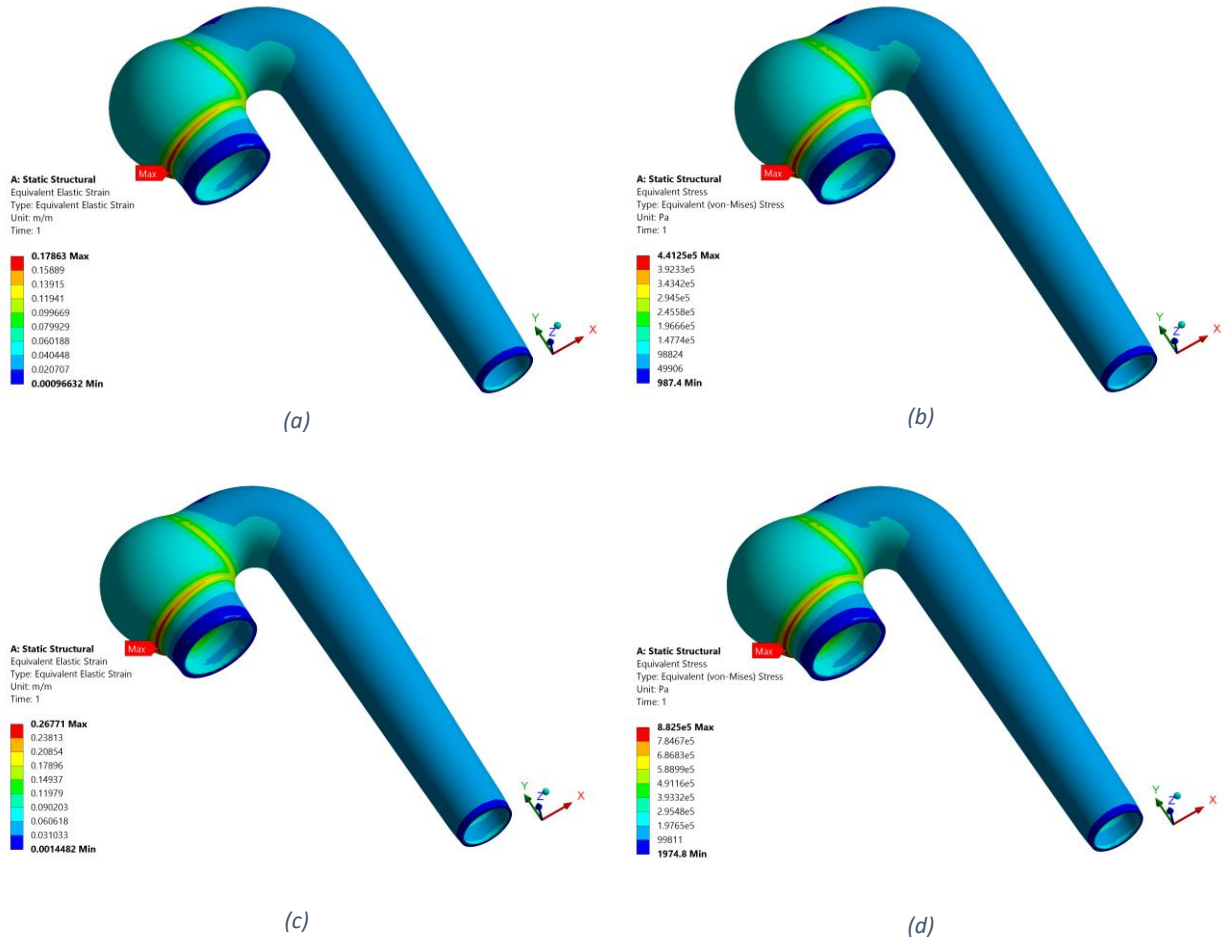

Figure 3.1. BSA=2.0 m^2 aneurysmal diameter D=55mm (a). Equivalent Elastic Strain at 120 mmHg (b). Von-Mises Stress at 120 mmHg (c). Equivalent Elastic Strain at 240 mmHg (d). Von-Mises Stress at 240 mmHg

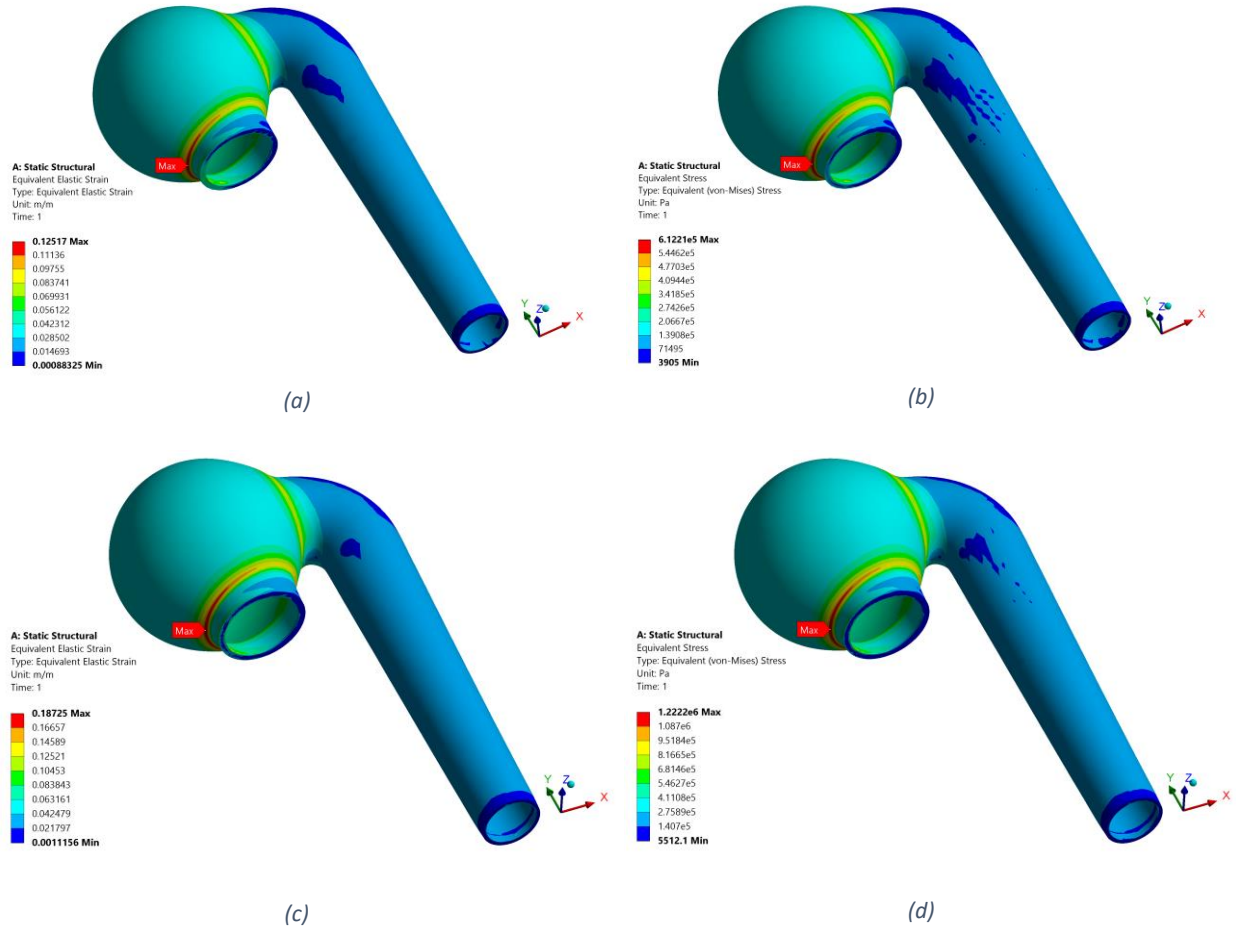

Figure 3.2. BSA=2.0 m² aneurysmal diameter D=77.5mm (α). Equivalent Elastic Strain at 120 mmHg (b). Von-Mises Stress at 120 mmHg (c). Equivalent Elastic Strain at 240 mmHg (d). Von-Mises Stress at 240 mmHg

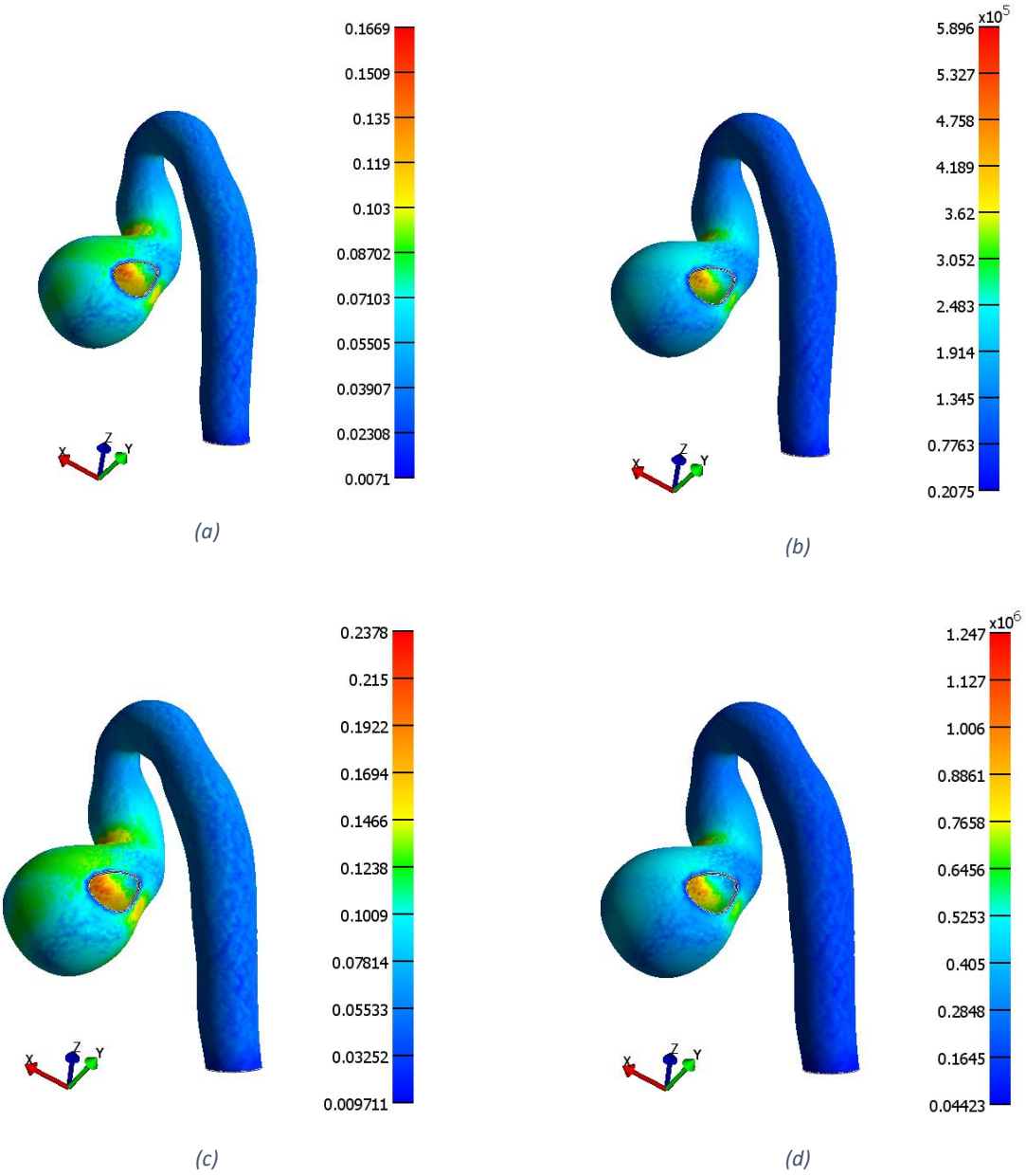

Figure 3.3. Patient case (α). Equivalent Elastic Strain at 120 mmHg (b). Von-Mises Stress at 120 mmHg (c). Equivalent Elastic Strain at 240 mmHg (d). Von-Mises Stress at 240 mmHg

The diagrams provided in the next pages illustrate the results that were drawn from the simulations. More specifically, the data below represent the maximum stress and strain that occur on the wall of the aortic models, for every BSA examined, when loaded with the pressure of 120 mmHg and 240 mmHg, in relation to the maximal diameter of the aneurysm.

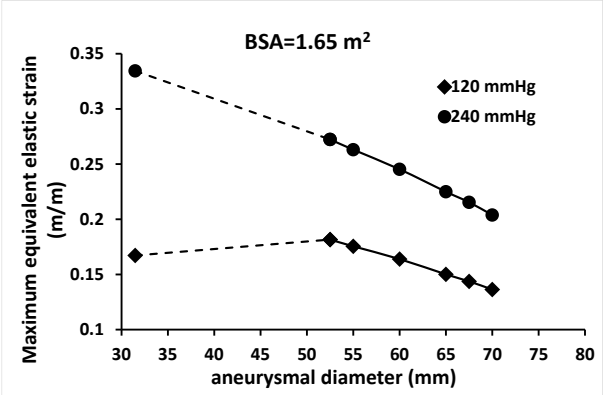

(a)

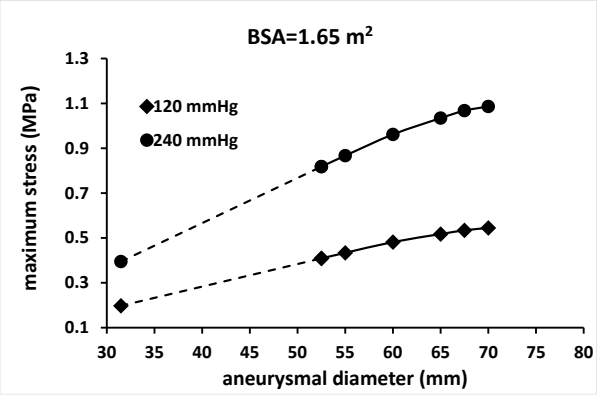

(b)

Figure 3.4. BSA=1.65 m²; (a) Maximum Equivalent Elastic Strain (m/m) – Aneurysmal Diameter (mm). (b) Maximum Stress (MPa) – Aneurysmal diameter (mm).

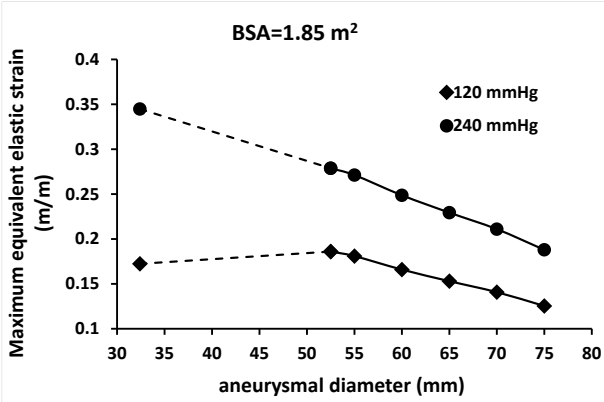

(a)

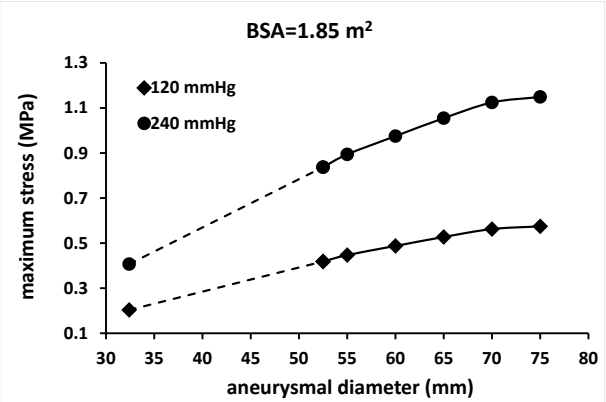

(b)

Figure 3.5. BSA=1.85 m²; (a) Maximum Equivalent Elastic Strain (m/m) – Aneurysmal Diameter (mm). (b) Maximum Stress (MPa) – Aneurysmal diameter (mm).

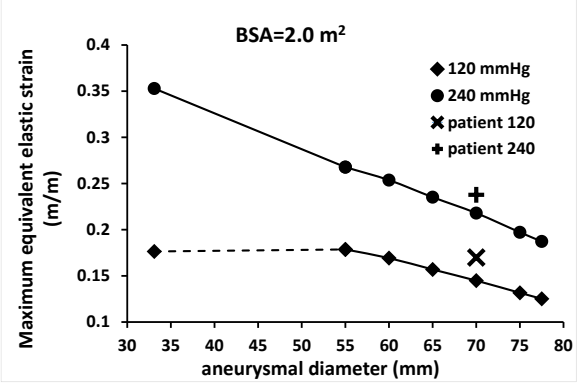

(a)

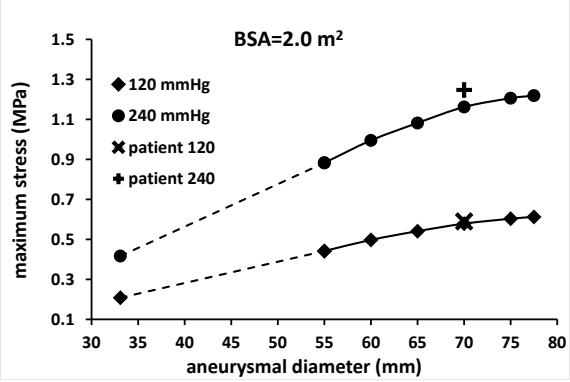

(b)

Figure 3.6. BSA=2.00 m²; (a) Maximum Equivalent Elastic Strain (m/m) – Aneurysmal Diameter (mm). (b) Maximum Stress (MPa) – Aneurysmal diameter (mm).

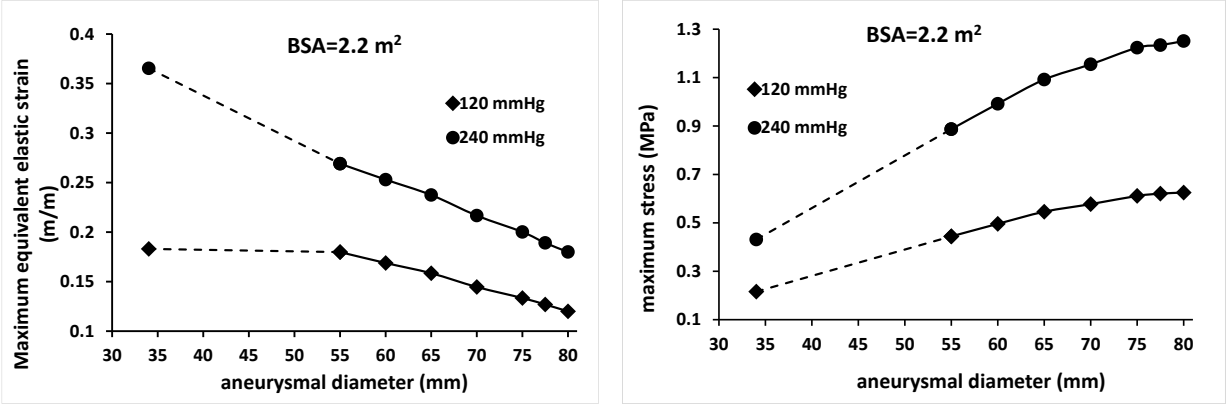

(a) *(b)*

Figure 3.7. BSA=2.20 m²; (a) Maximum Equivalent Elastic Strain (m/m) – Aneurysmal Diameter (mm). (b) Maximum Stress (MPa) – Aneurysmal diameter (mm).

It is clear from the diagrams that all line graphs that refer to the same size, follow the same trend. In particular, as can be seen from the strain - aneurysmal diameter diagrams, as the diameter increases, the wall stress decreases almost linearly for the pathological cases examined. However, in stress - diameter diagrams, the displayed values are proportional. More specifically, as the diameter increases, so does the wall stress while it seems that this increase is happening at a declining pace. The behavior of both trends can be attributed to the fact that as the diameter grows the elastic modulus (E_{inc}) increases (Figure 2.32, Figure 2.34), while a constant internal pressure is applied. In support of this, Koullias states in his paper that "High E_{inc} values essentially imply that in a prerupture phase applied force tends to cause less deformation (strain) simply because the aortic wall tissue has already been stretched to its maximum." [40].

Essentially, we witness a verification of the Laplace law; $\sigma = \frac{D*\Delta p}{4t}$, i.e. a proportional relationship between wall stress and aneurysm diameter so it is fair to state that, in this case, risk of rupture increases in accordance with aneurysm size.

Additionally, we know, from literature, that the failure stresses of the aneurysmatic aortic tissue in aTAA's range between 1.1-1.2 MPa for the longitudinal and 1.6-1.9 MPa for the circumferential direction [43]. Comparing those ranges with the maximum stresses that were obtained from our simulations, we see that the values are of the same order of magnitude, meaning that the analysis produced realistic results. Moreover, we observe that some values of maximum stresses for the hypertensive case are higher than the failure stresses in the longitudinal and circumferential direction so in those cases there would be rupture of the aortic wall.

Last but not least, Figure 3.6 shows the idealized model of BSA=2.0 m^2 in comparison with the geometry reconstructed from the patient's CT data. It is safe to say that the results of the CAD models approach the stress and strain results of the patient specific case with an acceptable error. More precisely, at 120 mmHg the patient model presented strain equal to 0.167 m/m and 0.238 m/m at 240 mmHg. The idealized model, on the other hand, experienced a strain of 0.145 m/m and 0.218 m/m when loaded with normal pressure and hypertensive respectively. Regarding stress, the deviations were even smaller. At 240 mmHg the patient specific case met stress load that amounted to 1.25 MPa and the artificial geometry 1.16 MPa while at 120 mmHg both stress values rounded up to approximately 0.58 MPa.

3.2 Normal cases

Simulations were also carried out for the non-pathological, idealized aortic models and the results extracted are depicted thoroughly through screenshots of the completed simulations as well as in the form of charts. The FE models appear to develop high stress concentration on the inner side of the aortic arch.

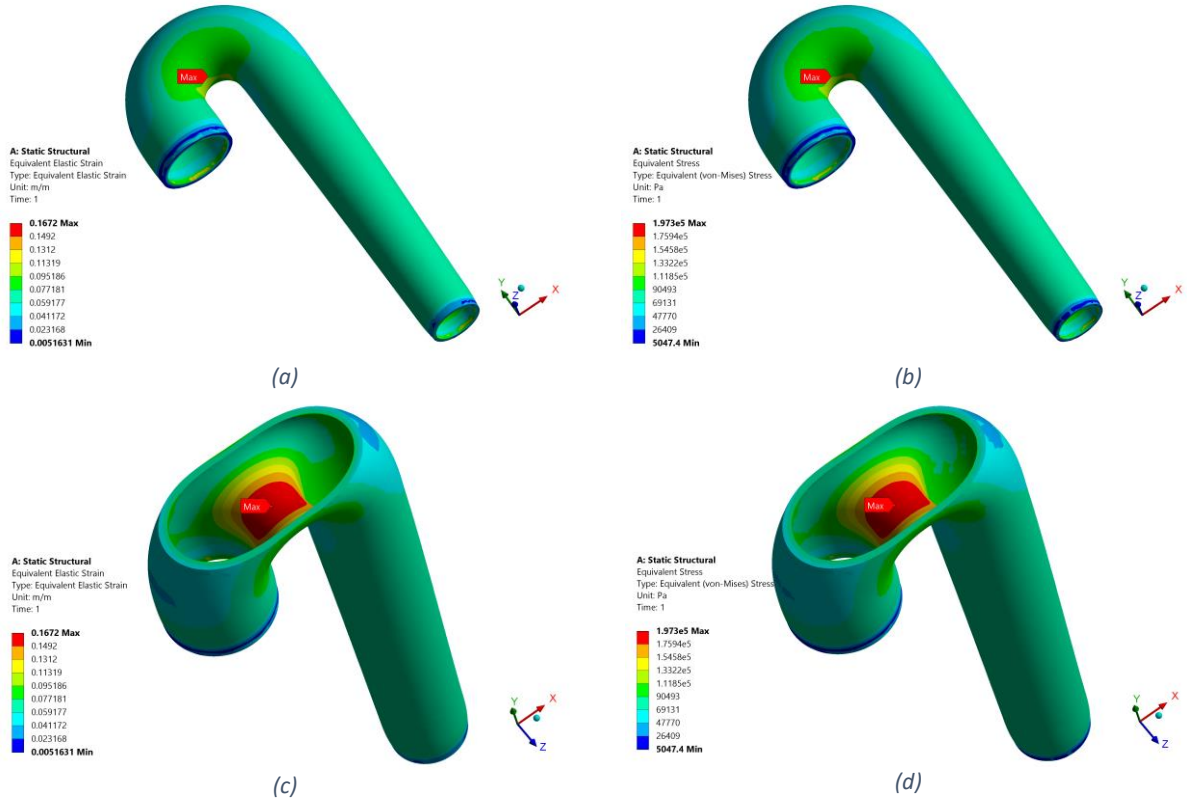

Figure 3.8. BSA=1.65 m^2, 120 mmHg; (a) Equivalent Elastic Strain (m/m) with a section view in (c). (b) Equivalent Stress with a section view in (d).

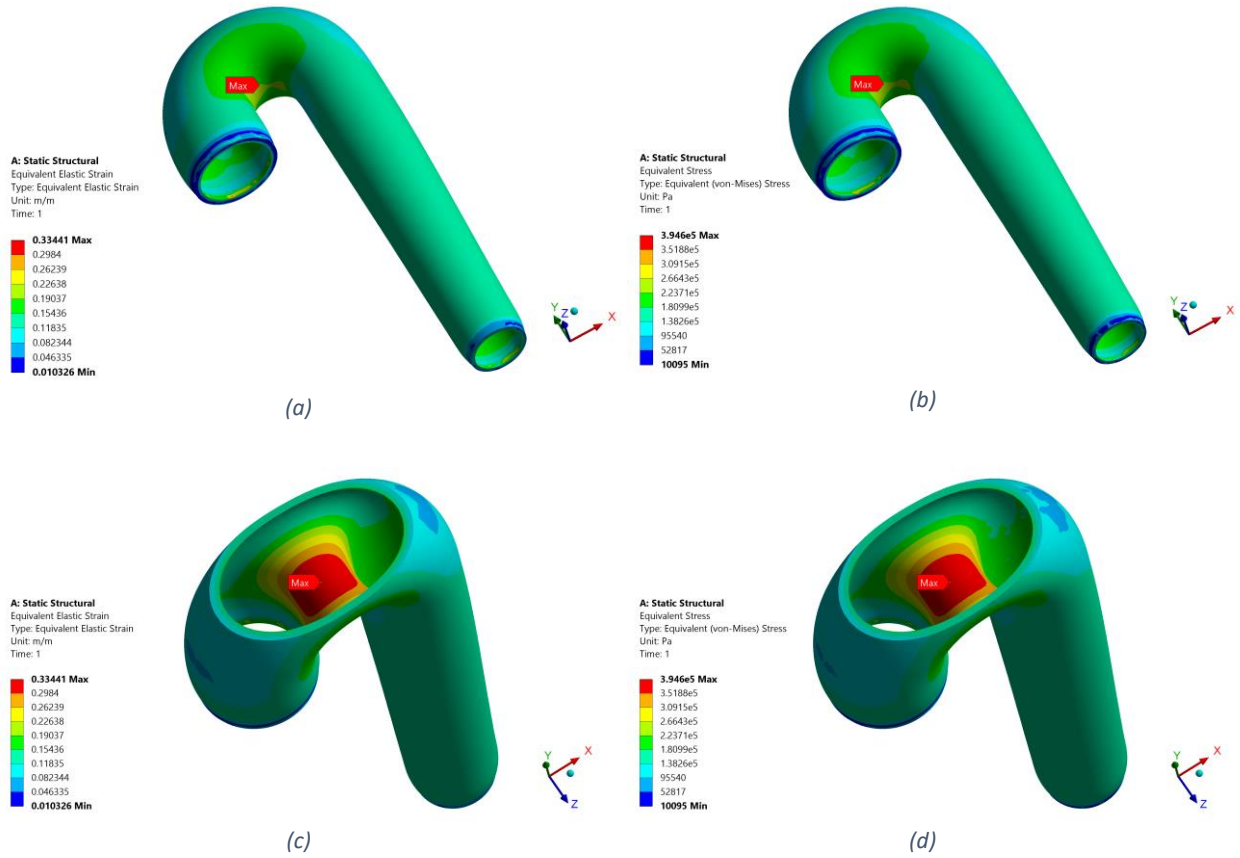

Figure 3.9. BSA=1.65 m^2, 240 mmHg; (a) Equivalent Elastic Strain (m/m) with a section view in (c). (b) Equivalent Stress with a section view in (d).

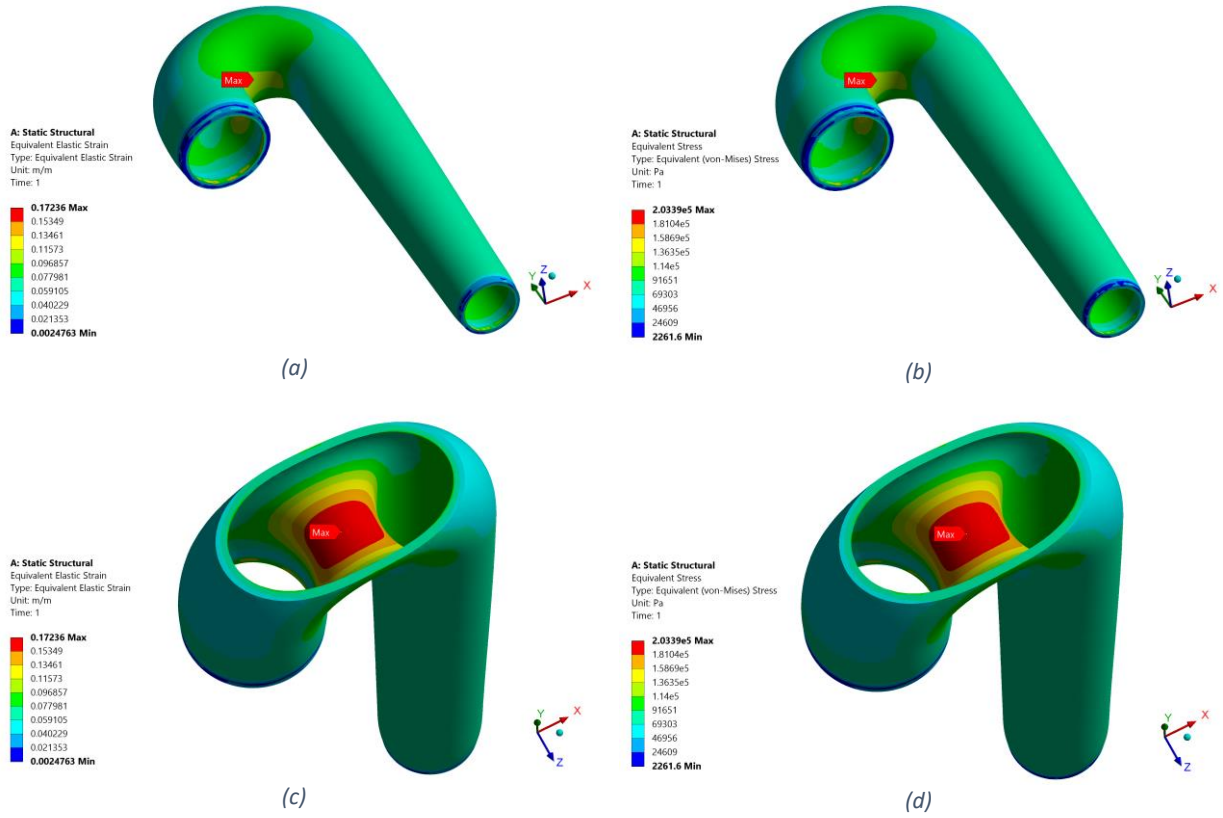

Figure 3.10. BSA=1.85 m², 120 mmHg; (a) Equivalent Elastic Strain (m/m) with a section view in (c). (b) Equivalent Stress with a section view in (d).

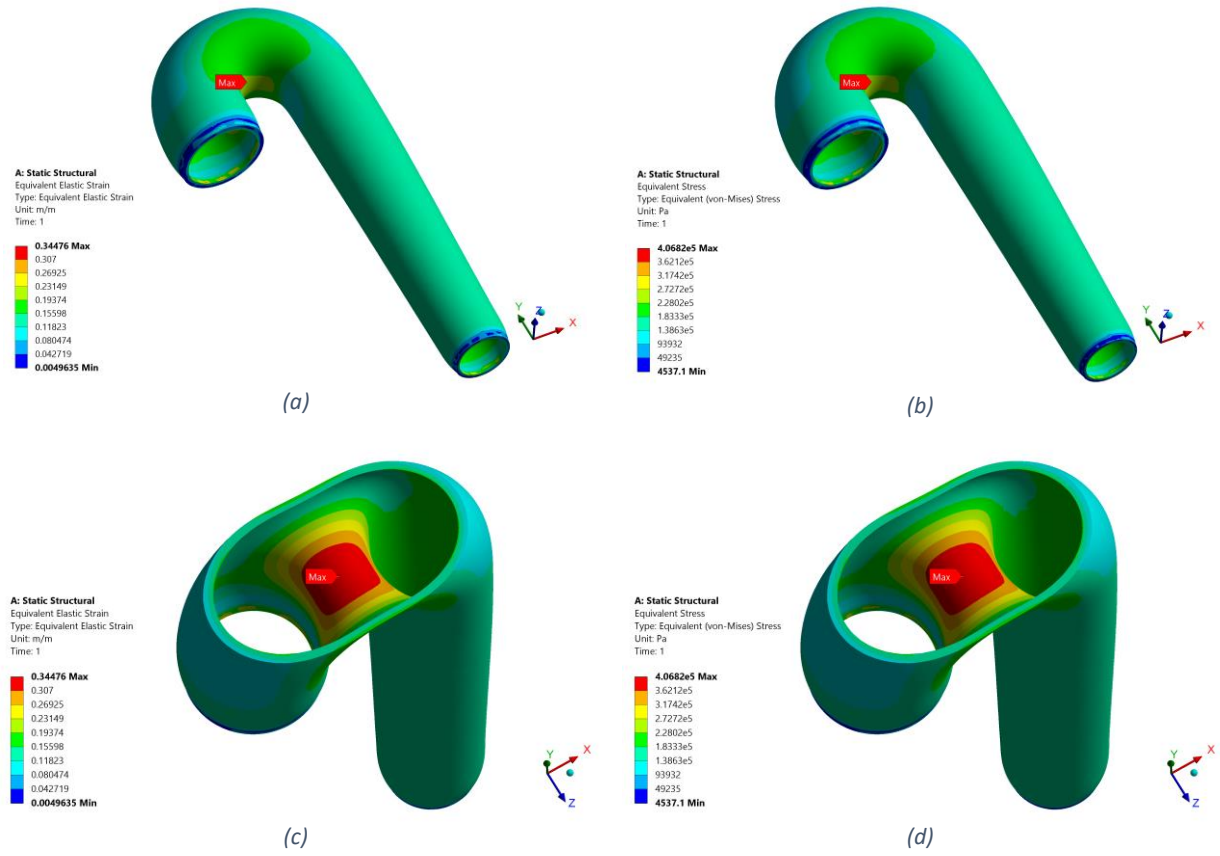

Figure 3.11. BSA=1.85 m², 240 mmHg; (a) Equivalent Elastic Strain (m/m) with a section view in (c). (b) Equivalent Stress with a section view in (d).

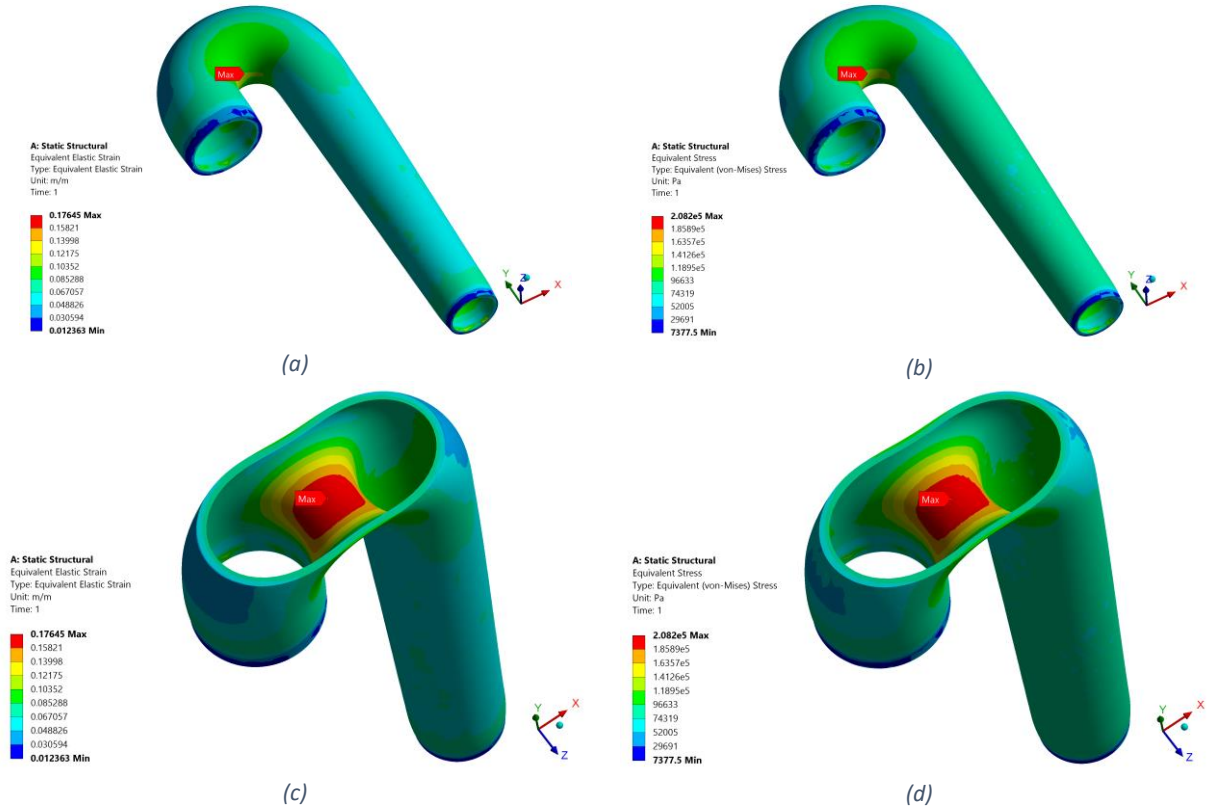

Figure 3.12. BSA=2.0 m^2, 120 mmHg; (a) Equivalent Elastic Strain (m/m) with a section view in (c). (b) Equivalent Stress with a section view in (d).

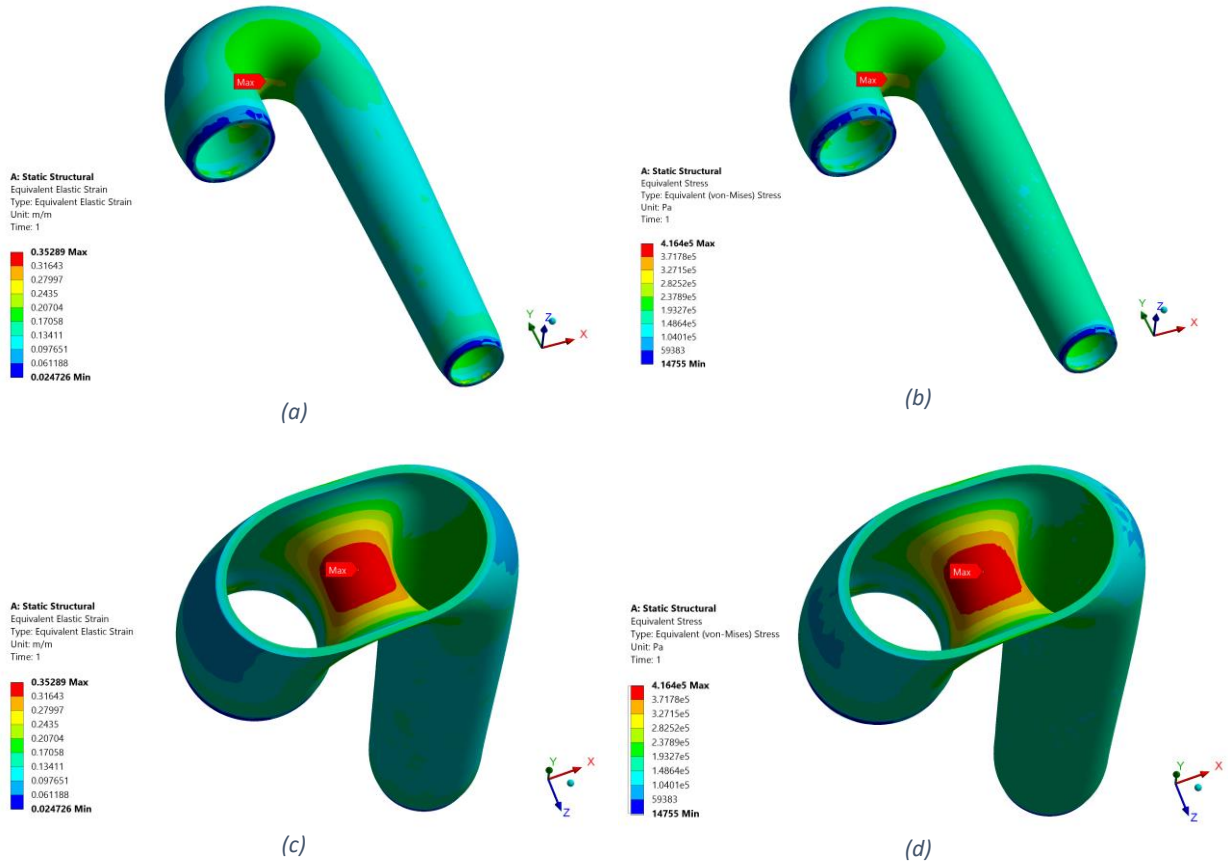

Figure 3.13. BSA=2.0 m^2, 240 mmHg; (a) Equivalent Elastic Strain (m/m) with a section view in (c). (b) Equivalent Stress with a section view in (d).

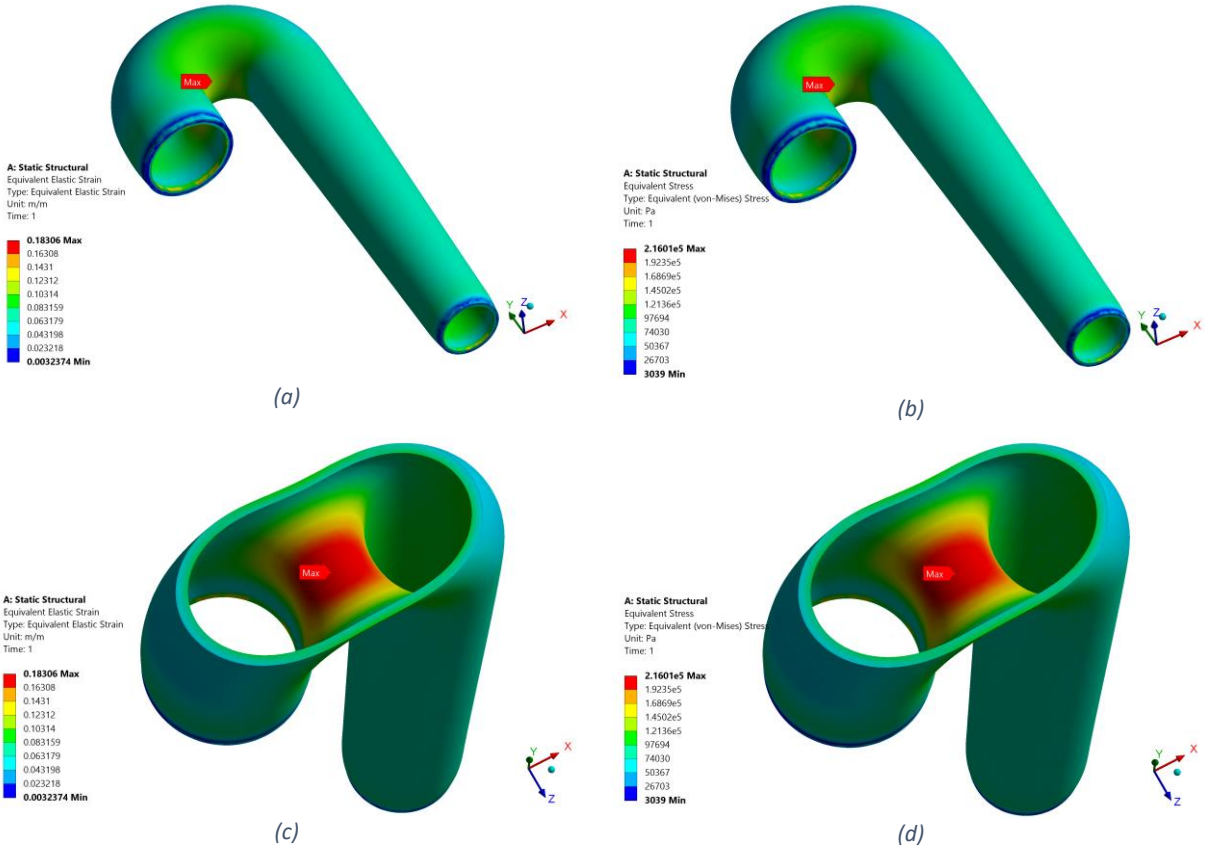

Figure 3.14. BSA=2.2 m^2, 120 mmHg; (a) Equivalent Elastic Strain (m/m) with a section view in (c). (b) Equivalent Stress with a section view in (d).

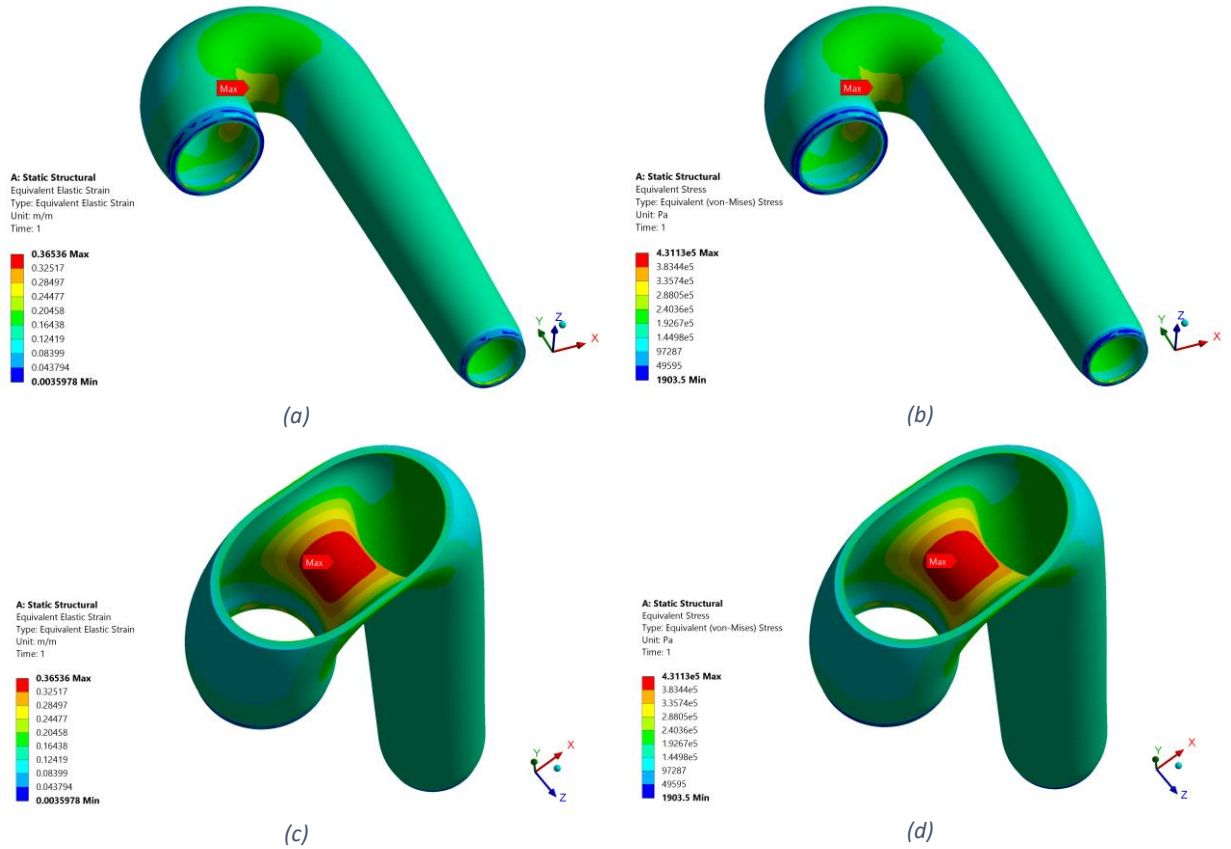

Figure 3.15. BSA=2.2 m^2, 240 mmHg; (a) Equivalent Elastic Strain (m/m) with a section view in (c). (b) Equivalent Stress with a section view in (d).

The line graphs below compare the maximum stress, maximum strain, maximum deformation and average stress among the four examined BSA values for the pressures of 120 mmHg and 240 mmHg - physiological and hypertensive respectively.

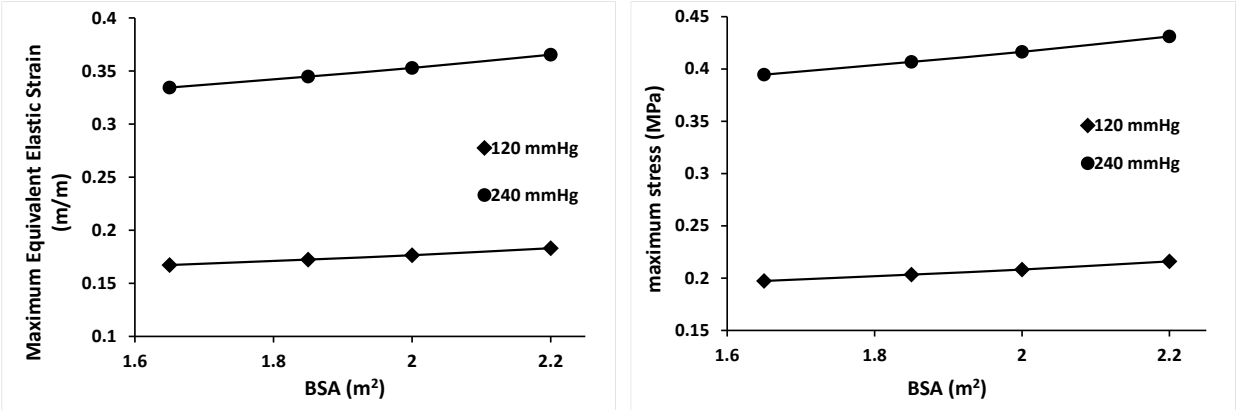

Figure 3.16. (a) Maximum Equivalent Elastic Strain (m/m) – BSA (m^2). (b) Maximum Stress (MPa) – BSA (m^2).

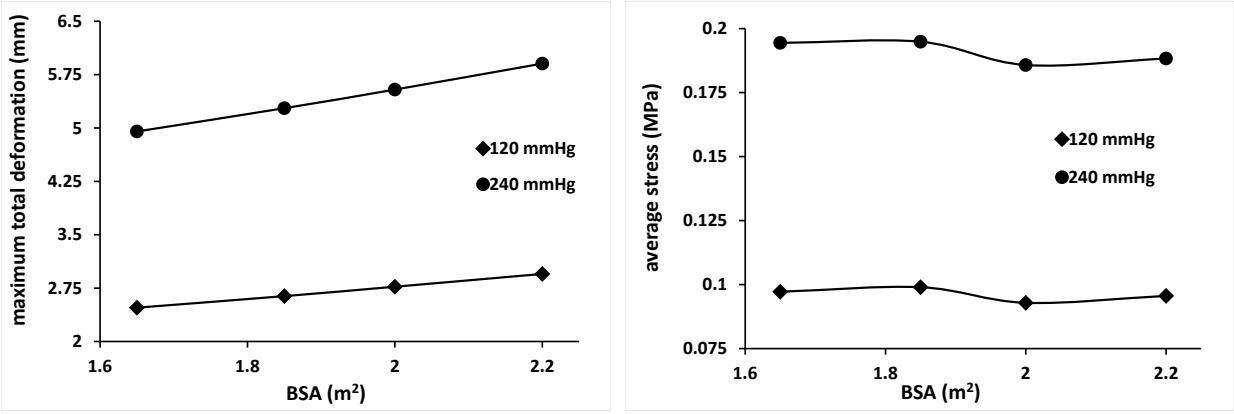

(a) *(b)*

Figure 3.17. (a) Maximum Total Deformation (mm) – BSA (m^2). (b) Average Stress (MPa) – BSA (m^2).

It is evident that as the BSA value increases, the maximum total deformation experiences a marked increase, while a constant, uniform pressure is applied. The same can be said about the BSA - maximum stress and maximum strain diagrams, although the increase is less noticeable in these diagrams. Finally, the average stress curve undergoes a marginal decline in the higher BSA values, but overall, it remains almost constant, as the BSA increases. Furthermore, it is easily observed from the charts that the stress, strain and deformation values were higher in hypertensive load state (240 mmHg) than in the normal load state (120 mmHg).

It is, also, important to note that the pathological geometries present maximum stress and strain values on the exterior aneurysmal wall close to the aortic valve, while the normal CAD models appear to have a peak of the extracted results on the inside of the aorta and specifically on the greatest curvature of the geometry, that is in the middle of the aortic arch.

Finally, it was deemed useful to show the covariations of the maximum stress and strain values in relation to the BSA and the aneurysmal diameter by creating four contour charts (Figure 3.18). These charts, indicate that a simultaneous increase of the aneurysmal diameter and the BSA, results in a rise of maximum stress value in contrast with the maximum strain value that drops as those two sizes grow.

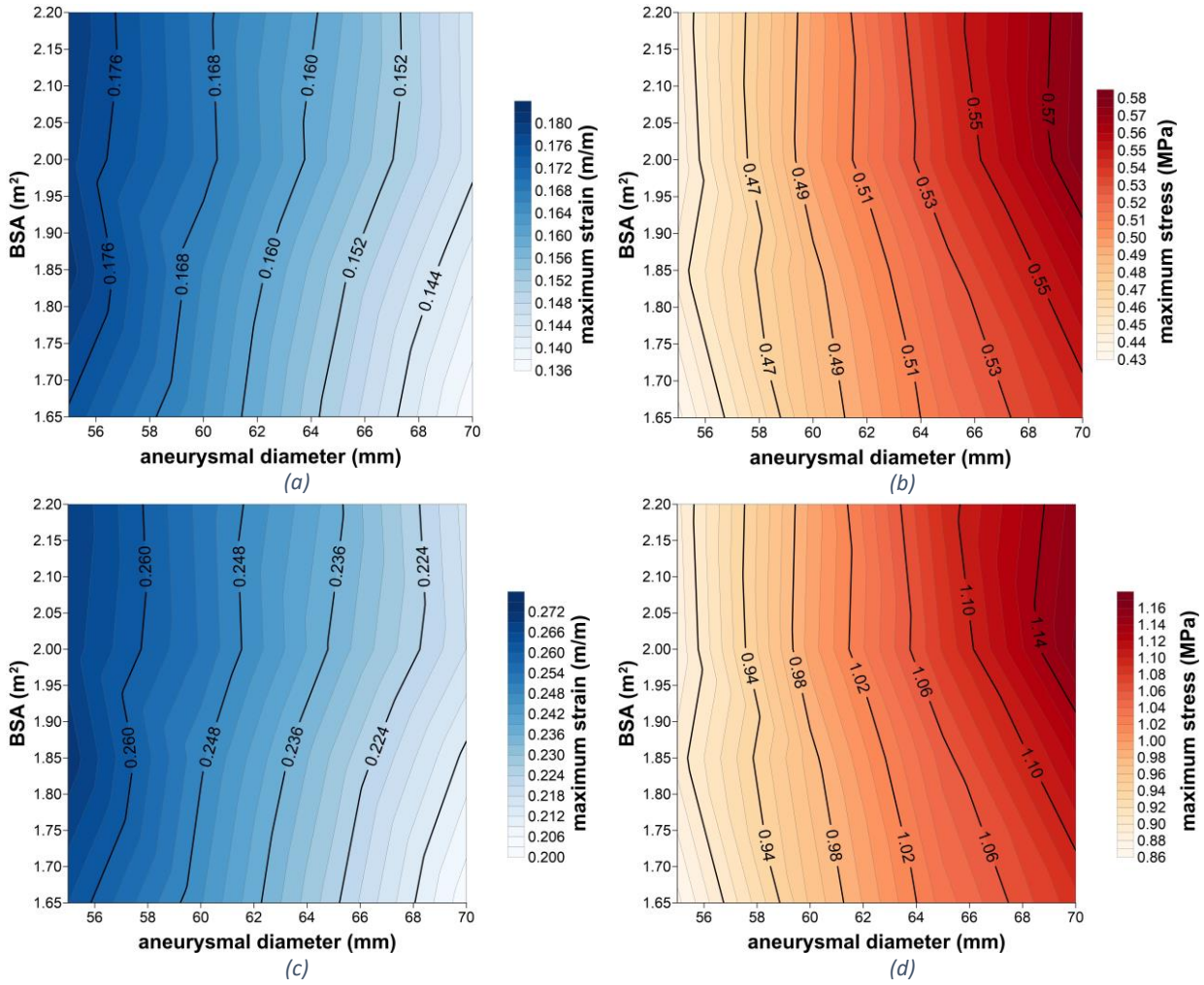

Figure 3.18. (a) BSA (m^2)-aneurysmal diameter (mm)-maximum strain (m/m); 120 mmHg. (b) BSA (m^2)-aneurysmal diameter (mm)-maximum stress (MPa); 120 mmHg. (c) BSA (m^2)-aneurysmal diameter (mm)-maximum strain (m/m); 240 mmHg. (d) BSA (m^2)-aneurysmal diameter (mm)-maximum stress (MPa); 240 mmHg.

4. Conclusions and suggestions for future research

4.1 Conclusions

In the present thesis, a number of normal and aneurysmal, idealized geometries are designed for different BSA values, and for each one of these geometries we show the stress state of the aortic wall under normal and hypertensive luminal pressure. At the same time, a pathological, individualized case of ascending thoracic aortic aneurysm (aTAA) is examined.

The results show that:

- the maximum stress and strain values develop at the proximal neck of the aneurysm, where the expansion begins.
- the maximum stress increases in proportion to the internal pressure and the maximum diameter of the aneurysm, while the strain, also, increases proportionally with internal pressure but decreases when the aneurysmal diameter rises.
- the values of maximum stress, maximum strain and maximum deformation experience an increasing trend, as a function of BSA.
- the maximum stress and maximum strain of the patient geometry reach values close to those of the idealized models when it comes to matching BSA values. Therefore, models of idealized geometries can be used to assess the stress state of the aortic wall in real patients.

4.2 Future research

Below are listed some topics in areas of interest for possible future research.

- Model the material of the aorta as anisotropic and non-linear in terms of the stress-strain relationship. Models such as the Gasser–Ogden–Holzapfel or Fung should be used.
- Examine and compare as many cases of aneurysmal individualized geometries as possible in order to decide on the reliability of the present model and the extent to which we can include its predictions during the treatment process of a patient.
- Insert not only the maximum systolic pressure but also a time variable pressure profile (pressure-transient analysis), as it actually happens during a cardiac cycle.
- Include and model adjacent tissues such as the heart muscle, the pericardial cavity, and other vessels such as pulmonary artery, as they create a support on the wall of the aorta and affect the stress state.
- Insert fluid to model the blood and study the stress state of the aortic wall using Fluid-Structure Interaction (FSI).
- Study the behavior of the aortic wall by carrying out a fatigue analysis. Having the parameters of the Wöhler curve for the aortic wall material as givens, by literature, and having computed the stress amplitude from load cycles (by loading the model with alternating internal pressure), one can determine the failure cycles of the material and predict when the aortic wall rupture will happen.

References

1. Braunwald, E., D.P. Zipes, and P. Libby, *Heart disease : a textbook of cardiovascular medicine*. 6th ed., edited by Eugene Braunwald, Douglas P. Zipes, peter Libby. ed. 2001, Philadelphia ; London: Saunders.
2. Hickson, S.S., et al., *The Relationship of Age With Regional Aortic Stiffness and Diameter.* JACC: Cardiovascular Imaging, 2010. **3**(12): p. 1247-1255.
3. Vorp, D.A., et al., *Effect of aneurysm on the tensile strength and biomechanical behavior of the ascending thoracic aorta.* The Annals of Thoracic Surgery, 2003. **75**(4): p. 1210-1214.
4. Vorp, D.A., *Biomechanics of abdominal aortic aneurysm.* J Biomech, 2007. **40**(9): p. 1887-902.
5. Dobrin, P.B., *Pathophysiology and pathogenesis of aortic aneurysms. Current concepts.* Surg Clin North Am, 1989. **69**(4): p. 687-703.
6. Coady, M.A., et al., *What is the appropriate size criterion for resection of thoracic aortic aneurysms?* The Journal of Thoracic and Cardiovascular Surgery, 1997. **113**(3): p. 476-491.
7. Elefteriades, J.A., *Natural history of thoracic aortic aneurysms: indications for surgery, and surgical versus nonsurgical risks.* The Annals of Thoracic Surgery, 2002. **74**(5): p. S1877-S1880.
8. Davies, R.R., et al., *Novel measurement of relative aortic size predicts rupture of thoracic aortic aneurysms.* Ann Thorac Surg, 2006. **81**(1): p. 169-77.
9. *Circulatory system anatomy vector jpg preview image*. Available from: https://www.vectorstock.com/royalty-free-vector/circulatory-system-anatomy-vector-27211255.
10. Camm, A.J., T.F. Lüscher, and P.W. Serruys, *The ESC textbook of cardiovascular medicine*. 2006, Malden, Mass.: Blackwell Pub.
11. *The structure of an artery wall*. Medical gallery of Blausen Medical 2014; Available from: https://commons.wikimedia.org/w/index.php?title=File:Blausen_0055_ArteryWallStructure.png&oldid=284404447.
12. *Illustration of normal thoracic aortic anatomy*. Available from: https://basicmedicalkey.com/thoracic-aneurysms-and-aortic-dissection/.
13. *Diagram of the aorta*. Available from: https://www.clevelandclinic.org/heartcenter/images/guide/disease/marfan/aortaLG.jpg.
14. *Types of aneurysms*. Available from: https://drhakangercekoglu.com/wp-content/uploads/2017/12/anevrizma-tipleri.jpg.
15. *Abdominal aortic aneurysms*. Available from: http://aortainstitute.co.uk/wp-content/uploads/2018/01/Abdominal-Aortic-Aneurysm-AAA-e1517239227232.jpg.
16. *Thoracic aortic aneurysms*. Available from: https://www.cardiachealth.org/wp-content/uploads/2015/06/thoracic-aneurysms.jpg.
17. *Thoracoabdominal aneurysms*. Available from: https://www.mainlinehealth.org/-/media/images/conditions-and-treatments/aortic/thoracoabdominal-aneurysm-types-1-to-4.jpg?h=549&w=705&la=en&hash=C7D884FBDCDD6DE6A51C81C4BF7B61B94542E84E.
18. Turkbey, E.B., et al., *Determinants and normal values of ascending aortic diameter by age, gender, and race/ethnicity in the Multi-Ethnic Study of Atherosclerosis (MESA).* Journal of Magnetic Resonance Imaging, 2014. **39**(2): p. 360-368.
19. Azadani, A.N., et al., *Biomechanical properties of human ascending thoracic aortic aneurysms.* Ann Thorac Surg, 2013. **96**(1): p. 50-8.
20. Duprey, A., et al., *Biaxial rupture properties of ascending thoracic aortic aneurysms.* Acta Biomaterialia, 2016. **42**: p. 273-285.
21. Evangelista, A., *Aneurysm of the ascending aorta.* Heart, 2010. **96**(12): p. 979.

22. Iliopoulos, D.C., et al., *Ascending thoracic aortic aneurysms are associated with compositional remodeling and vessel stiffening but not weakening in age-matched subjects.* J Thorac Cardiovasc Surg, 2009. **137**(1): p. 101-9.
23. Wisneski, A.D., et al., *Abstract 10921: Wall Stress of Ascending Thoracic Aortic Aneurysm versus Normal Aorta: Towards Defining Wall-stress Based Thresholds for Aneurysm Intervention.* Circulation, 2019. **140**(Suppl_1): p. A10921-A10921.
24. Wisneski, A.D., et al., *Biomechanics of Ascending Thoracic Aortic Aneurysm: Computational Modeling and Pursuit of Wall Stress Based Rupture Risk.* Journal of the American College of Surgeons, 2019. **229**(4): p. S43-S44.
25. Sorimachi, H., et al., *Sex differences in left ventricular afterload and diastolic function are independent from the aortic size.* PLOS ONE, 2019. **14**(4): p. e0214907.
26. Fung, Y.C., *Biomechanics: Circulation*. 2013: Springer New York.
27. Westerhof, N., et al., *Analog studies of the human systemic arterial tree.* Journal of Biomechanics, 1969. **2**(2): p. 121-143.
28. *Thoracic Aorta anatomy*. Available from: https://thoracickey.com/diseases-of-the-aorta-7/.
29. Van Puyvelde, J., et al., *Aortic wall thickness in patients with ascending aortic aneurysm versus acute aortic dissection.* European Journal of Cardio-Thoracic Surgery, 2015. **49**(3): p. 756-762.
30. Updegrove, A., et al., *SimVascular: An Open Source Pipeline for Cardiovascular Simulation.* Ann Biomed Eng, 2017. **45**(3): p. 525-541.
31. Bergel, D.H., *The static elastic properties of the arterial wall.* The Journal of Physiology, 1961. **156**(3): p. 445-457.
32. Carew, T.E., R.N. Vaishnav, and D.J. Patel, *Compressibility of the arterial wall.* Circ Res, 1968. **23**(1): p. 61-8.
33. Di Martino, E.S., et al., *Fluid-structure interaction within realistic three-dimensional models of the aneurysmatic aorta as a guidance to assess the risk of rupture of the aneurysm.* Med Eng Phys, 2001. **23**(9): p. 647-55.
34. Gao, F., et al., *Fluid-structure Interaction within a Layered Aortic Arch Model.* Journal of biological physics, 2006. **32**: p. 435-54.
35. Hemmasizadeh, A., M. Autieri, and K. Darvish, *Multilayer material properties of aorta determined from nanoindentation tests.* Journal of the Mechanical Behavior of Biomedical Materials, 2012. **15**: p. 199-207.
36. Jayendiran, R., et al., *Computational prediction of hemodynamical and biomechanical alterations induced by aneurysm dilatation in patient-specific ascending thoracic aortas.* International Journal for Numerical Methods in Biomedical Engineering, 2020. **36**(6): p. e3326.
37. Maddali, M., C. Shah, and K. Yang, *Finite Element Modeling of Aortic Tissue Using High Speed Experimental Data*. Vol. 2006. 2005.
38. MERILLON, J.P., et al., *Evaluation of the elasticity and characteristic impedance of the ascending aorta in man.* Cardiovascular Research, 1978. **12**(7): p. 401-406.
39. Nathan, D.P., et al., *Pathogenesis of acute aortic dissection: a finite element stress analysis.* Ann Thorac Surg, 2011. **91**(2): p. 458-63.
40. Koullias, G., et al., *Mechanical deterioration underlies malignant behavior of aneurysmal human ascending aorta.* The Journal of Thoracic and Cardiovascular Surgery, 2005. **130**(3): p. 677.e1-677.e9.
41. Khanafer, K., et al., *Determination of the elastic modulus of ascending thoracic aortic aneurysm at different ranges of pressure using uniaxial tensile testing.* J Thorac Cardiovasc Surg, 2011. **142**(3): p. 682-6.
42. Maas SA, E.B., Ateshian GA, Weiss JA, *FEBio: Finite Elements for Biomechanics.* Journal of Biomechanical Engineering, 2012. **134**(1): p. 011005.

43. Sokolis, D.P. and D.C. Iliopoulos, *Impaired mechanics and matrix metalloproteinases/inhibitors expression in female ascending thoracic aortic aneurysms.* Journal of the Mechanical Behavior of Biomedical Materials, 2014. **34**: p. 154-164.

5. Appendix

Screenshots of the simulation results illustrating stress *(σ)* and strain *(ε)* distributions on the CAD generated models, are presented below in a group of four snapshots per diameter and BSA. Each group shows the physiological state (120 mmHg) in the top pictures and the hypertensive state (240 mmHg) in the bottom ones. Strain is depicted on the left side and stress on the right side of every figure. The caption of each figure states the defining diameter and BSA value.

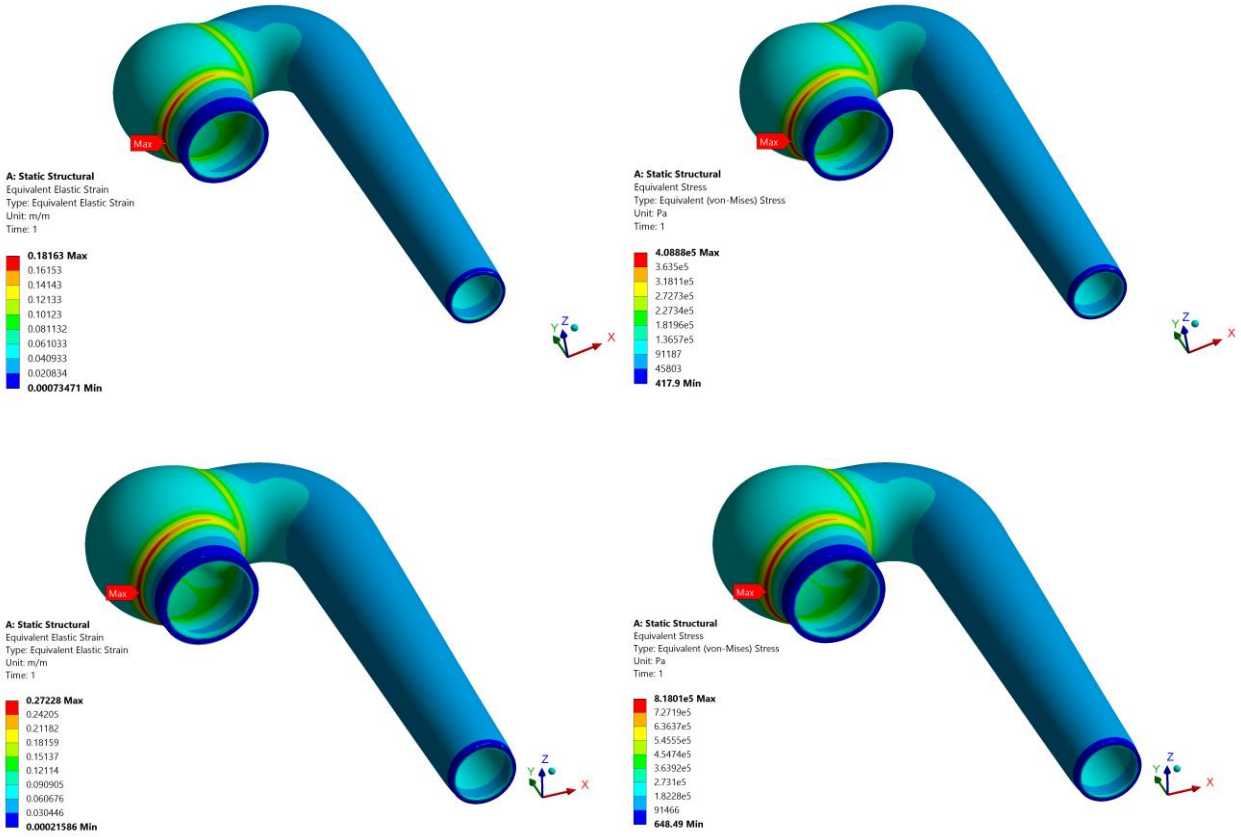

Figure 5.1. BSA=1.65 m^2, aneurysmal diameter = 52.5 mm

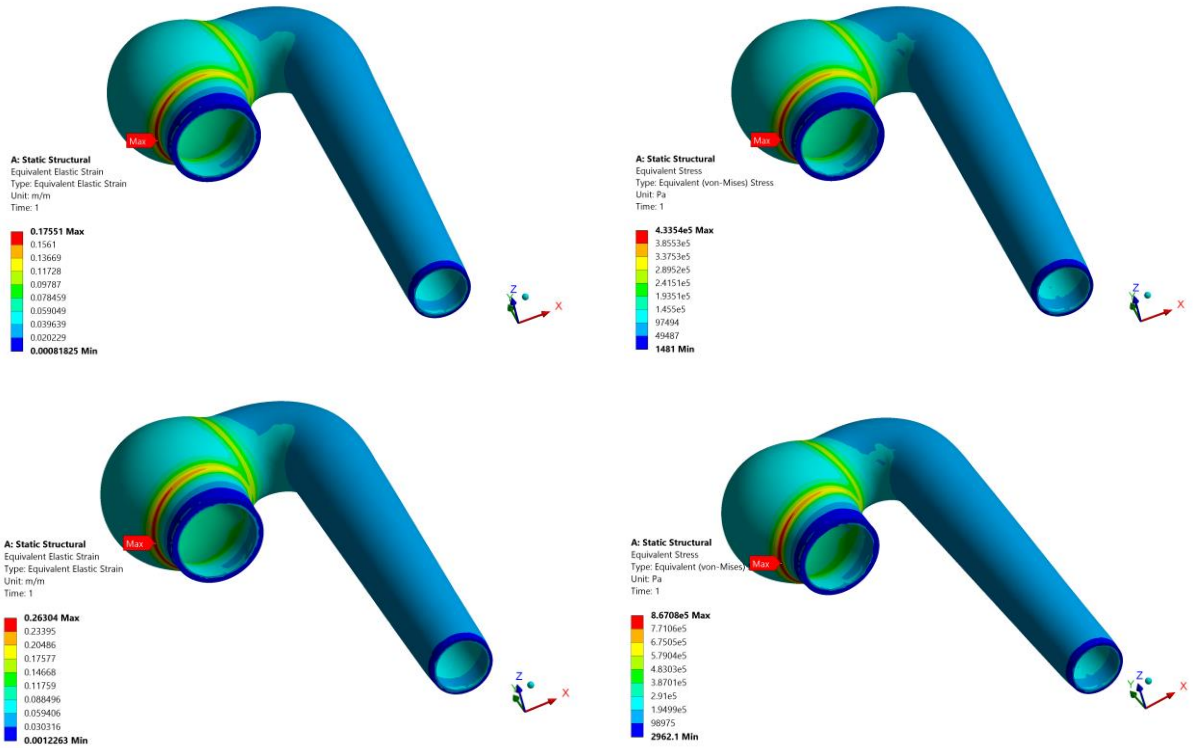

Figure 5.2. BSA=1.65 m², aneurysmal diameter=55 mm

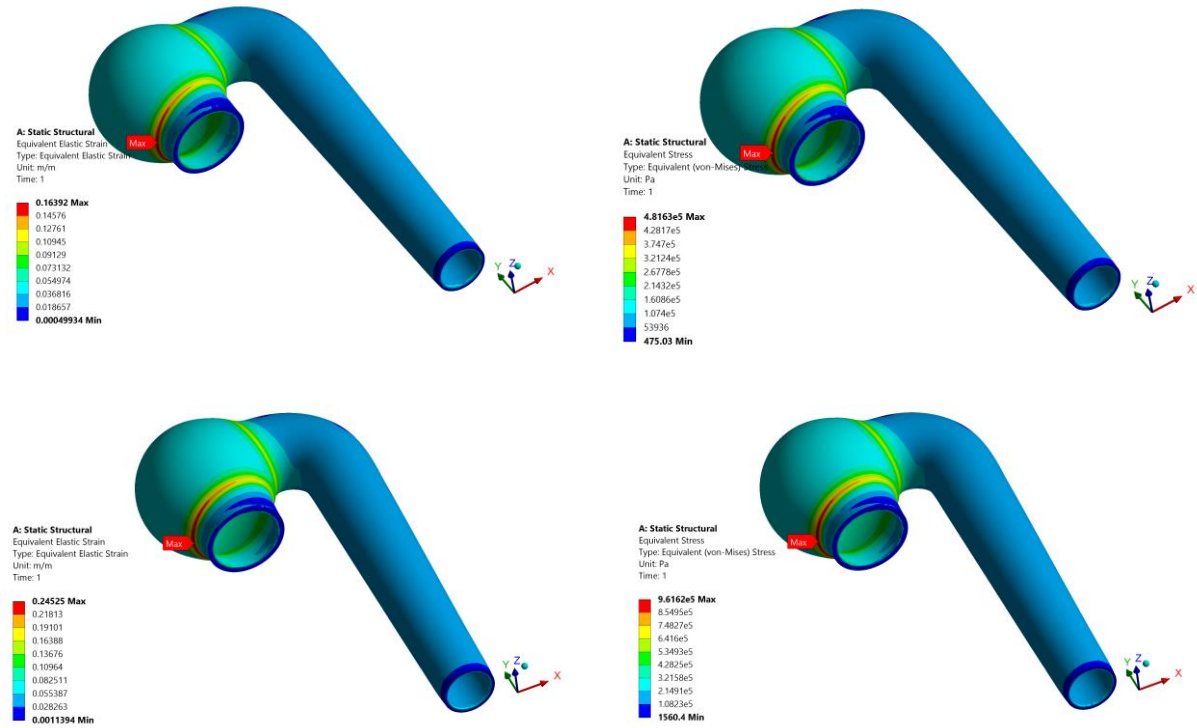

Figure 5.3. BSA=1.65 m², aneurysmal diameter=60 mm

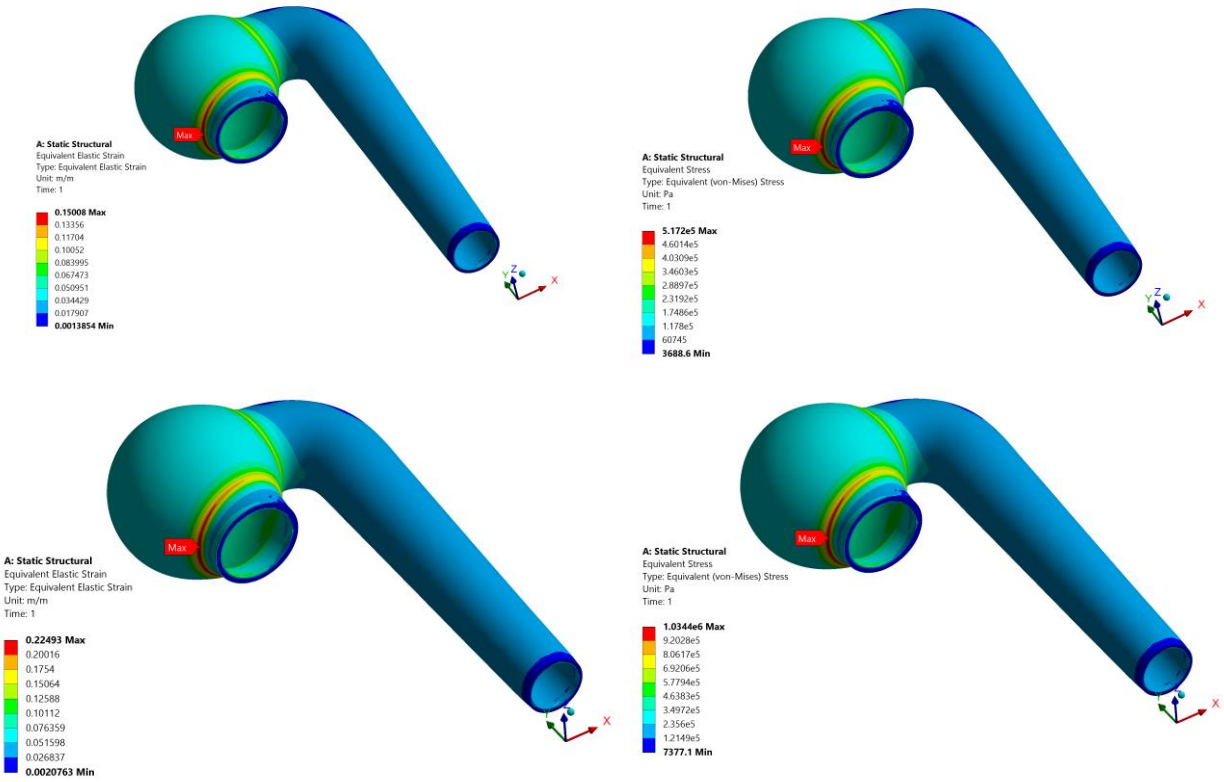

Figure 5.4. BSA=1.65 m², aneurysmal diameter=65 mm

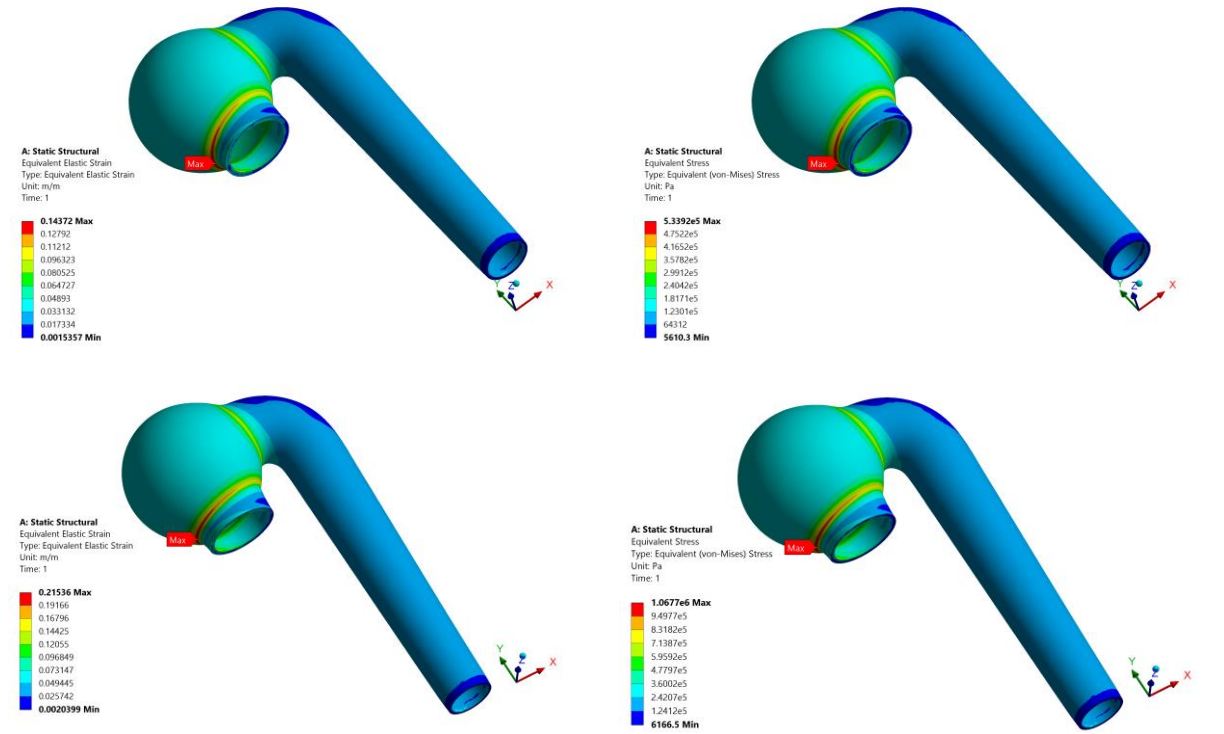

Figure 5.5. BSA=1.65 m², aneurysmal diameter=67.5 mm

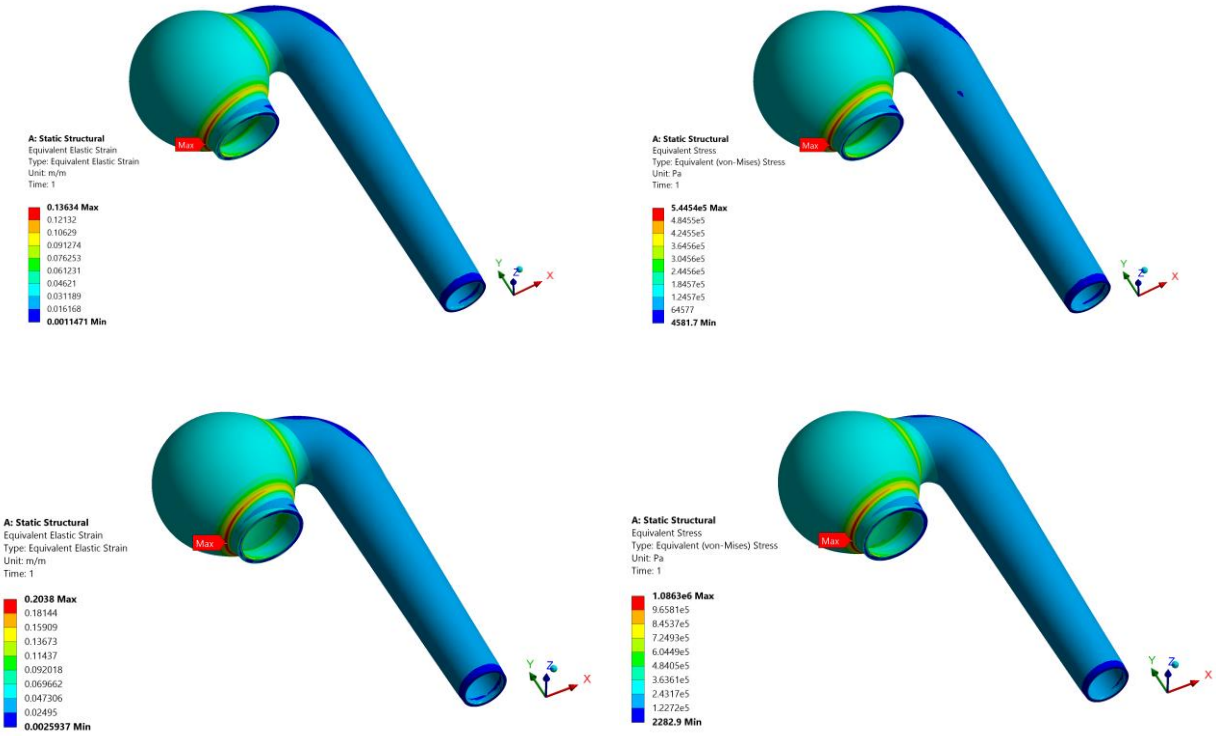

Figure 5.6. BSA=1.65 m², aneurysmal diameter=70 mm

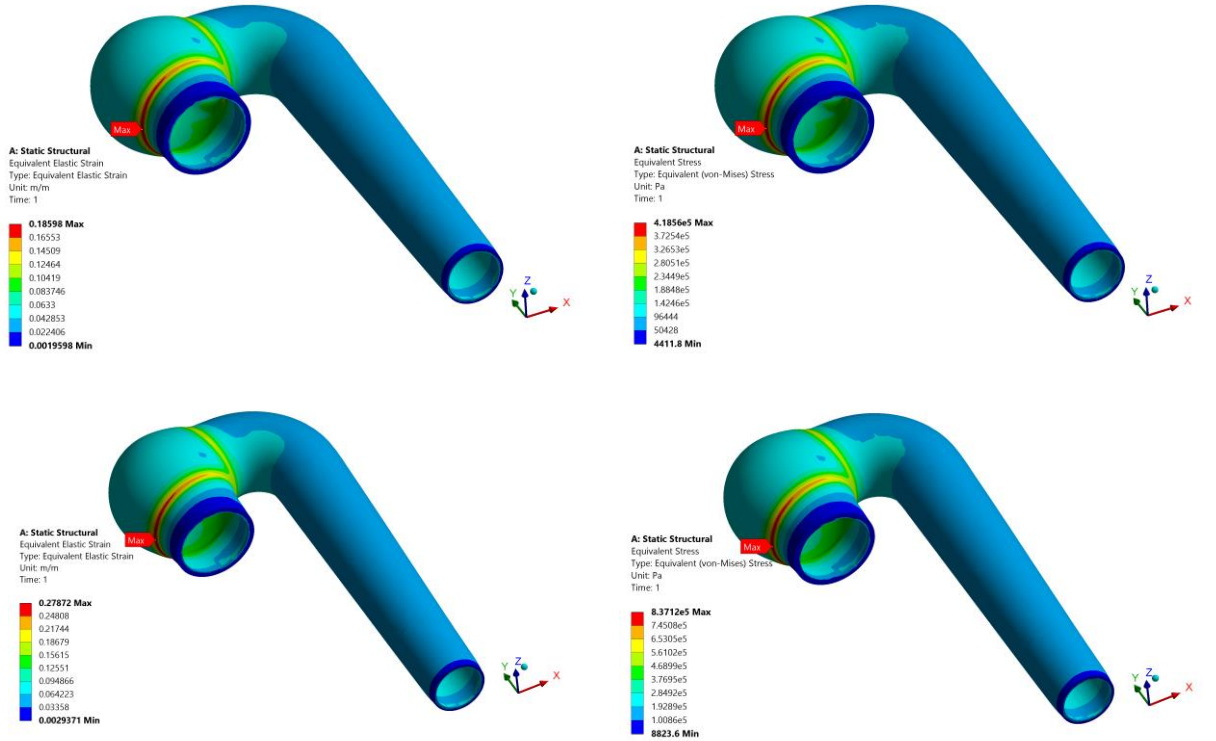

Figure 5.7. BSA=1.85 m², aneurysmal diameter=52.5 mm

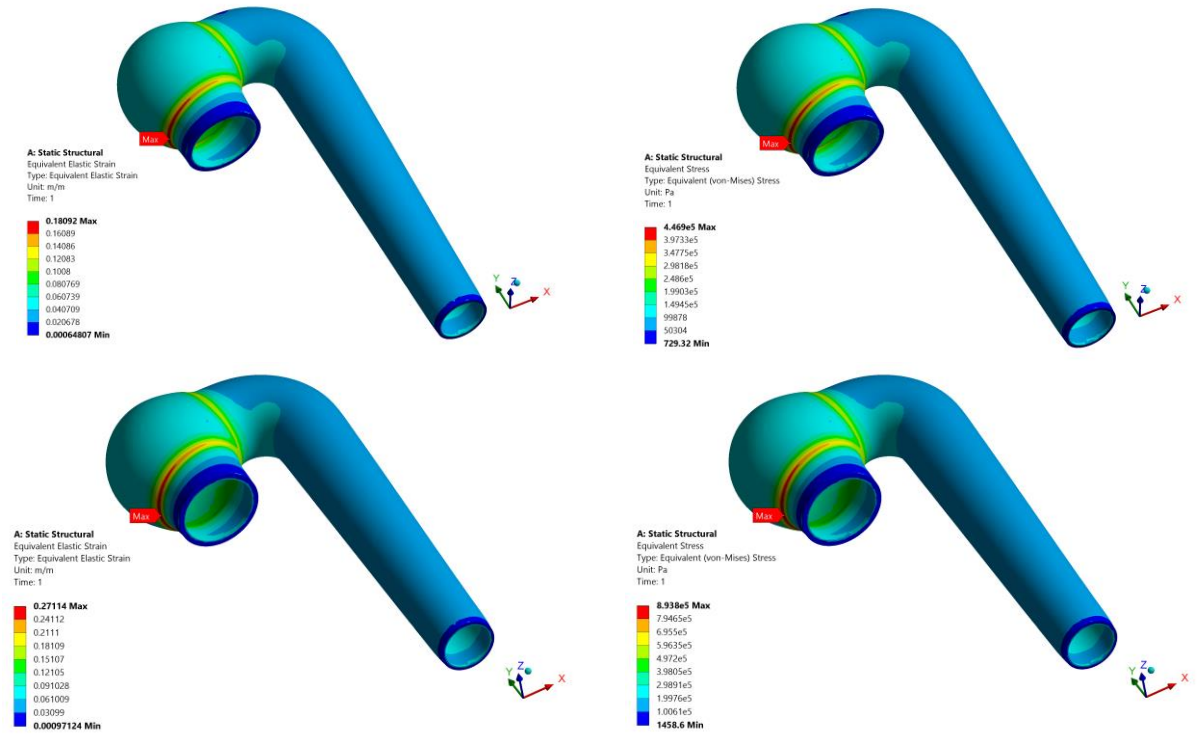

Figure 5.8. BSA=1.85 m^2, aneurysmal diameter=55 mm

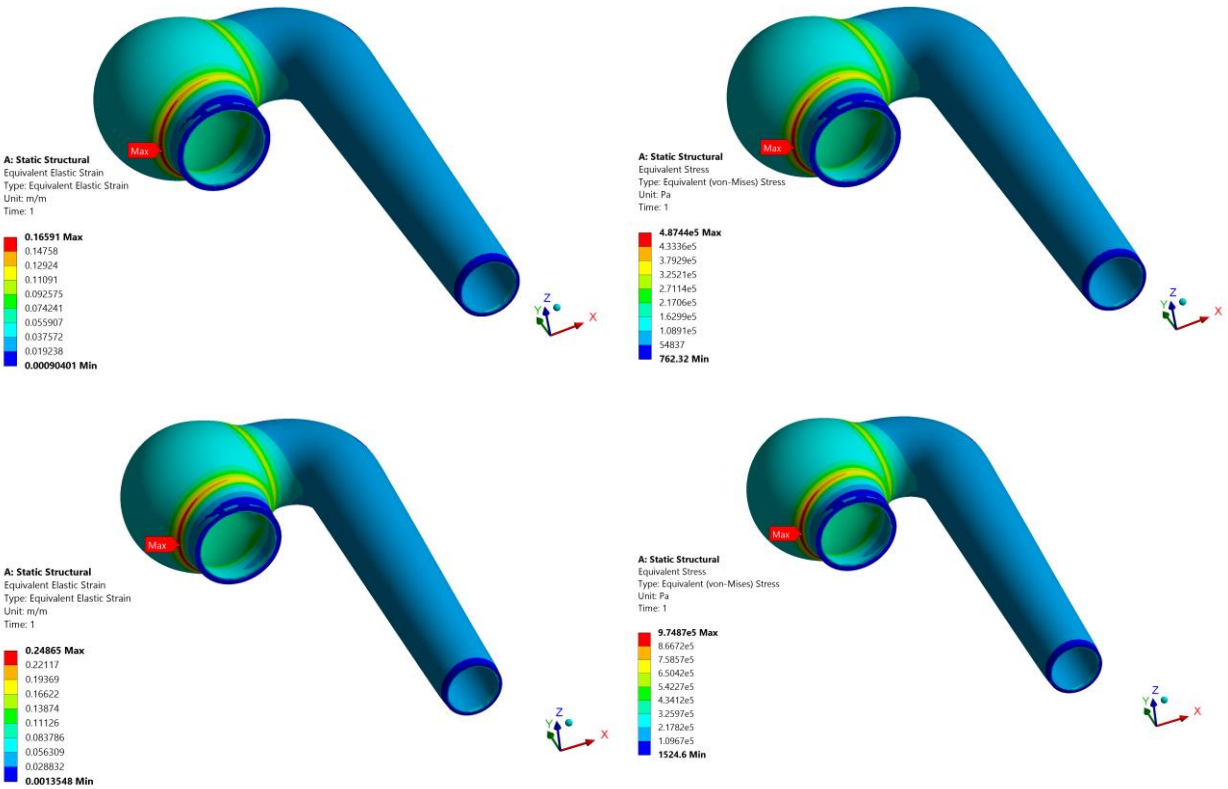

Figure 5.9. BSA=1.85 m^2, aneurysmal diameter=60 mm

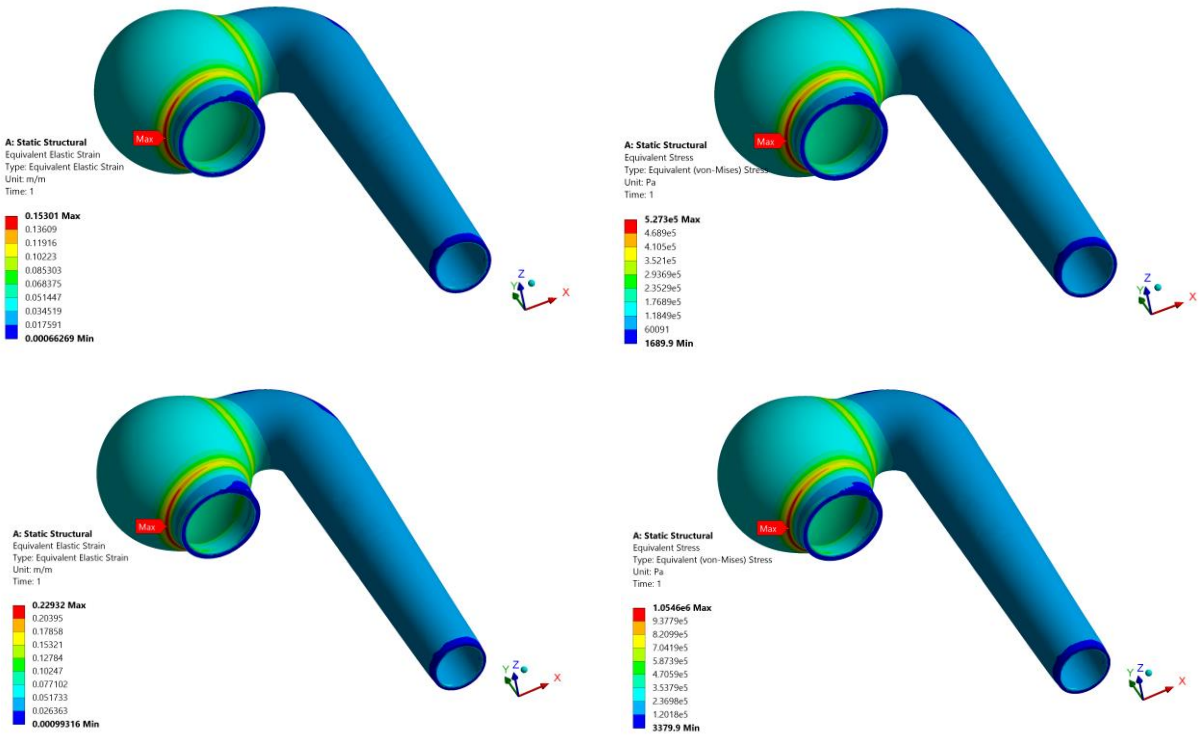

Figure 5.10. BSA=1.85 m^2, aneurysmal diameter=65 mm

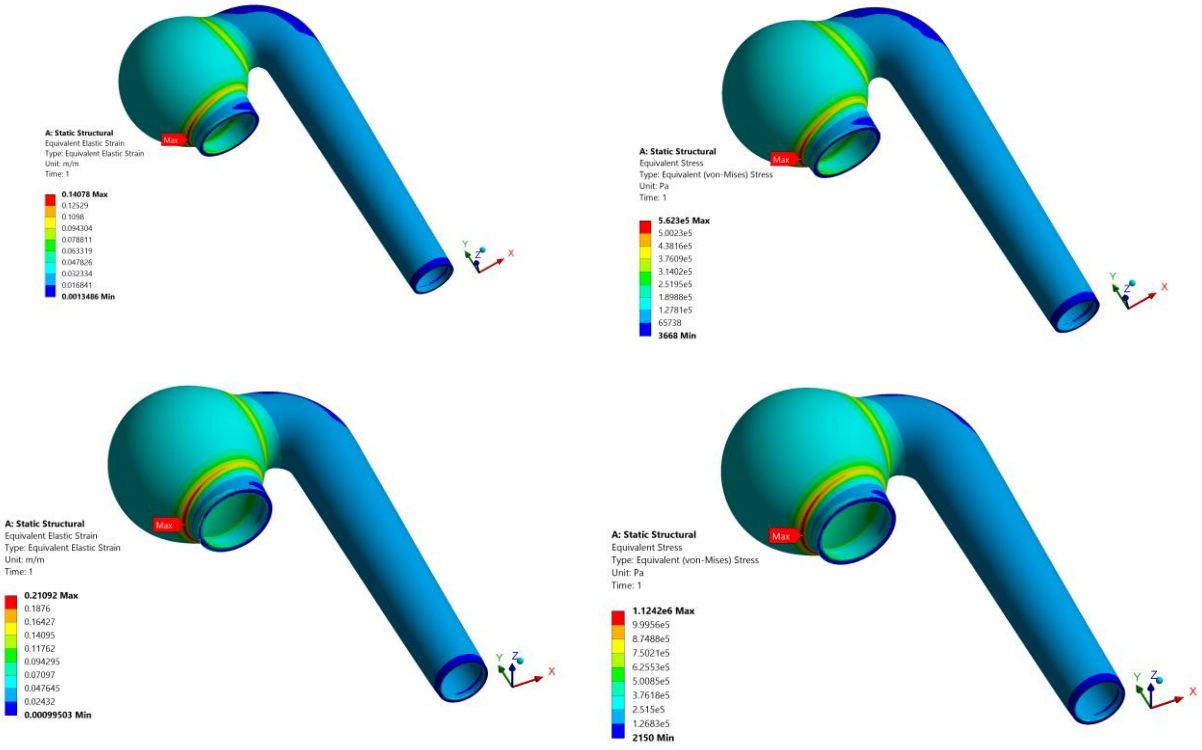

Figure 5.11. BSA=1.85 m^2, aneurysmal diameter=70 mm

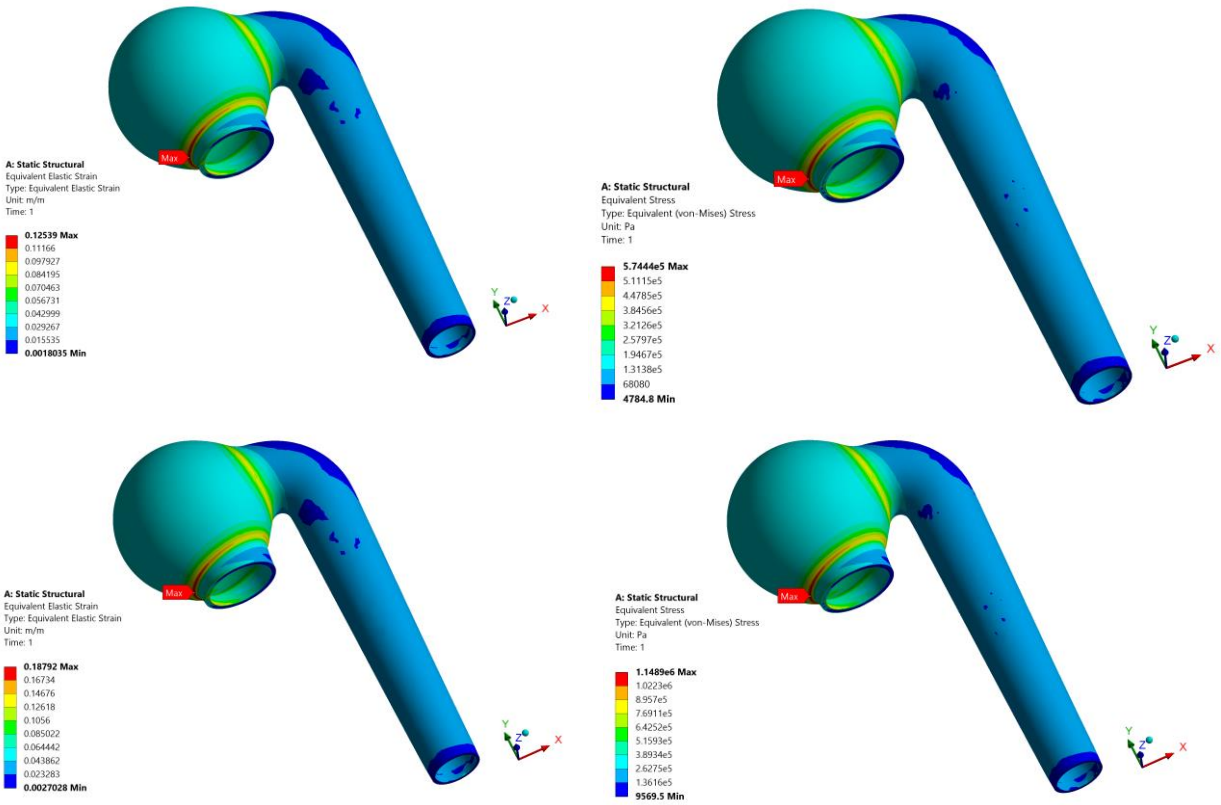

Figure 5.12. BSA=1.85 m², aneurysmal diameter=75 mm

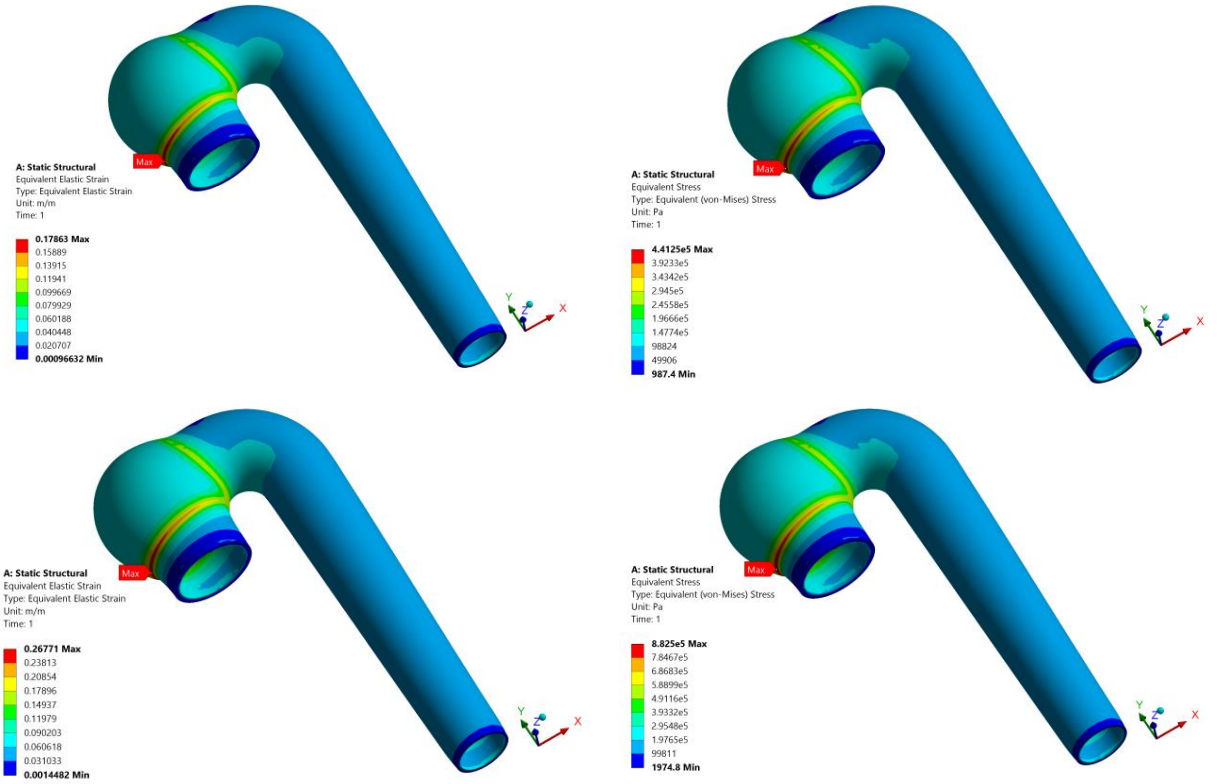

Figure 5.13. BSA=2.0 m², aneurysmal diameter=55 mm

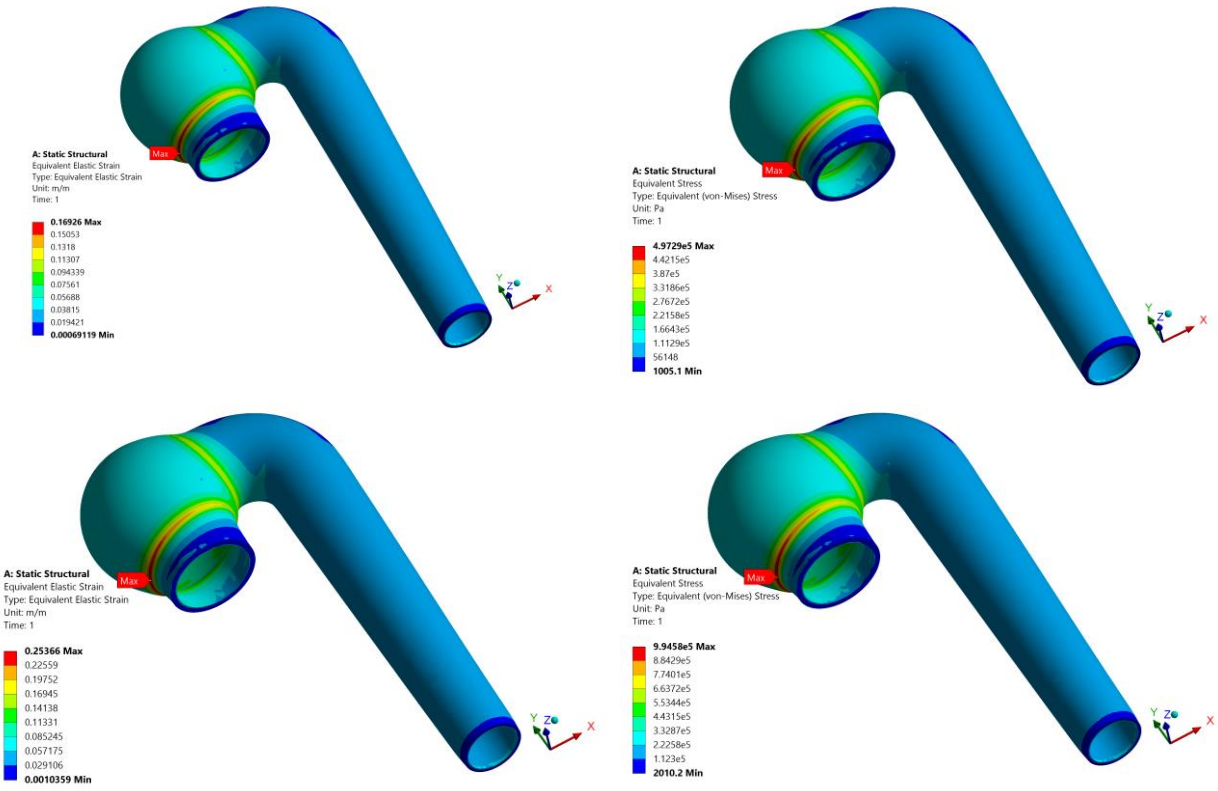

Figure 5.14. BSA=2.0 m², aneurysmal diameter=60 mm

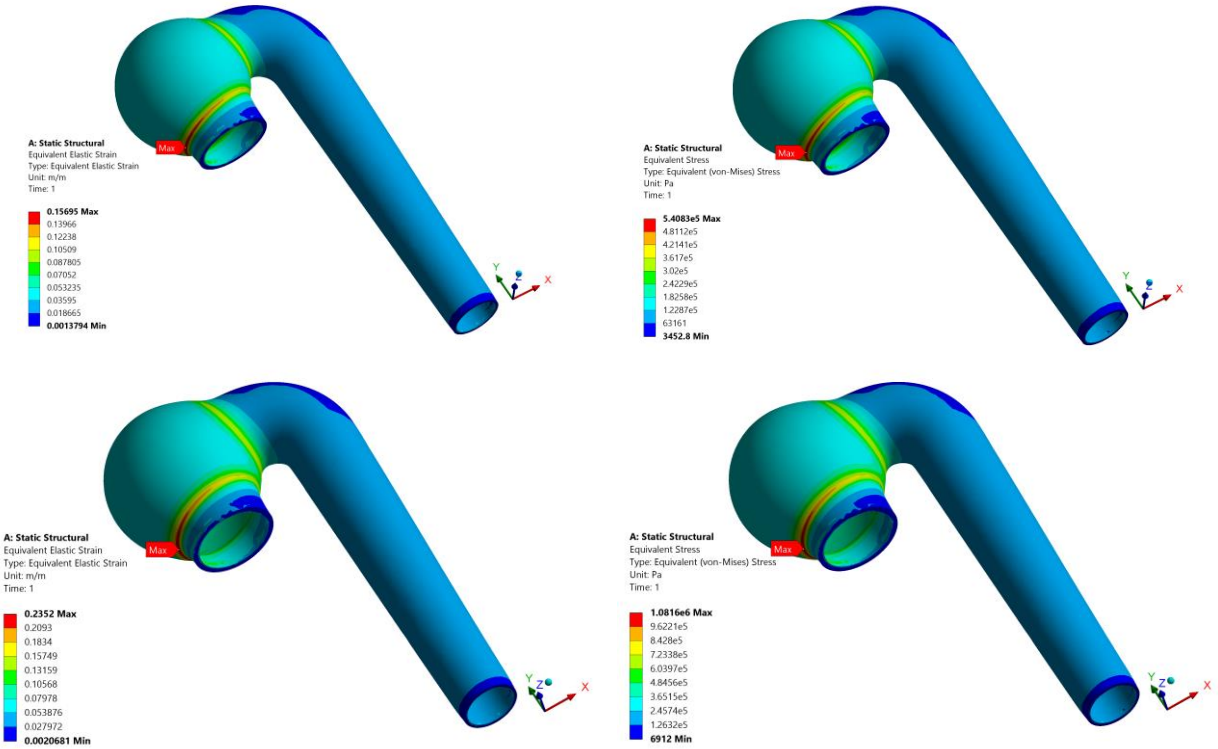

Figure 5.15. BSA=2.0 m², aneurysmal diameter=65 mm

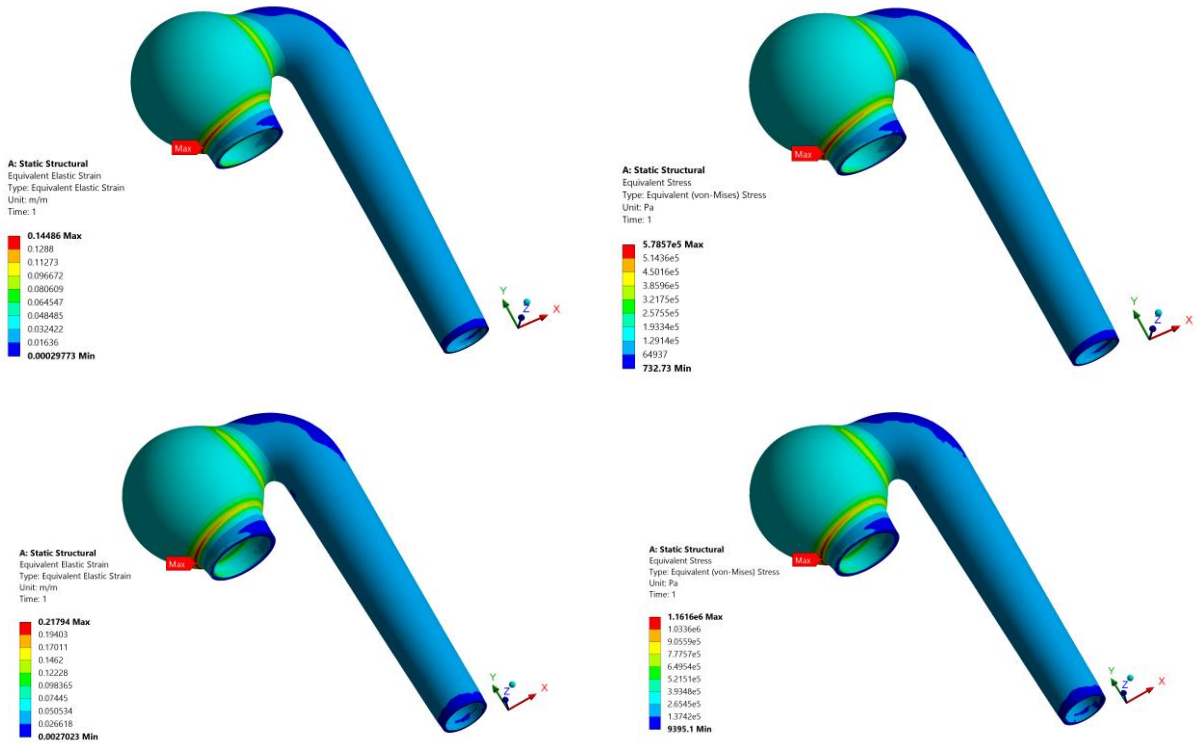

Figure 5.16. BSA=2.0 m², aneurysmal diameter=70 mm

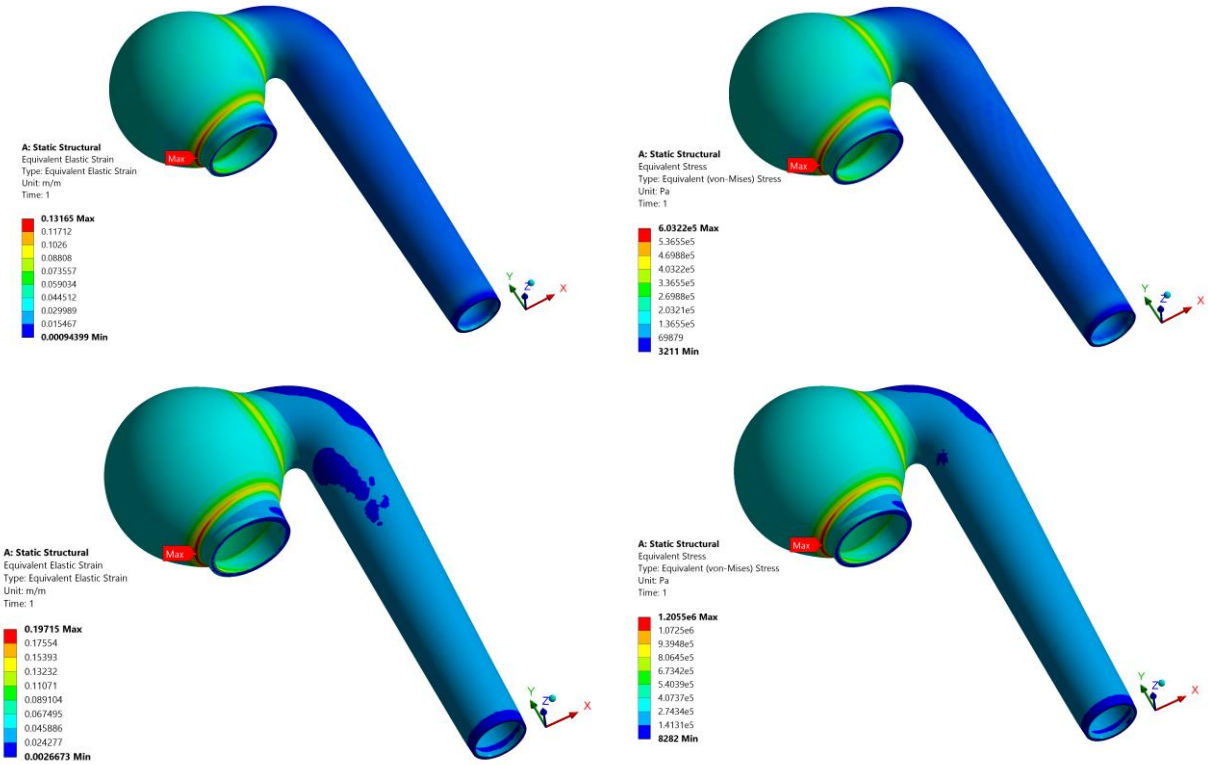

Figure 5.17. BSA=2.0 m², aneurysmal diameter=75 mm

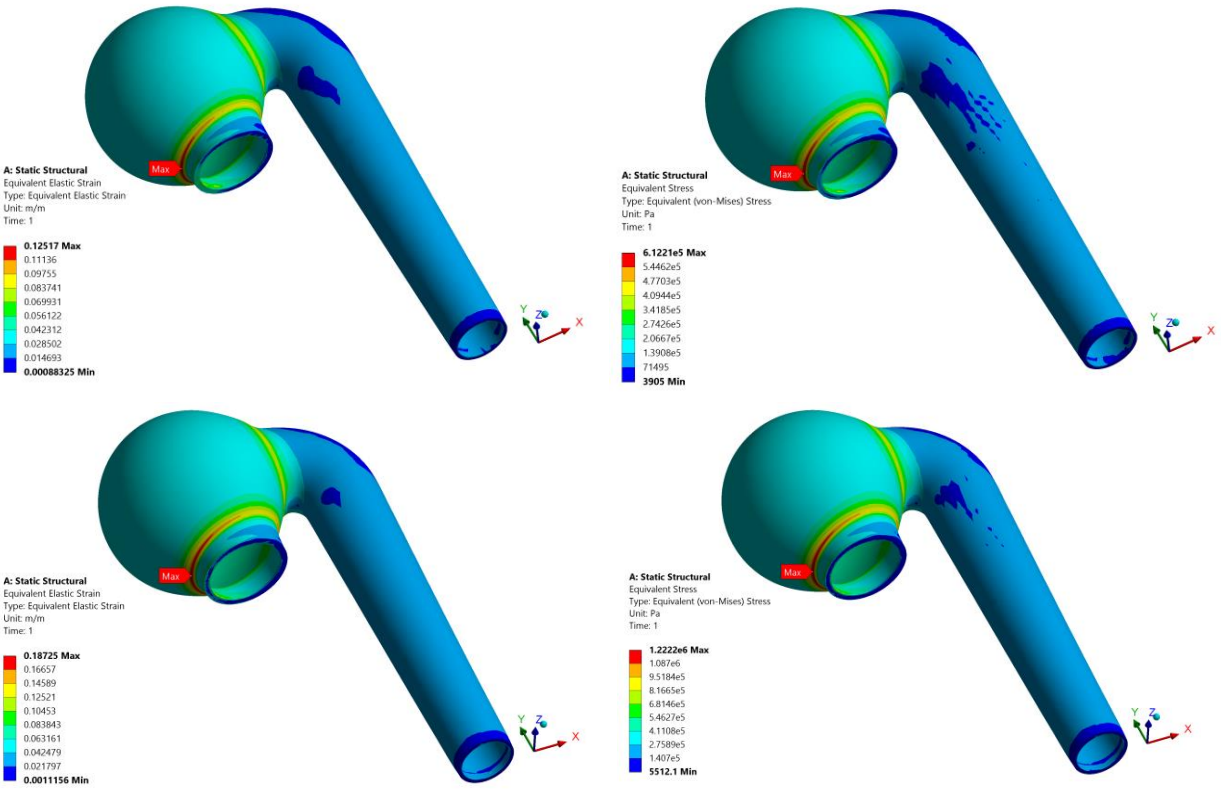

Figure 5.18. BSA=2.0 m^2, aneurysmal diameter=77.5 mm

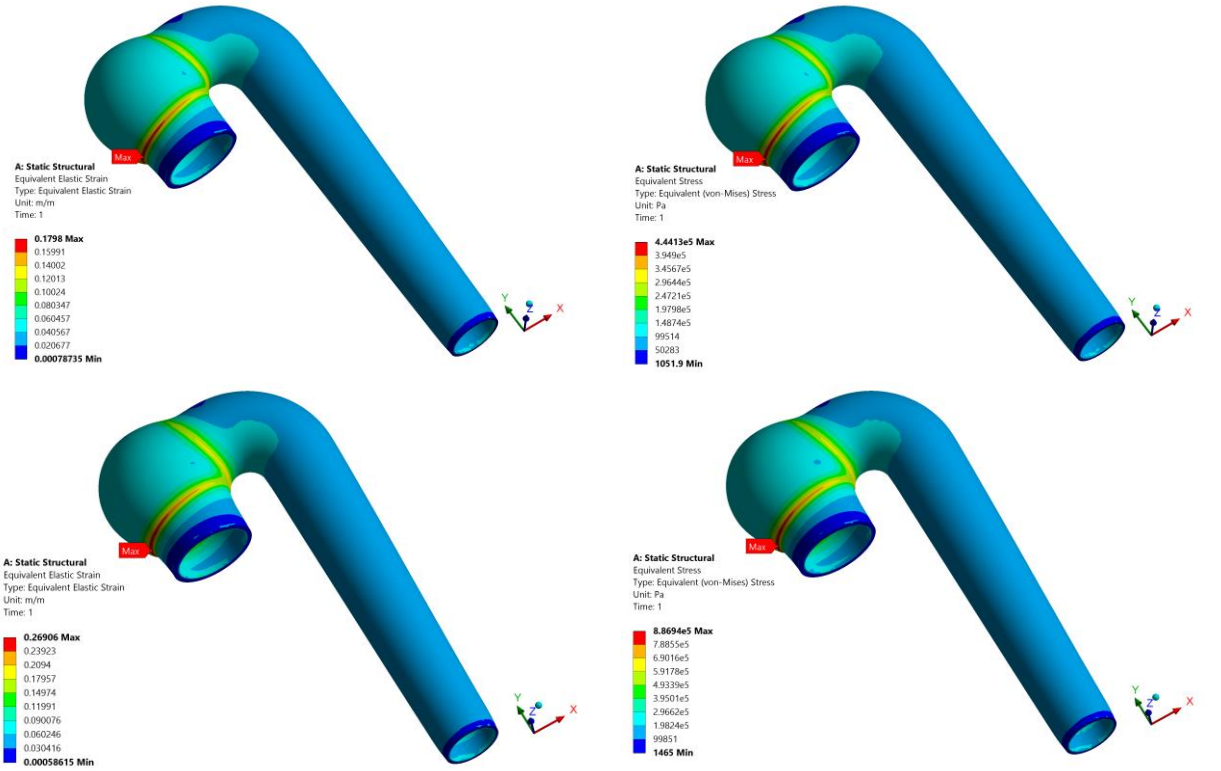

Figure 5.19. BSA=2.2 m^2, aneurysmal diameter=55 mm

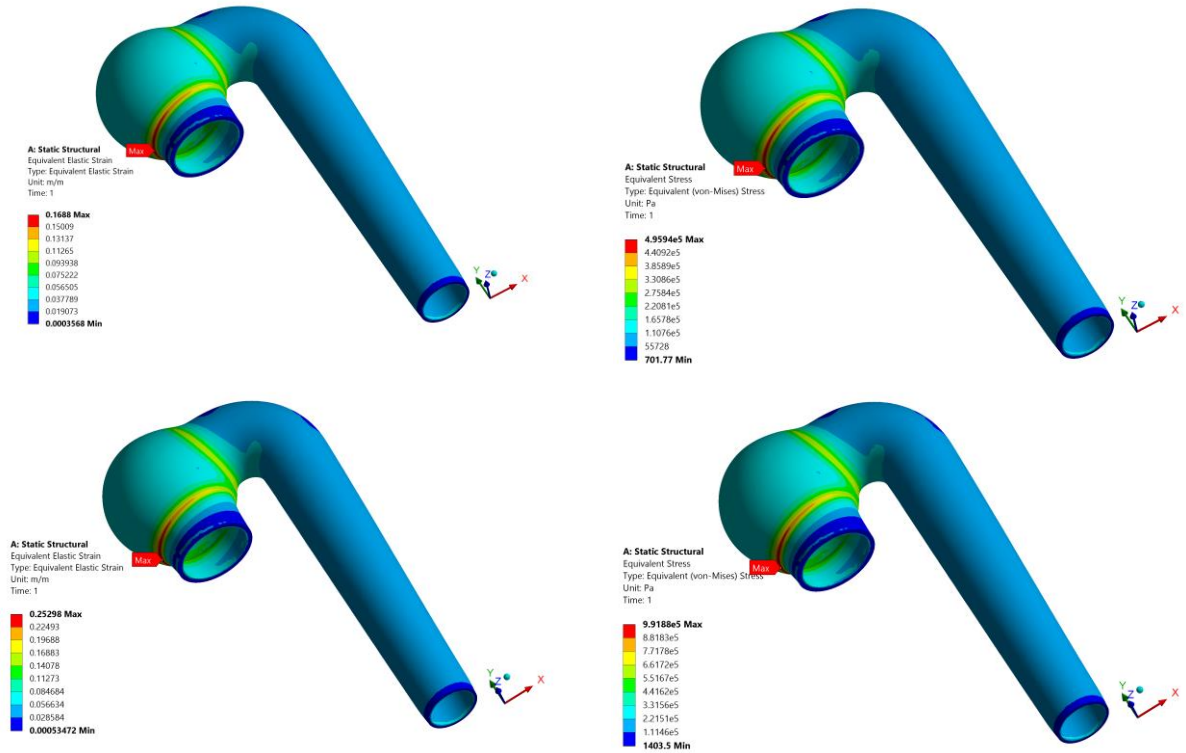

Figure 5.20. BSA=2.2 m², aneurysmal diameter=60 mm

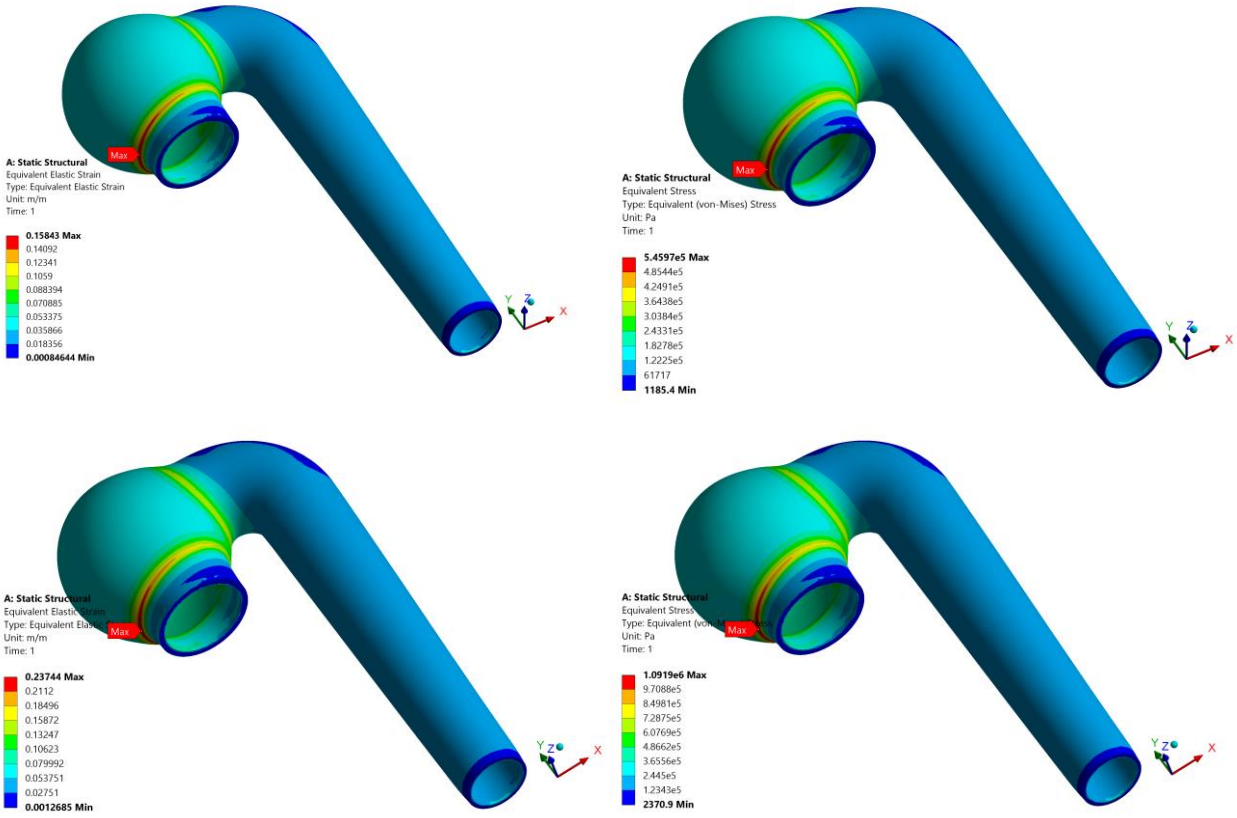

Figure 5.21. BSA=2.2 m², aneurysmal diameter=65 mm

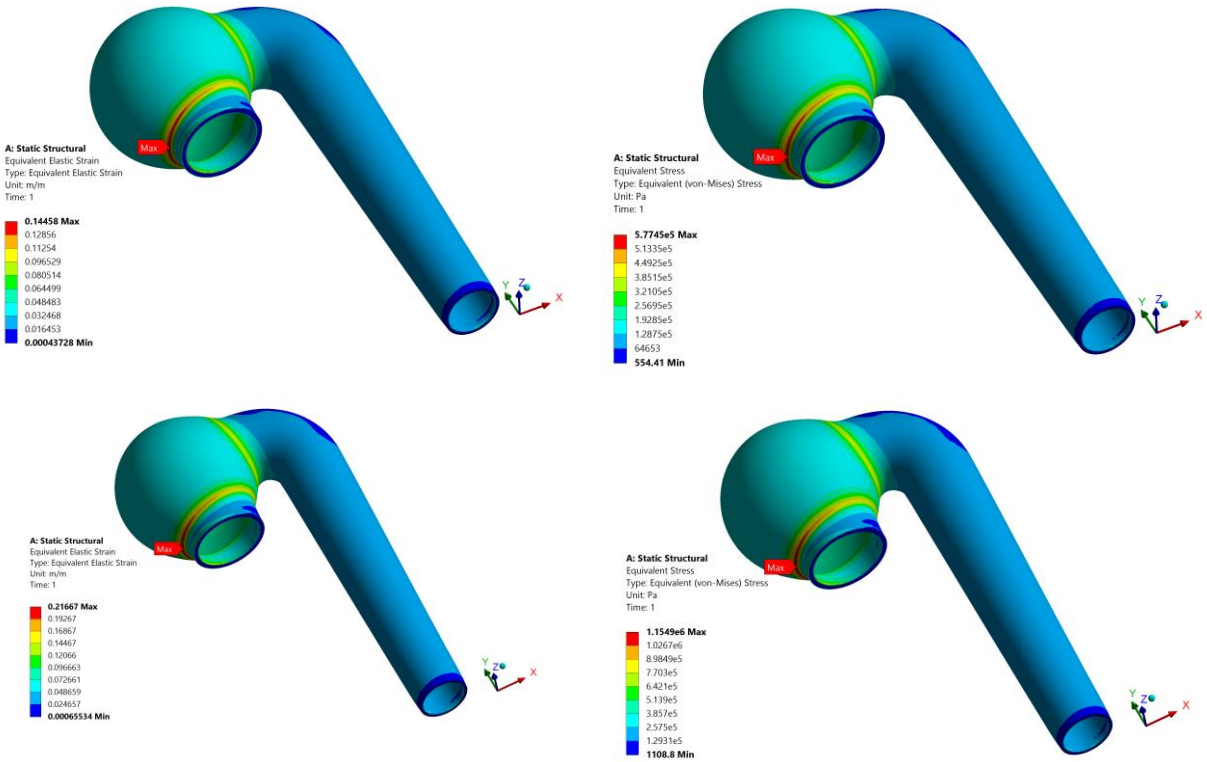

Figure 5.22. BSA=2.2 m², aneurysmal diameter=70 mm

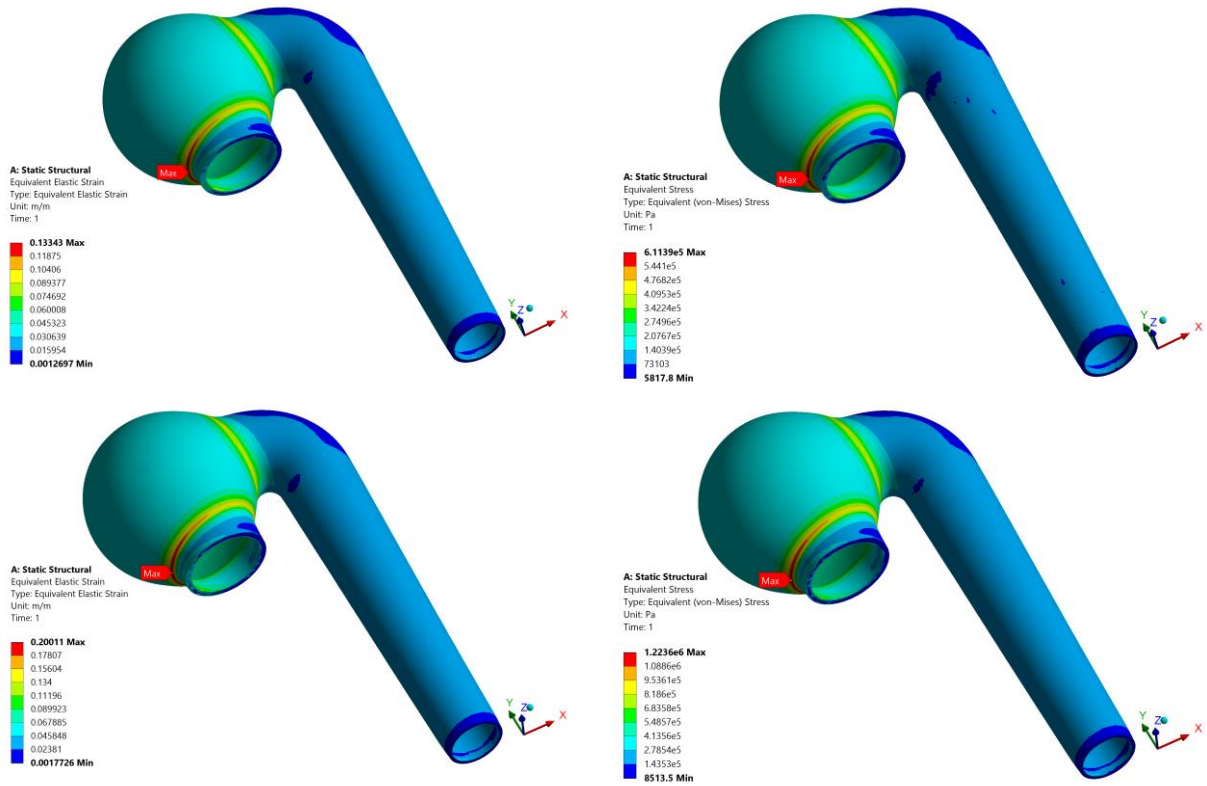

Figure 5.23. BSA=2.2 m², aneurysmal diameter=75 mm

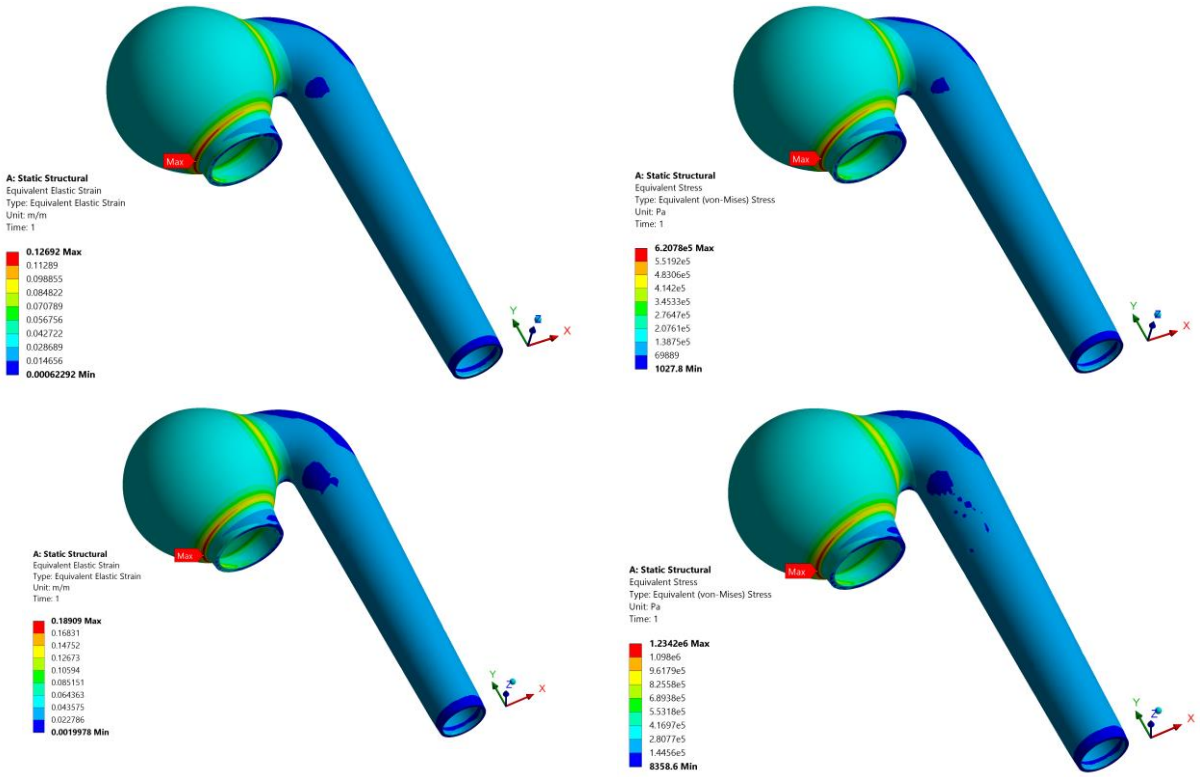

Figure 5.24. BSA=2.2 m², aneurysmal diameter=77.5 mm

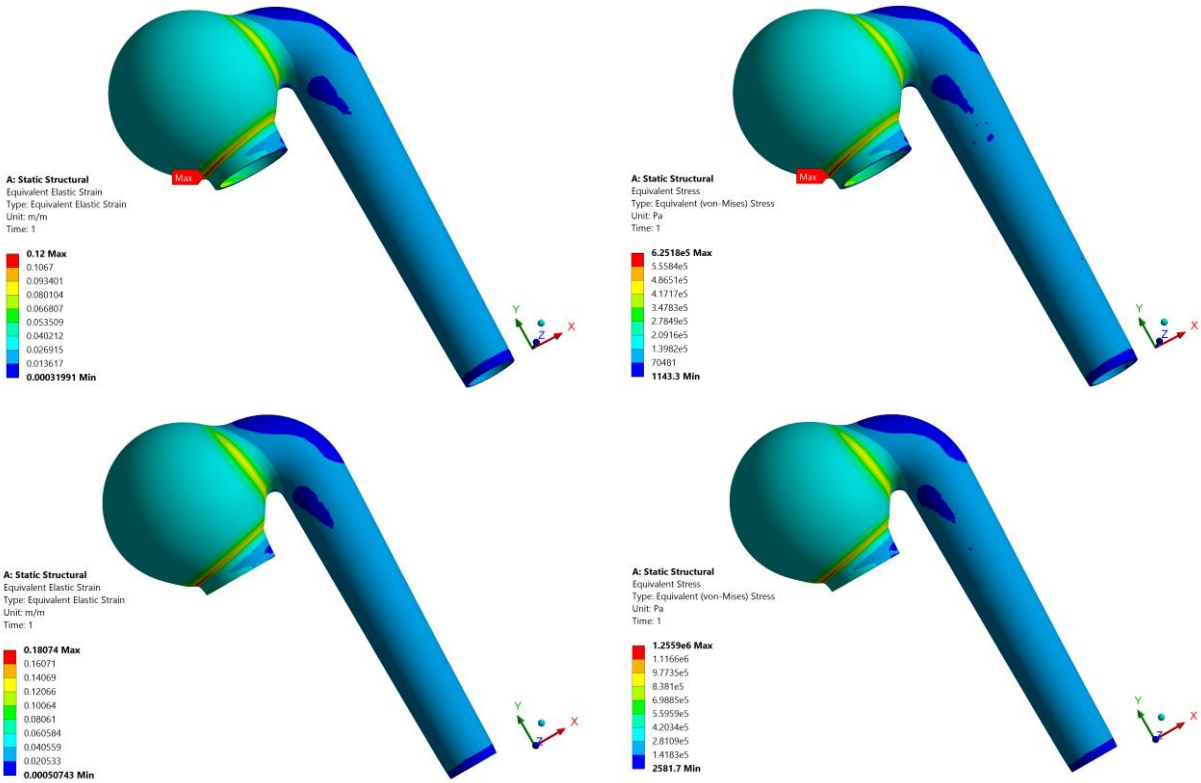

Figure 5.25. BSA=2.2 m², aneurysmal diameter=80 mm

Average Stress and Maximum Total Deformation

Below are shown charts of average stress and maximum total deformation as a function of the aneurysmal diameter, for all of the four BSA values.

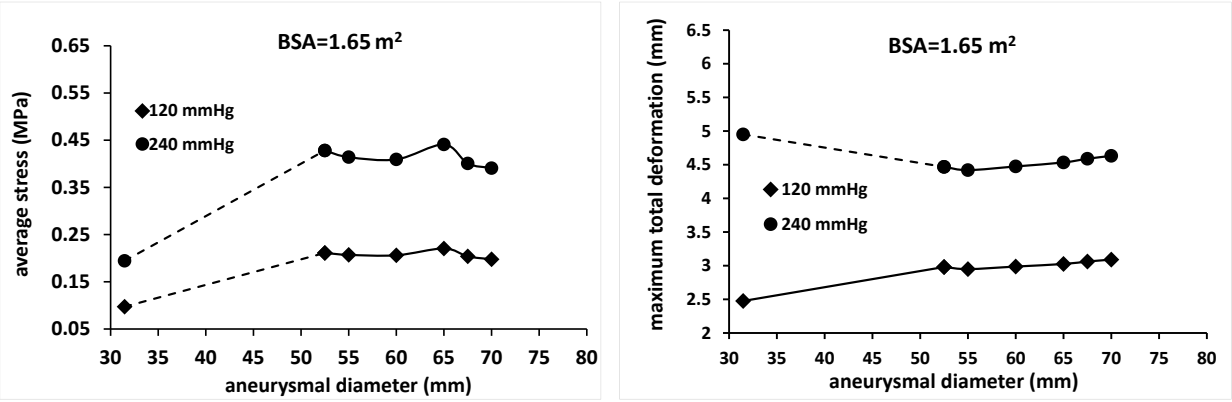

(a) *(b)*

Figure 5.26. BSA = 1.65 m²; (a) Average Stress (MPa) – Aneurysmal diameter (mm). (b) Maximum Total Deformation (mm) – Aneurysmal diameter (mm).

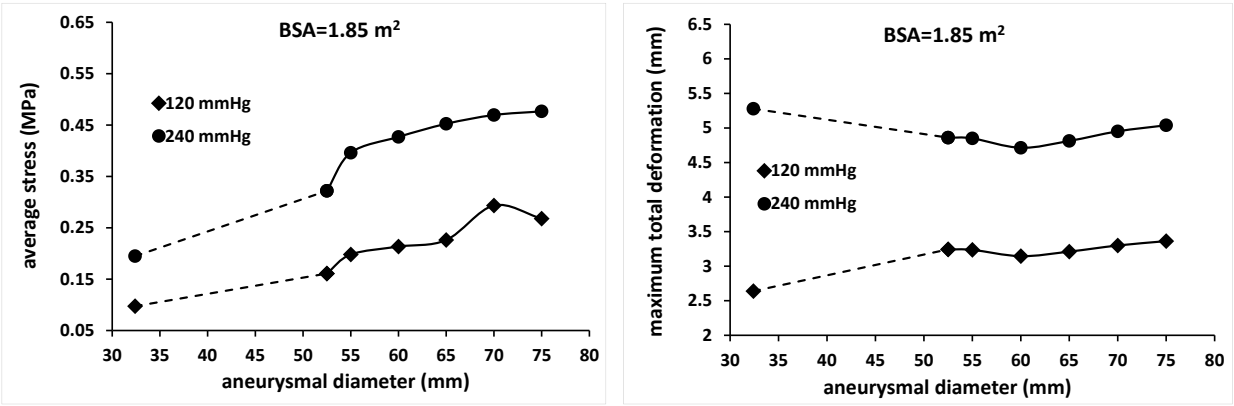

(a) *(b)*

Figure 5.27. BSA = 1.85 m²; (a) Average Stress (MPa) – Aneurysmal diameter (mm). (b) Maximum Total Deformation (mm) – Aneurysmal diameter (mm).

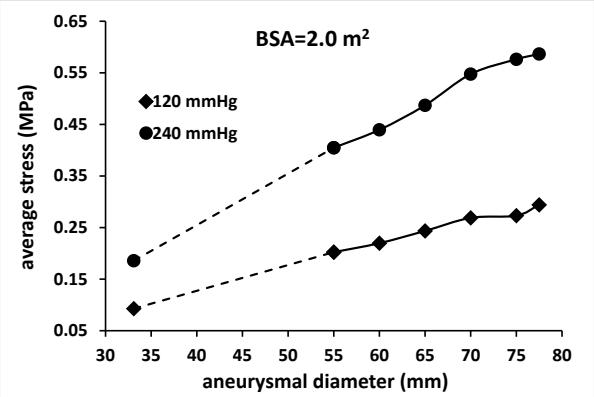

(a)

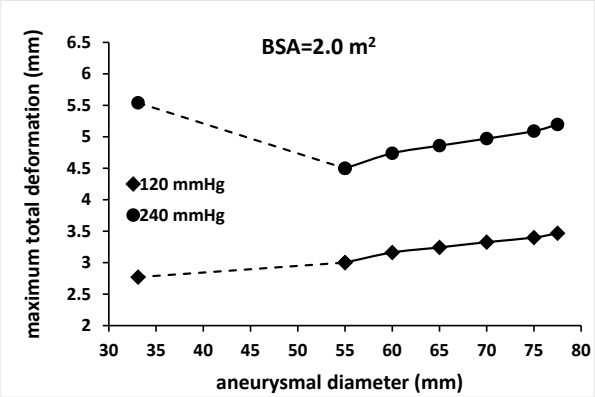

(b)

Figure 5.28. BSA = 2.00 m²; (a) Average Stress (MPa) – Aneurysmal diameter (mm). (b) Maximum Total Deformation (mm) – Aneurysmal diameter (mm).

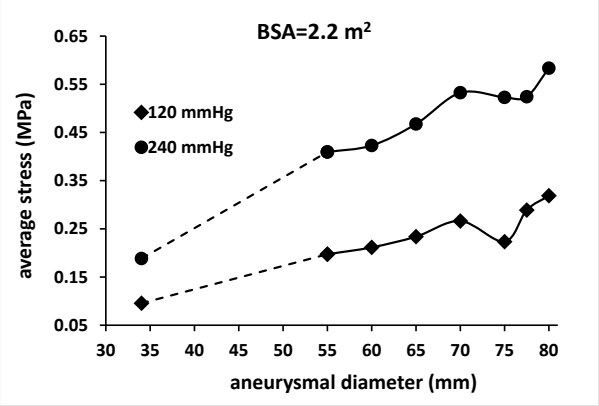

(a)

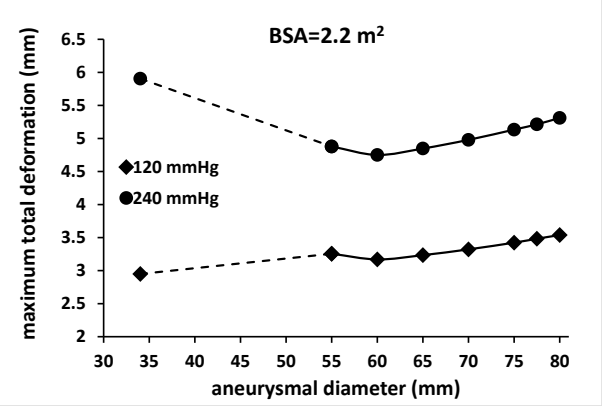

(b)

Figure 5.29. BSA = 2.20 m²; (a) Average Stress (MPa) – Aneurysmal diameter (mm). (b) Maximum Total Deformation (mm) – Aneurysmal diameter (mm).